Spin Polarized Currents in Magnetic and Superconducting Structures

by

Gejian Zhao

A Dissertation Presented in Partial Fulfillment
of the Requirements for the Degree
Doctor of Philosophy

Approved April 2018 by the
Graduate Supervisory Committee:

Tingyong Chen, Chair
Peter Bennett
Robert Nemanich
Quan Qing

ARIZONA STATE UNIVERSITY

May 2018

ABSTRACT

An electrical current with high spin polarization is desirable for the performance of novel spintronics devices, such as magnetic tunnel junction and giant magnetoresistance devices. The generation of spin polarized current can be from ferromagnetic materials or triplet superconductors.

Anomalous Hall effect (AHE) is an effective way to study the properties of magnetic structures. The scattering of electrons by the magnetic moments affects the change of resistance, which can be used to detect the magnetization. In this dissertation, AHE is used to study the perpendicular magnetic anisotropy (PMA) structures, including Co/Pt and Ta/CoFeB/MgO.

Domain walls exist in all ferromagnetic materials. This dissertation studies the domain wall movement in the Ta/CoFeB/MgO structure. A single domain is observed by measuring the anomalous Hall effect. On the other hand, a zero Hall step is successfully observed in a single layer of magnetic material for the first time, which can be used to fabricate advanced domain wall spintronics devices.

Besides the normal ferromagnetic material, the generation of spin polarized current in superconductor is also important for Spintronics. The electrons in superconductors form Cooper pairs. In this dissertation, Andreev Reflection Spectroscopy (ARS) is used to study the spin configuration in Cooper pairs.

Generally, ferromagnetism and superconductivity can not co-exist. In this dissertation, the Bi/Ni bilayer structure has been studied with ARS, and the measurement results show a triplet superconductivity below 4K. The appearance of superconductivity is believed to be attributed to the Bi-Ni interface, and the triplet Cooper pair makes it a promising candidate in superconducting spintronics.

Besides, a Bi_3Ni single crystal is also studied with ARS. The measurements show a singlet superconductivity in this material, which further proves the importance of

the Bi/Ni interface to achieve triplet superconductivity.

Finally, ARS is also used to study $NbSe_2$ monolayer, a 2D superconductor. The monolayer is verified by the measurements of critical temperature and critical field, which are different from the values of multilayer or bulk. Andreev reflection results show that $NbSe_2$ monolayer is a singlet superconductor and there is no node exist in the superconducting gap for a in plane magnetic field up to 58 kOe.

DEDICATION

To my parents.

ACKNOWLEDGMENTS

First, I would like to thank my advisor, Prof. Tingyong Chen for his guidance and help through my graduate career. Prof. Chen has been patiently helping me in learning magnetism, gaining new technical skills, and building the confidence in my research work. He always encouraged me to read more books, papers and websites about various topics related to my research to broaden my view. And he also trained me very patiently in how to do presentation, how to build my network and how to be professional. I have learned so much from him, not only magnetism, superconductivity and experimental techniques, but also the way of being a real researcher.

I also need to thank Prof. Peter Bennett for mentoring me in both course work and research. I would also like to thank Prof. Robert Nemanich on advising me on my research work and dissertation. I am also grateful to have Prof. Quan Qing in my graduate committee and I have learned a lot from his comments and suggestions on my research work. Also, a special thanks to Prof. David Smith for helping me on TEM measurement for my sample, which benefits my research a lot. On the other hand, I would also thank my collaborators, Dr. Jing Shi, Dr. Chia-Ling Chien, Dr. Xiaofeng Jin, Dr. Yulong Jin, Dr. Xinxin Gong and many others for so many interesting projects that make my graduate career fruitful.

I would also like to thank my colleagues in ASU, including Dr. Jessica Gruss, Dr. Dongrin Kim, Dr. Zhicheng Liu, Dr. Fan Fan, Dr. Leijun Yin, Dr. Chufeng Li, Guibin Song, Ji Zhang, Bochao Li, Miguel Bueno, Zhiyu Huang, Nathen Vargas, Salar Samie for their academic supports. Without these help, I could not have achieved what I have now.

I also need thanks to my friends Qi Ren, Yaozhong Song, Runchen Fang, Yongtao Wang, Haotong Wang, Mei Hao and so many other friends for their supports in my life.

A special thanks to all my family members. They went through the most difficult time in the graduate study period with me. Their encouragement and love helped me make the right decisions in the hard time and earn my doctorate. Thank you for your patience, love and endurance.

TABLE OF CONTENTS

CHAPTER Page

CHAPTER Page

LIST OF FIGURES

Figure Page

Figure Page

Chapter 1

INTRODUCTION

The discovery of electricity can be dated back to the ancient time. In about 2750 B.C. [1], the ancient Egyptian found that some kind of fish could make people feel shock. This fish was then known as the 'electric fish', which could generate electricity when it felt dangerous. At that time, the Egyptian named the electrical fish 'Thunder of the Nile'[2]. The description of this electric fish can also be found in the report from other places, such as the ancient Greek, Roman and so on. Later, in about 600 B.C., people found out that if one used cat's fur to rub a rod of amber, the rod could attract light objects, which was due to the generation of the so called 'static electricity'[3].

Magnetism was also discovered quite early. The first literature record about magnetism lies in a 4th-century B.C. book from China. The book described a material called lodestone, which could attract iron when put close to each other. Later, in the 11th century, a Chinese scientist, Shen Kuo, wrote about the first model of compass in his then quite famous book, 'Dream Pool Essays'. In his book, he introduced that when a needle of lodestone was put on a kind of smooth plate, it would point to the south direction. This idea was then used to make compass, which had greatly benefited the exploration of the new continent.

For quite a long time, electricity and magnetism remained two separated topics. Until 19th century, people started to discover the close relation between them.

1.1 Electromagnetism

Electricity remained a little bit like 'magic' until the 17 century, when the first industrial revolution enlarged the usage of electricity in people's daily life. Since then, the exploration of electricity and magnetism became quite rapidly. In 1802, Romangnosi discovered that if a voltaic pile was connected to a electric wire, a compass nearby would be deflected. This was the first observation of the relationship between man-made electricity and magnetism. Later, in 1820, Hans Christian Orsted did a similar experiment and this phenomenon started to become widely known.

Encouraged by Orsted's observation, people started to put a lot of effort on exploring the relationship between electricity and magnetism. Since then, Ampère's Law (1920), Biot-Savart Law (1820), Faraday's Law of Induction (1831) etc. uncovered the different aspects of the electromagnetism. In 1861, James Clerk Maxwell unified all the previous discoveries into a series of equations, which were then the quite famous Maxwell's Equations. The equations enlightened an amazing picture of electromagnetism: electricity and magnetism are so closely connected that they can be induced mutually. Since then, the electromagnetism developed quite fast and scientists can use them to explain and predict quite a bit of phenomena, including the propagation of light, electromagnetic waves, in air and in waveguide and so on. These progresses stimulated the emergent and fast growth of the information technology.

1.2 Electronics

The usage of current charge greatly change people's life. With current, people can have reliable light source, control machines to fabricate staffs, use computers to complete almost all jobs instead of using any paperwork, use internet to stay in touch

with families and friends. Now it is hard for people to live in a quite 'natural' place, without electricity. It is not exaggerate to say that electronics has been integrated into people's life. The normal current makes use of the electron charge. Under the external electrical potential, the electrons in a closed circuit will move continuously, thus the charge current can be generated.

Besides forming current by the electric field, electrons and the associated electrical fields can be affected and controlled by an electronic system in a manner consistent with the intended functions people need. For example, a circuit can be purposely designed to be an amplifier, or radio signal receiver, with some proper components, such as capacitors, inductors, diode, transistors etc. The vacuum tubes were one of the earliest electronic components[4]. The tubes took signals from parlor tricks and give people radio, television, radar signal and so on. On the other hand, the discovery of semiconductor vastly expanded the possibility of electronic components and devices. The behavior of charge carriers, such as electrons and holes, within the semiconductor materials and related structures, is the fundamental of diodes, transistors and many other modern electronics devices. In April, 1955, IBM introduced the first calculator which contained only transistor circuits without any vacuum tubes[5]. From then on, the transistors started to dominate the electronics devices. With the rapid development of nanotechnology, transistors have been fabricated to be smaller and smaller. In 2017, the number of transistors in one chip can be as high as 18 billions from Qualcomm, which greatly enhance the performance of computers.

1.3 Spintronics

Electronics makes use of the charge of electrons. However, in modern physics, an electron has not only charge, but also an intrinsic property: spin. Instead of a real rotational motion, spin is an intrinsic form of angular momentum carried by

all kinds of elementary particles, such as proton, electron, neutron etc[6]. The first experimental observation of spin came from two German physicists: Otto Stern and Walther Gerlach in the year 1922[6]. During the original experimental, a beam of silver atoms were sent through a non-uniform magnetic field. Showing no magnetic property in nature, Ag was regarded as a non-magnetic material. Therefore, nothing should happen when the silver atoms went through the magnetic field. However, the experimental results surprised everyone: the sliver beam was split into two separated beams. Therefore, they attributed this phenomenon to an intrinsic property of the atom - Spin angular momentum. Later theoretical and experimental study showed that different elemental particles, include electron, had different spin angular momentum. And different from the orbital angular momentum, this spin angular momentum can be integer or half integer. Particles with integer spin are called Bosons, while the ones with half integer spin are called Fermions. Statistically, they will follow Boson distribution and Fermi distribution, respectively. For electrons, the spin will be $\frac{\hbar}{2}$, making it the most commonly seen fermion.

Since the discovery of spin angular momentum, people have been exploring the possibilities to make use of it. In electronics, charge of electrons plays a key role. If spin signal is also considered and made into use, there comes another topic, Spintronics. The spintronics emerged from the discovery of the spin-dependent electron transport phenomena in magnetic structures, in 1980s. One of the most famous structures is the thin film giant magnetoresistance (GMR) structure, discovered by Albert Fert and Peter Grünberg et al in 1988[7, 8]. The huge change of resistance of the GMR structure under the external magnetic field makes it of great importance in the data recording industry. For example, the read head of the magnetic hard drives are now based on the GMR structure. Figure(1.1)[9] illustrate the Co/Cu bilayer based GMR structure. The structure is deposited on a Si substrate, with a Fe buffer layer

of about 135 $\mathring{A}$. The buffer layer enables a better crystal quality of the above Co/Cu layers. The bilayer is repeated 40 times for better GMR ratio. The neighboring two Co layers are separated by a very thin Cu spacer (about 1 $\mathring{A}$) so that the exchange coupling between the two Co layers align the magnetization antiparallel when there is no external field applied. If a current is sent into the structure, the electrons with up-spin and down-spin will be scattered in different layers so that the total resistance is larger. When there is a magnetic field applied to the structure, the magnetization in all the Co layers will be aligned to the field direction. Thus when the electrons pass through the structure, only electrons with up-spin or down-spin will be scattered, resulting in a much smaller resistance.

Besides GMR, another similar structure, magnetic tunnel junction (MTJ), has been discovered by M. Julliere in 1975[10] and has been extensively studied since 1990s[11–18]. New memory technique, such as magnetoresistive random access memory (MRAM) is based on this MTJ structures. Compared with the typical memory (SRAM, DRAM etc.), MRAM is a non-volatile devices that can keep information even after power is off, because the information is stored by magnetic moment in each bits, instead of the electrical voltage in the transistors. On the other hand, since MRAM stores information with magnetic states, instead of using multiple transistors and capacitors, therefore it possible to greatly shrink the size of each memory bits and reduce the power consumption. Motivated by these advantages, many companies started to put investment into this area and have been making progress through all these years. In 1995, Motorola initiated the development on MRAM and produced the first-generation 256 kb MRAM in 1998[19]. Two years later, IBM and Infineon established a joint research program on MRAM development. Through 2003, several new concepts have been proposed and patented, such as the toggle MRAM[20], spin torque transfer (STT) etc. And after 2004, more real structures and products be-

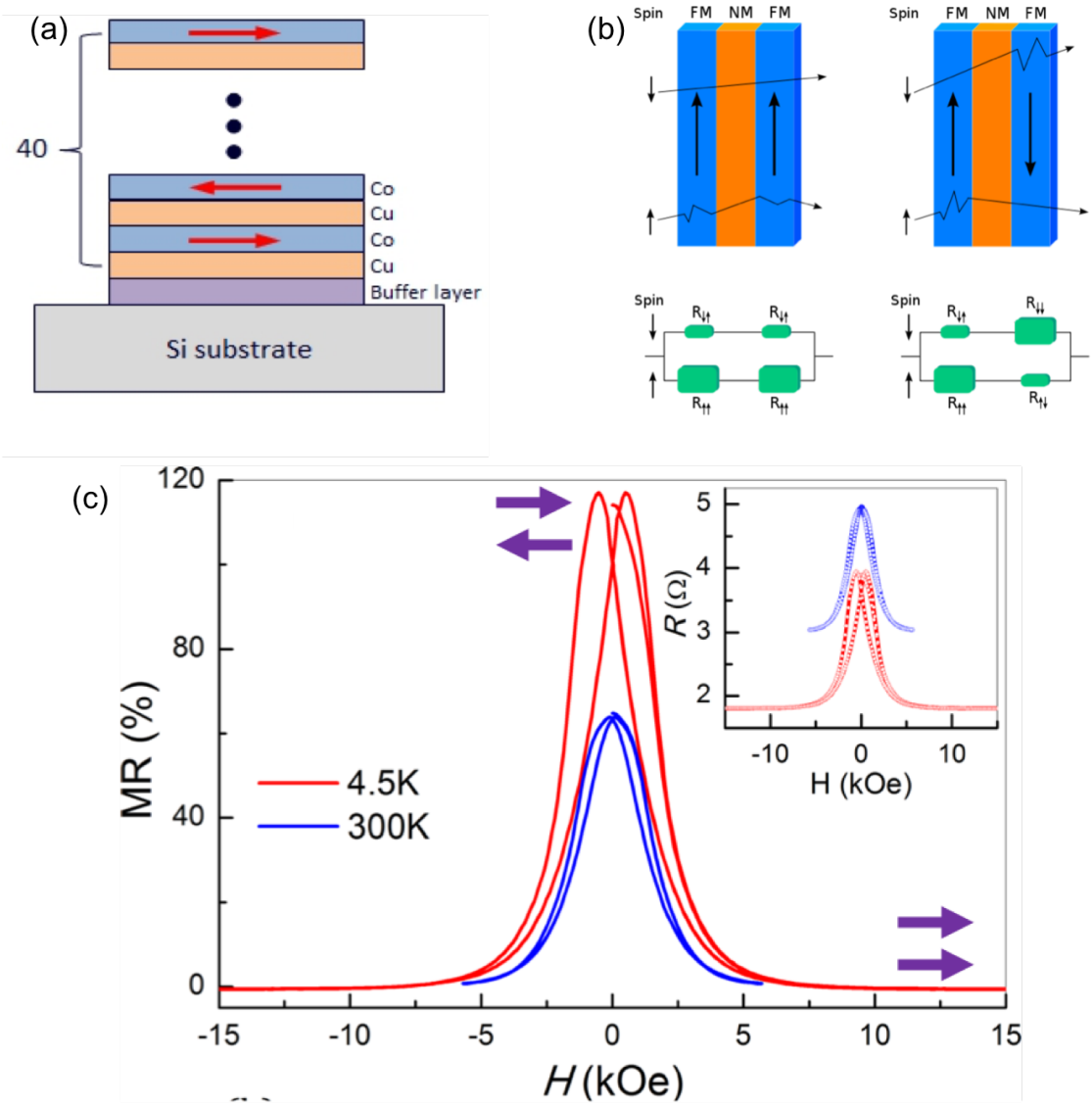

Figure 1.1: (a).Co/Cu GMR structure. (b). Two-current mode of electron scatterings in GMR structure. (c).GMR ratio under room temperature and 4.5K.[9]

came available. In June 2004, Infineon unveiled a 16-Mbit prototype MRAM, with 180 nm lithographic process. One year later, in June 2005, Honeywell published a data sheet for a 1-Mbit MRAM with 150 nm lithographic process. in November 2005, Sony announced the first lab produced STT MRAM, which utilized the spin polarized current going through a MTJ structure to realize data writing. In December 2005, Freescale Semiconductor Inc. demonstrated that MRAM that used magnesium oxide could out perform the traditional aluminum oxide based MRAM structure, by reducing the current required to write information. On July 10th, 2006, Freescale started to sell 4-Mbit MRAM chip[21]. In 2007, MRAM research started to force on STT MRAM. In November, Toshiba proved the first spin transfer torque in the perpendicular magnetic anisotropy MTJ devices, which was quite important to fabricate smaller size memory cell. In June 2009, Hitachi and Tohoku University proved a 32-Mbit STT RAM, making this technique more attractive. And In November, Everspin shipped its first embedded MRAM samples. In the end of 2012, Everspin debuted the 64-Mbit spin torque MRAM with a 90 nm process. In April 2016, IBM and Samsung announced that they could fabricate MRAM device with size of about 11 nm. In August, Everspin began to sell the industry's first 256Mb STT MRAM to customers. Recently, several companies start to announce real MRAM product in 2018, including Samsung, Everspin, GlobalFoundries and TSMC.

Motivated by these fantastic progress, I have done several projects related to spintronics. And in this dissertation, I will discuss those projects and some breakthroughs. This dissertation is organized as follows: In chapter 2, I will introduce different magnetism, which is the fundamental of spintronics, as well as domain wall structure, which plays an important role in the magnetization process. In Chapter 3, I will introduce the basic knowledge of superconductivity, which is quite important and related to a very fast growing researching area, Superconductivity Spintronics. In

Chapter 4, I will talk about spin polarization and Andreev reflection, which is the key concept to study spin configuration in different structures. In the next chapter, I will focus the experimental equipment I use, including magnetron sputtering, Rutherford Backscattering (RBS), Andreev Reflection Spectroscopy, Vibrating Sample Magnetometer (VSM), and the home-made magnetic transport system. Start from Chapter 5, I will talk about the projects I have done. In Chapter 5, two perpendicular magnetic anisotropy (PMA) structures will be discussed. Chapter 7 and 8 will focus two projects related to superconductivity, including the possible triplet superconductivity, Bi/Ni bilayer structure, the Bi_3Ni alloy and 2 dimensional superconductivity.

Chapter 2

MAGNETIC STRUCTURES

Magnetism is one of the oldest natural phenomena in human being's history. In the old days, people made use of the magnet to make compass, which benefited the development of the seafaring. New continents were discovered, international trade began to bloom. Even in nowadays compasses still play an important role in navigation, especially when one comes into a 'wild' place with quite weak satellite signal. Different materials have different magnetism. Some of them, such as Ni, Fe, and Co, will be attracted by magnet, so that they are called Ferromagnet. Some of them, such as Cu, Al, however, will not react to magnet. All the materials are made of atoms, so it is important to find out the source of magnetism.

2.1 Sources of Magnetism

In classical theory, magnetism comes from the orbital motion of electrons around the nucleus. For one electron, assume the radius of the orbit is r, the angular frequency of the circular motion is ω, then the current due to the circular movement of the electron will be:

$$I = -\frac{e\omega}{2\pi r} \tag{2.1}$$

Since this current forms a closed loop, therefore, it can generate a magnetic moment, which can be calculated by:

$$\mathbf{M} = -\mu_0 I\mathbf{S} = -\mu_0 \frac{e\omega r}{2} \tag{2.2}$$

where $\mathbf{M}$ is the magnetic moment, $\mathbf{S}$ is the area of the closed current, μ_0 is the vacuum permeability, and e is the electron charge.

Consider the angular momentum of the movement, $\mathbf{P} = mr\omega$, we have

$$\mathbf{M} = -\mu_0 \frac{e}{2m} \mathbf{P} \tag{2.3}$$

In quantum theory, the orbits of different electrons are not continuous. The orbit angular momentum is $\mathbf{P} = l\hbar$, where l is the orbital angular momentum quantum number. Therefore, the magnetic moment in equation (2.3) can be written as:

$$\mathbf{M} = -\mu_0 \frac{e\hbar}{2m} l = \mu_B l \tag{2.4}$$

where μ_B is called Bohr magneton. From the above equations, one can see that one source of magnetism in a single atom is from the circular movement of electrons.

Besides the orbital angular momentum, electrons have another intrinsic angular momentum, called spin angular momentum. This is another source of magnetic moment. Compared with orbital angular momentum, the magnetic moment due to spin can be written as:

$$\mathbf{M}_s = -\mu_0 \frac{e\hbar}{2m} s = \mu_B s \tag{2.5}$$

where s is the spin momentum quantum number.

Consider both orbital and spin angular momentum, one can write the magnetic moment as:

$$\mathbf{M} = -g\mu_0 \frac{e}{2m} \mathbf{P} \tag{2.6}$$

where g is the Lande's g factor.

Experimental data shows that for most transition metals, g is close to 2. This means that in those materials, the magnetic properties are mainly due to spin angular momentum. For simplification, one can just refer to the spin angular momentum as spin. The discrepancy is due to the effect of the orbital angular momentum[22].

Besides electrons, nucleus also have spin. Therefore, they can also generate spin magnetic moment. However, from equation 2.5 one can see that the spin magnetic moment is inversely proportional to the mass of the particle. Thus, the spin magnetic momentum from the nucleus is almost negligible since the mass of the nucleus is usually three orders of magnitude larger than that of an electron. In other words, the magnetic moment from one single atom mainly comes from the spin magnetic moment of the electrons. For simplification, one can use spin direction to represent that of magnetic moment.

2.2 Classification of Magnetism

Single atom can have magnetic moment, due to the arrange of electrons outside the nucleus. If many atoms gather together and form a bulk material, such as crystal, the magnetic moment from each atom may be affected by each other. The summation of all the magnetic moments in a unit volume is called Magnetization. In different material, the magnetization will behave differently under the external magnetic field, which can be typically put into five categories: Diamagnetism, Paramagnetism, Ferromagnetism, Antiferromagnetism, and Ferrimagnetism.

2.2.1 Diamagnetism and Paramagnetism

Langevin Diamagnetism

In classical theory, diamagnetism comes from the orbital movement of electrons outside the nucleus. This orbital movement forms a circular current, which follows the

classical electromagnetism rules. If an external magnetic field is applied to this current, a magnetic moment that is opposite to the original moment, which is generated by the current, will be induced, as is indicated by the Lenz's law. Through a simple mathematic calculation, the susceptibility of the diamagnetism is[23]:

$$\chi = \frac{\mu_0 N \mu}{B} = -\frac{\mu_0 N Z e^2}{6m} \left\langle r^2 \right\rangle \tag{2.7}$$

where N is the number of atoms per unit volume, B is the applied external field, Z is the number of electrons in one atom, e is the electron charge, m is the mass of an electron, and r is the radius of the electron, μ_0 is the permeability in free space. From equation (2.7), one can see that the external field will induce a negative effect on the magnetization, or susceptibility. Thus, this behavior is called diamagnetism.

However, from the view of quantum physics, the orbital motion of electron does not exist. When a magnetic field is applied to one atom, the effect of it should be added to the Hamiltonian as[23]:

$$\mathcal{H} = \frac{ie\hbar}{2mc}(\bigtriangledown \cdot \mathbf{A} + \mathbf{A} \cdot \bigtriangledown) + \frac{e^2}{2mc^2} A^2 \tag{2.8}$$

If the magnetic field is uniform and along the z direction (usually can be regarded as the electron spin direction), the three components of the vector field $\mathbf{A}$ can be written as:

$$A_x = -\frac{1}{2} yB, A_y = \frac{1}{2} xB, A_z = 0 \tag{2.9}$$

Therefore, the equation (2.8) becomes[23]:

$$\mathcal{H} = \frac{ie\hbar B}{2mc}(x\frac{\partial}{\partial y} - y\frac{\partial}{\partial x} + \frac{e^2 B^2}{8mc^2}(x^2 + y^2) \tag{2.10}$$

In the right hand side of equation (2.10), the first term represents the energy contribution coming from the orbital angular momentum. The second term represents the energy contribution as:

$$E' = \frac{e^2 B^2}{12mc^2} \left\langle r^2 \right\rangle \tag{2.11}$$

Therefore, the associated magnetic moment can be written as[23]:

$$\mu = -\frac{\partial E'}{\partial B} = \frac{e^2 \left\langle r^2 \right\rangle}{6mc^2} B \tag{2.12}$$

which is in agreement with equation (2.7).

Paramagnetism

Just opposite to diamagnetism, materials with paramagnetism will feel positive contribution to the susceptibility when a magnetic field is applied. This positive contribution usually appears in free atoms or ions with partly filled inner shell, such as transition elements and rare earth ions. It also appears in metals and some compounds with an even number of electrons.

For one atom, the magnetic moment can be written as:

$$\vec{\mu} = \gamma \hbar \mathbf{J} = -g\mu_B \mathbf{J} \tag{2.13}$$

where γ is called the gyromagnetic ratio and $\hbar\mathbf{J}$ is the total angular momentum (includes both orbital and spin angular momentum). g is the Lande equation, which can be calculated by the angular quantum number:

$$g = 1 + \frac{J(J+1) + S(S+1) - L(L+1)}{2J(J+1)} \tag{2.14}$$

When a magnetic field is applied to the atom, the energy of it will be changed[22]:

$$U = -\vec{\mu} \cdot \mathbf{B} = m_J g \mu_B B \tag{2.15}$$

where μ_B is called Bohr magneton.

From equation (2.15), one can notice that the energy of the atom in the external field is related to the relative direction of magnetic moment and the field. Now consider a system with N atoms, which contains N_1 atoms with spin up and N_2 atoms with spin down ($N_1 + N_2 = N$). Therefore, one can get the ratios of spin up and spin down atoms as[22]:

$$\frac{N_1}{N} = \frac{exp(\mu B/k_B T)}{exp(\mu B/k_B T) + exp(-\mu B/k_B T)} \tag{2.16}$$

$$\frac{N_2}{N} = \frac{exp(-\mu B/k_B T)}{exp(\mu B/k_B T) + exp(-\mu B/k_B T)} \tag{2.17}$$

As a result, the magnetization of N atoms in this field can be written as:

$$M = (N_1 - N_2)\mu = N\mu tanh(\frac{\mu B}{k_B T}) \tag{2.18}$$

Generally, $\mu B/k_B T \ll 1$, therefore:

$$M = N\mu \frac{\mu B}{k_B T} \tag{2.19}$$

which contains a positive susceptibility. This is the so called paramagnetism.

2.2.2 Ferromagnetism

The word 'Ferromagnetism' is used to describe the strong attraction magnetic behavior. In some materials, the magnetic moments in atoms tend to align parallel to each other even when there is no external magnetic field. Pierre Weiss, in 1907, proposed that there existed a molecular field inside the material, which was formed

by all the atoms, that would induce the spontaneous magnetization. In the theory, Weiss assumed that the intensity of the molecular field is proportional to the total magnetization of the material:

$$\mathbf{H}_m = w\mathbf{M} \tag{2.20}$$

So with an external field, the average magnetization of the material is[23]:

$$\mathbf{M} = N\mathbf{m}\frac{\int_0^\pi exp\frac{\mathbf{m}(H+w\mathbf{M})}{kT}cos\theta sin\theta d\theta}{\int_0^\pi exp\frac{\mathbf{m}(H+w\mathbf{M})}{kT}sin\theta d\theta} = N\mathbf{m}L(\alpha) \tag{2.21}$$

where $L(\alpha)$ is called Langevin function and $\alpha = \frac{\mathbf{m}(H+w\mathbf{M})}{kT}$. In other words, the average magnetization can also be written as[23]:

$$\mathbf{M} = \frac{kT}{\mathbf{m}w}\alpha - \frac{H}{w} \tag{2.22}$$

Unlike diamagnetism, the ferromagnetism will change with temperature. When the temperature is higher than some certain value, the ferromagnetism is gone. This critical point is called Curie point, Θ_f. From equation 2.21, one can get:

$$\frac{\partial\mathbf{M}}{\partial\alpha} = \frac{N\mathbf{m}}{3} \tag{2.23}$$

While from equation (2.22), the value should be the same when the temperature $T = \Theta_f$. Thus[23]:

$$\frac{\partial\mathbf{M}}{\partial\alpha} = \frac{k\Theta}{\mathbf{m}w} \tag{2.24}$$

Therefore, the Curie temperature can be written as:

$$\Theta_f = \frac{Nm^2w}{3k} = \frac{(J+1)Nm^2w}{3Jk} \tag{2.25}$$

where J is the Brillouin function.

Typically, for iron, $\Theta_f = 1063K$, $\mathbf{m} = 2.2\mathbf{m}_b$, $N = 8.5 \times 10^{28} m^{-3}$ and $J = 1$. Put these values into equation 2.25, one can easily get:

$$w = \frac{3Jk\Theta_f}{(J+1)Nm^2} = 3.9 \times 10^8 \tag{2.26}$$

Therefore, the molecular field in iron is:

$$H_m = w\mathbf{M} = 0.85 \times 10^9 A/m \approx 1.1 \times 10^7 Oe \tag{2.27}$$

From this value, one can notice that the internal molecular field in the material can be quite large. Remember that usually the magnetic field in a lab is usually a few Tesla, which is much smaller than the value of the molecular field. Due to this strong internal field, the magnetic moments of each atom tend to align to one direction, even without the external field.

The molecular field is so large that classical theories can not explain the origin of it. In the year 1928, Heisenberg proposed that this enormously huge field came from the interaction in ferromagnetic materials. In quantum physics, electrons are fermions with spin $\frac{\hbar}{2}$, and the distribution of electrons follow the Pauli exclusion principle. Consider two atoms, each with a single unpaired electrons, approach each other. If the spin of the two electrons are antiparallel, they can share the same electron orbit. In other words, these two electrons can be quite close to each other, which will increase the Coulomb energy. However, if the two spins are parallel to each other, they can not stay in the same orbit due to the Pauli exclusion principle. That is to say that the distance of the two electrons are relatively far away, compared with the antiparallel case. Thus, the Coulomb energy can be lower. Assume that the distance between two electrons are about 1 $\mathring{A}$, so the Coulomb energy can be estimated as[23]:

$$E_c = \frac{e^2}{4\pi\varepsilon_0 r} = 2.1 \times 10^{-18} J \sim 1.4 \times 10^5 K \tag{2.28}$$

That is to say, if one wants to change the Coulomb energy by changing the temperature, one has to apply a temperature as high as 140000 K, which is impossible to realize. This explain why the magnitude of the molecular field is so large.

2.2.3 Antiferromagnetism and Ferrimagnetism

Like ferromagnetism, the spins in antiferromagnetism materials are also follow some certain alignment when the temperature is below a certain value. The difference is in ferromagnetism, the spins in the material tend to align parallel, while in antiferromagnetism material, the two neighboring spins tend to align antiparallel. The critical temperature below which the spins tend to align antiparallel, is called Neel temperature. Due to the special alignment of the spins, antiferromagnetism materials show no spontaneous magnetization and only have a feeble magnetism. The susceptibility of this kind of materials is usually between 10^{-5} to 10^{-2}, similar to that of the paramagnetism.

Materials with antiferromagnetism usually contain at least two elements. The first antiferromagnetic spin ordering was verified in the material MnO. The Mn ions form a fcc structure, while the O ions fall in the interstitial sites. Therefore, the direct interaction between two Mn ions is quite weak. The two spins in two neighboring Mn ions align antiparallel due to the superexchange interaction between the two Mn ion and on O ion between them. As is shown in the figure. The Mn^{2+} ion has five electrons outside the nucleus, thus one spin is unpaired. the electrons in the O^{2-} atom is $1s^2 2s^2 2P^6$, with six outside electrons in the $2p$ orbit. The p-orbit stretches towards the two nearby Mn^{2+} ions (M_1 and M_2). Assume that on of the p-electrons in the O^{2-} ion can transfer to the 3d orbit of the Mn^{2+} ion. Since the Mn^{2+} ion already has five electrons outside, the incoming electron should have a spin antiparallel to the Mn^{2+} spin. On the other hand, another electron in the O^{2-} ion must have a spin

antiparallel to the one that goes to the first Mn^{2+} ion, due to the Pauli exclusion principle. In this case, this electron will have exchange interaction with the second Mn^{2+} ion, M_2, making the two spins in M_1 and M_2 antiparallel. One thing to notice is that the superexchange interaction is the strongest when the three ions form an angle of π, and will become weaker when the angle decreases[22].

Ferrimagnetism has a spin arrangement similar with that of antiferromagnetism. In antiferromagnetism, the two neighboring spins come from the same element. While in ferrimagnetism, the two spins in the neighboring places come from different magnetic elements, or sometimes different number of atoms. Thus, the antiferromagnetic spin arrangement will produce spontaneous magnetization in the material. The mechanism of ferrimagnetism is also through the superexchange interaction with a third non magnetic atom.

2.3 Magnetic Domain Walls

2.3.1 Domain Energy

Ferromagnetic materials have spontaneous magnetization, However, if one puts two pieces of iron together, they will not attract or repel each other. That is to say, the iron does not show any magnetization, without any external magnetic field. In the year 1907, Weiss pointed out that the magnetic moments in a ferromagnetic material are not necessarily point to one direction without external field because the spontaneous magnetization takes different direction in different domain. This is the first proposal of domain in ferromagnetism[22, 24].

In 1919, Barkhausen discovered the magnetization process in ferromagnetic material is not continuous; instead, this process always happen with many discrete steps. This is the so called Barkhausen effect. He proved his idea by connecting a speaker on

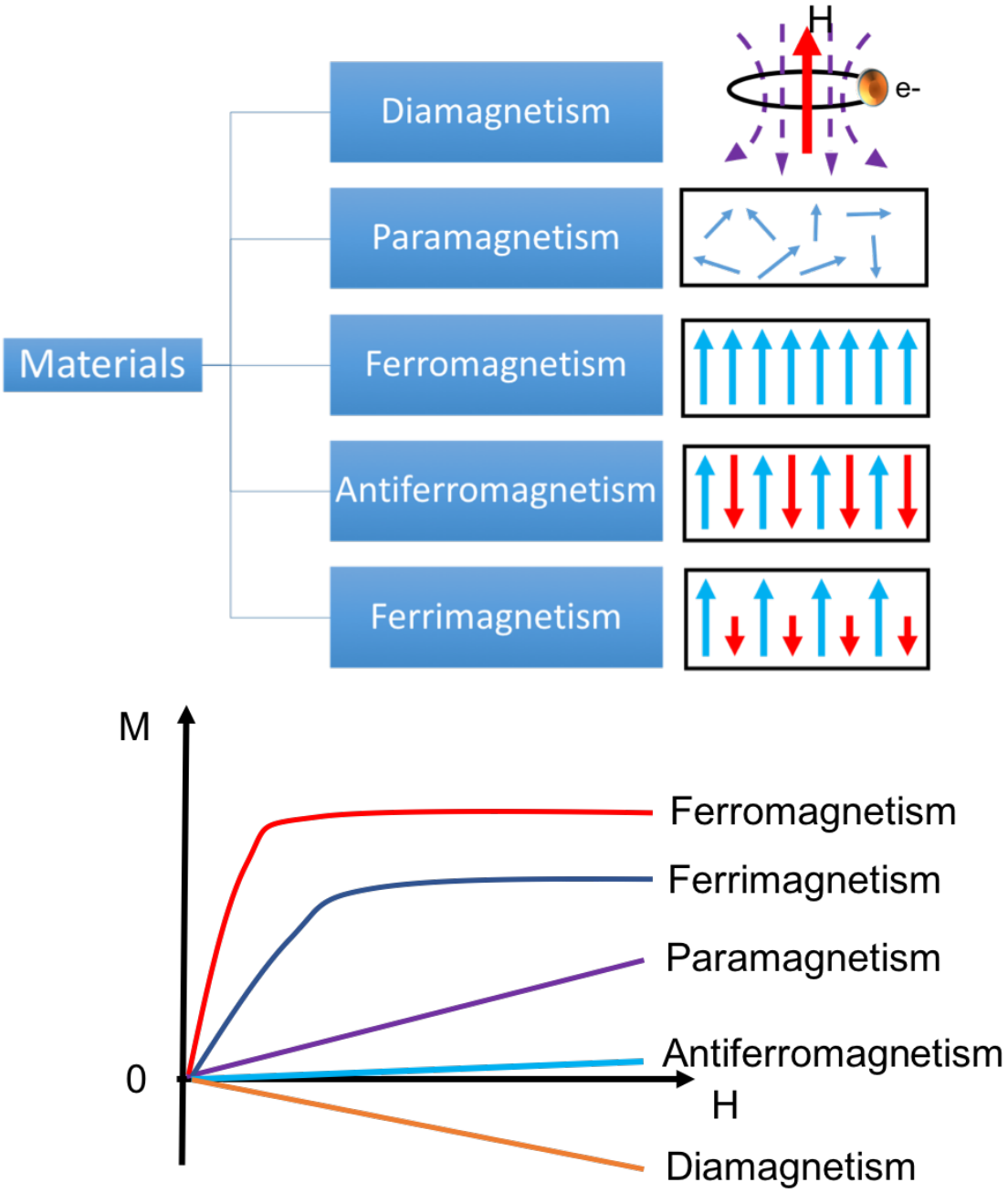

Figure 2.1: Top: Five common magnetism and their magnetic moments alignment with external field; Bottom: M-H curve for the five different magnetism.

a coil, which was wrapped on a piece of ferromagnetic material. From the speaker, he could hear the roaring noise like the sound from the seashore when he use a magnet to magnetize the specimen. This noise is called Barkhausen noise. This is the first direct proof of discontinuous magnetization process[22, 25].

The first direct observation of magnetic domain structure under a microscope was made by Bitter in 1931[22]. He put colloidal ferromagnetic particles on the top of a well polished magnet surface and used a reflecting microscope to observe the position of those particles. Interestingly, he found that the particles tend to form clusters on different locations on the magnetic. This is because in the magnet, there exist many domains and they are separated by domain walls. The ferromagnetic particles will be attracted by the magnetization in different domains and thus form clusters.

Consider a piece of infinitely long ferromagnetic specimen is put in a magnetic field, the direction of which is along the long axis of the sample. When the specimen is fully magnetized, it will have a single domain. If the sample has a finite size, there will be free magnetic poles at the surface, which will increase the magnetostatic energy. To reduce this energy, the spin distribution has to be altered so that the free poles on the surface can decrease. Usually, for a magnetic sample, the total energy in the specimen have four parts[22]:

$$U = U_{mag} + U_{ex} + U_{mc} + U_{me} \tag{2.29}$$

where U_{mag} is the magnetostatic energy, U_{ex} is the exchange energy, U_{mc} is the magnetocrystalline energy and U_{me} is the magnetoelastic energy. To reach a stable state, the total energy should be minimized.

Consider a ferromagnetic disk with radius r and thickness d, and has been magnetized along one direction, as is shown in figure(2.2)[22]. In this case, the magnetostatic energy is:

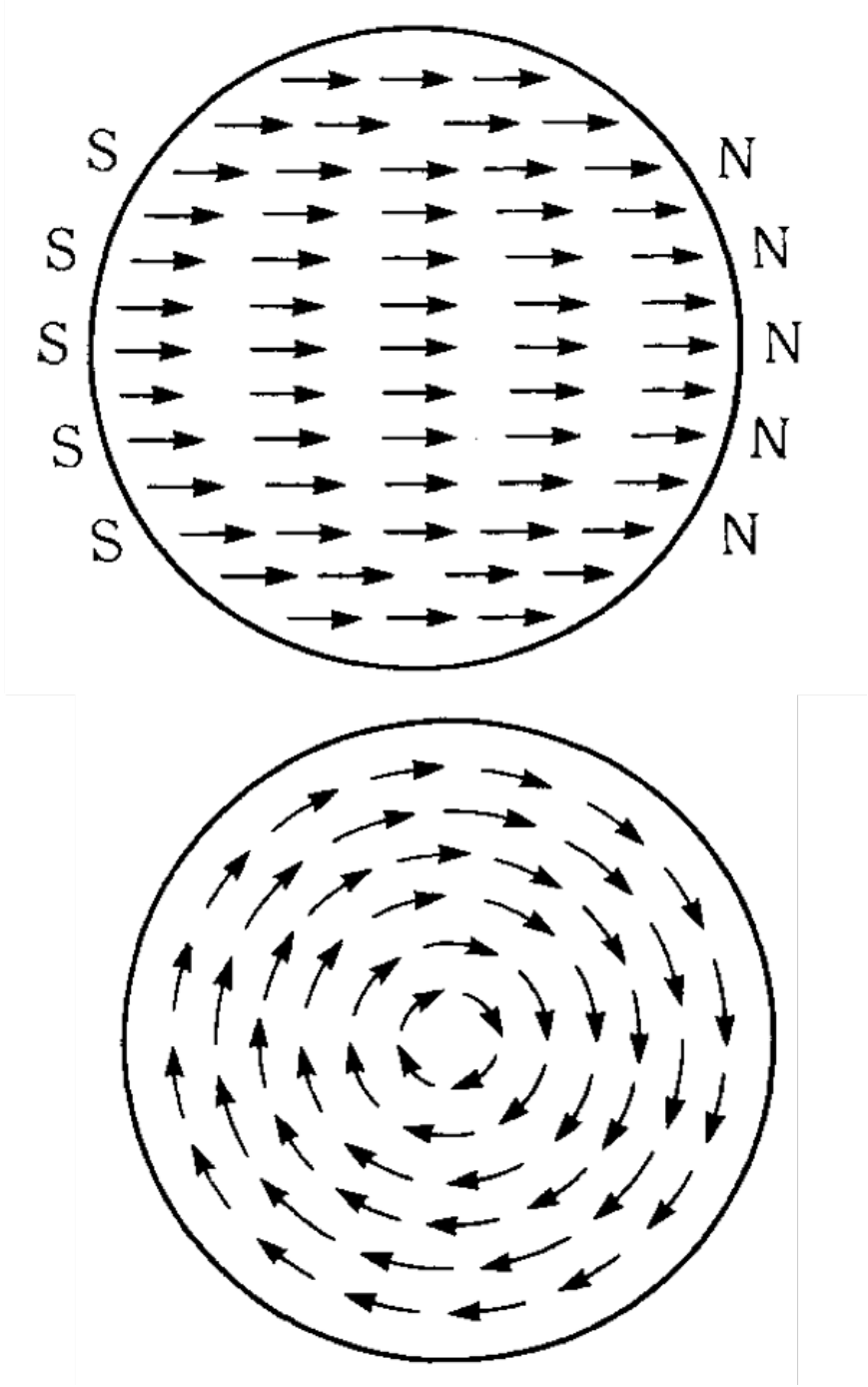

Figure 2.2: Top: Ferromagnetic disk with uniform magnetization; Bottom Ferromagnetic disk with circularly magnetization.[22]

$$U_{mag} = \frac{1}{2\mu_0} N M^2 V \tag{2.30}$$

where $V = \pi r^2 d$ is the volume of the magnetic disk, N is the demagnetization factor. To reduce this energy, the magnetic moments inside the disk will change their directions. One of the possibility is that they will form a circularly magnetization, which will enable that there is no free poles on the surface of the sample, so that $U_{mag} = 0$. In this case, the angle between two neighboring spins are not zero; instead, they will have a small angle, which will store a small amount of exchange energy:

$$w_{ij} = -2J\mathbf{S}_i \cdot \mathbf{S}_j \tag{2.31}$$

where J is called exchange integral and it is positive for ferromagnetism and negative for antiferromagntism. If the angle between neighboring two spins are quite small, this energy can be written as:

$$w_{ij} = -2JS^2 cos\varphi \simeq JS^2\varphi^2 + const \tag{2.32}$$

In the material, assume one spin has z nearest neighborhoods. In this case, the total exchange energy can be written as[22]:

$$\sum_{j+1}^{z} wij = -JS^2 \sum_{j=1}^{z} (\alpha \frac{\partial^2 \alpha}{\partial x^2} x_j^2 + \alpha \frac{\partial^2 \alpha}{\partial y^2} x_j^2 + \alpha \frac{\partial^2 \alpha}{\partial z^2} z_j^2) \tag{2.33}$$

In a cubic lattice, $\sum_{j=1}^{z} x_j^2 = \sum_{j=1}^{z} y_j^2 = \sum_{j=1}^{z} z_j^2$, therefore, the exchange energy density can be simplified to:

$$E_{ex} = -\frac{nJS^2}{a} (\alpha \cdot \frac{\partial^2 \alpha}{\partial x^2} + \alpha \cdot \frac{\partial^2 \alpha}{\partial y^2} + \alpha \cdot \frac{\partial^2 \alpha}{\partial z^2}) \tag{2.34}$$

In a cylindrical coordinate, this energy density can be written as[22]:

$$E_{ex} = A\{(\frac{\partial\alpha}{\partial r})^2 + \frac{1}{r^2}(\frac{\partial\alpha}{\partial\theta})^2 + (\frac{\partial\alpha}{\partial z})^2\} \tag{2.35}$$

where $A = \frac{nJS^2}{a}$ is called exchange stiffness constant. So the total exchange energy can be calculated as:

$$U_{ex} = 2\pi d \int_0^r rE_exdr = \frac{2AV}{r^2} ln(r) \tag{2.36}$$

From this equation, one can see that the exchange energy density increases as the radius decreases.

In ferromagnetic crystals, there exist the magnetocrystalline energy, which is different at different crystal direction, based on the direction of the easy axis. When the crystal anisotropy is large, the spins will tend to align to the easy axis, instead of forming a circular domain. The domain structures for a disk specimen with cubic anisotropy and uniaxial axial anisotropy are shown in the figure (2.3)[22]. From the figure one can see that there exist free magnetic poles at the surface of the sample, which means there is some magnetostatic energy stored. Neighboring domains are separated by a wall named domain wall, and the energy stored in the wall is called domain wall energy.

2.3.2 Domain Walls

As is stated in the previous section, in a ferromagnetic specimen, neighboring domains are separated by domain walls. The direction of spins in the domain wall change from the direction of the first domain to the direction of the second domain, within the domain wall. If the spins in the two domains are complete opposite to each other, the domain wall is called 180° wall. All the other kind of domain walls, no matter what the real angle between the spins of the two domains is, are called 90° wall.

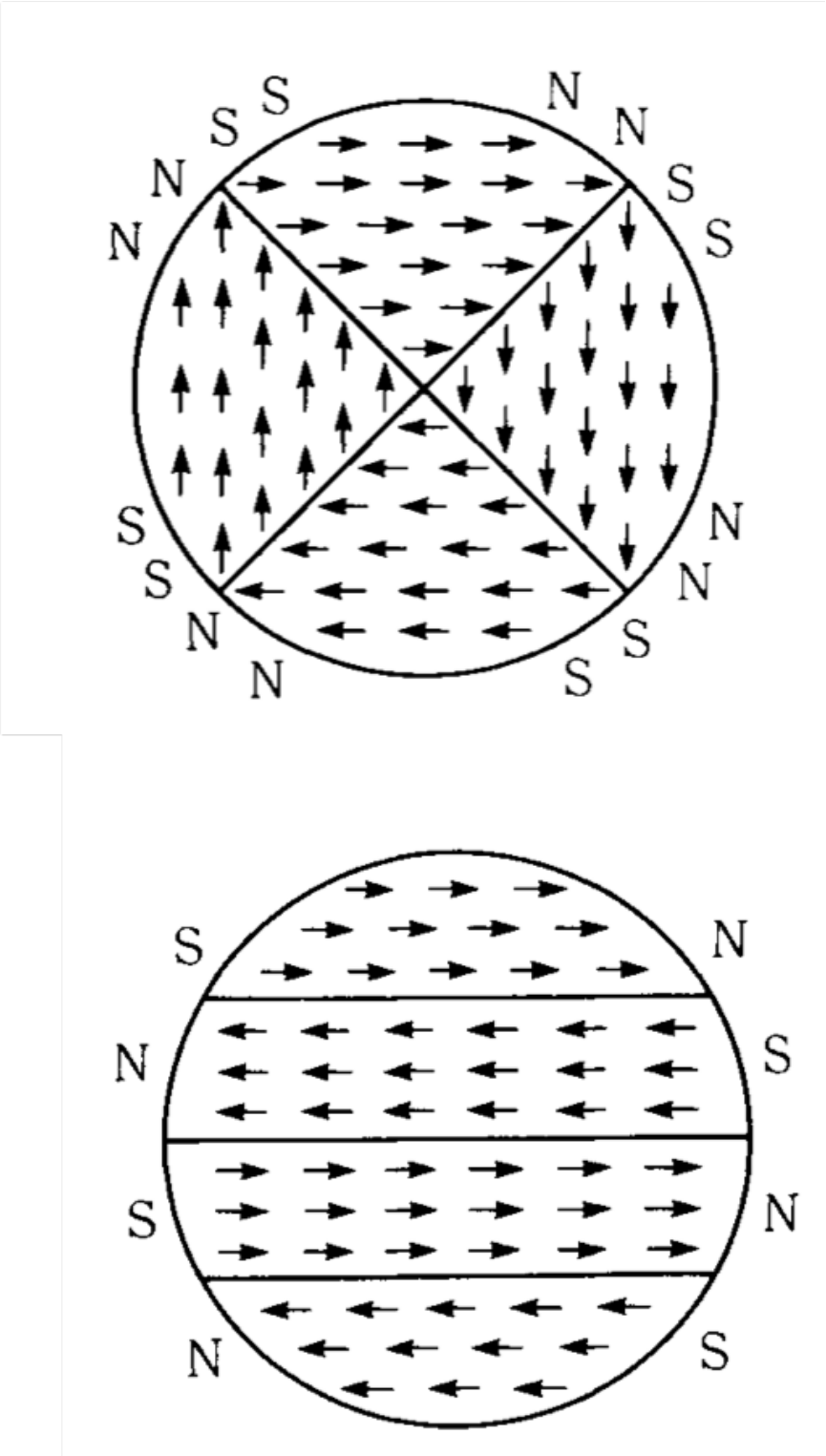

Figure 2.3: Top Domain structure for cubic anisotropy material; Bottom: Domain structure for uniaxial anisotropy material.[22]

Bloch Wall

Bloch wall is one type of 180° wall. When two domains are separated by Bloch wall, the spins in the wall will gradually change from the direction of one domain to the direction of another domain, with the change of spin out of the plane. Usually, the energy of the domain wall contains two parts: anisotropy energy and exchange energy. Consider a Bloch wall in a simple cubic structure (lattice constant is a), with N atom layers in the wall. So the angle between two spins in the neighboring atom layer is π/N. So the exchange energy can be calculated by[22]:

$$\gamma_{ex} = \frac{N}{a} w_{ij} = \frac{JS^2\pi^2}{a^2 N} \tag{2.37}$$

On the other hand, the spins in the domain wall deviate from the easy axis. Therefore, the anisotropy will raise:

$$\gamma_a = KNa \tag{2.38}$$

where K is the anisotropy constant and N is the number to atom layers in the domain wall.

So the total energy that is stored in the domain wall is:

$$\gamma = \gamma_{ex} + \gamma_a = \frac{N}{a} w_{ij} = \frac{JS^2\pi^2}{a^2 N} + KNa \tag{2.39}$$

To reach a stable state, the energy should be minimized. Therefore, the thickness of the wall can be calculated by:

$$\delta = Na = \pi\sqrt{\frac{JS^2}{Ka}} \tag{2.40}$$

For iron, $J = 2.16 \times 10^{-21}, S = 1, K = 4.2 \times 10^4, a = 0.286nm$, therefore, the domain wall thickness is about $\delta = 150$ *lattice constants*[22].

Neel Wall

Neel wall is another kind of 180° wall. Unlike the Bloch wall, the spins in Neel wall will gradually change the direction in plane. In a very thin sample, if two domains are separated by a Bloch wall, since the spins in the wall will change directions out of plane, there will be magnetic free poles on the surface of the sample. In bulk material or very thick sample, this magnetostatic energy, which is caused by the free poles, may be negligible, compared with other energy. However, in very thin film, the contribution of this energy can be quite large to the total domain wall energy. Thus, in these samples, the Bloch walls are not preferred. So Neel pointed out that if the rotations of spins are in a plane parallel to the thin film the magnetostatic energy will be much smaller, which is called Neel domain wall. Theoretical calculations show that the wall energy of Neel wall is[22]:

$$\gamma = 4\sqrt{A(K_u + \frac{M^2}{2\mu_0})} \tag{2.41}$$

where M is the magnetization. Usually, the energy stored in Neel wall is higher than that in the Bloch wall. However, when the sample is very thin, the magnetic free poles on the surface of the film will increase the magnetostatic energy in the Bloch wall. On the other hand, the energy of Neel wall will tend to decrease with the decreasing of the thickness of the film, since the demagnetization factor, N in equation (2.41) decreases with thickness. Therefore, the Bloch wall is more stable for thick film, while the Neel wall is more preferable for thinner film. For thin films with thickness not too thin nor too thick, the energy of Bloch wall and Neel wall are comparable. In this case, the direction of spins will change discontinuously.

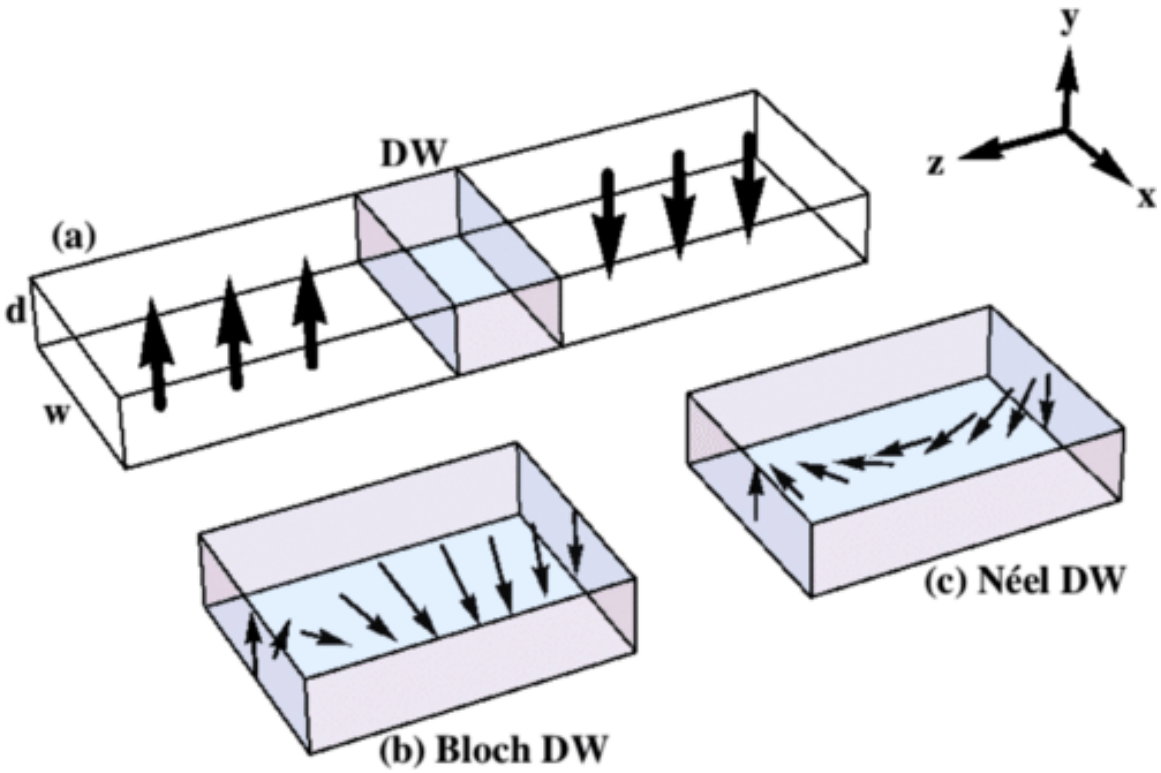

Figure 2.4: Left: Bloch wall, the spins in the wall change their directions out of plane; Right: Neel wall, the spins change directions in plane[26]

2.4 Domain Structures

In ferromagnetic and ferrimagnetic materials, there exist many domains when they are not fully magnetized. The magnetization of each domain points to different direction, in order to reduce the total magnetostatic energy. Assume the domains are stripes, so generally, this energy is proportional to the width of the domain, d. If d decreases, the negative free poles are more closely to the positive free poles, making the magnetostatic energy even smaller. However, when the width decreases, more domain walls will appear in the material, which will store more energy in the wall. Therefore, at equilibrium the size of the domain wall is determined by minimizing the summation of domain energy and the wall energy.

Consider a ferromagnetic plate, with thickness l. When the plate is fully magnetized, the magnetization if $\mathbf{M}$, so that the total energy stored per unit area is given by[22]:

$$\varepsilon_1 = \frac{M^2}{2\mu_0} l \tag{2.42}$$

When the sample is not fully magnetized, there will be many small domains inside. Assume all the domains have equal size, with the width $= d$, and the thickness of the sample, l, is large enough that the interactions between poles on the top and the bottom can be negligible. Therefore, the total energy in this case can be calculated by[22]:

$$\varepsilon_2 = 1.08 \times 10^5 M_0^2 d \tag{2.43}$$

where M_0 is the magnetization in each domain. On the other hand, the total wall energy can be written as:

$$\varepsilon_w = \frac{\gamma l}{d} \tag{2.44}$$

where γ is the energy per wall. Thus, the total energy is the summation of domain energy and wall energy:

$$\varepsilon = 1.08 \times 10^5 M_0^2 d + \frac{\gamma l}{d} \tag{2.45}$$

To minimize the total energy, the width of each domain has to ba:

$$d = 3.04 \times 10^{-3} \frac{\sqrt{\gamma l}}{M} \tag{2.46}$$

Iron has bcc structure. Assume all the domain walls are along the (100) direction. So the wall energy is $\gamma_{100} = 1.6 \times 10^{-3}$. So the domain width for a iron sample with thickness 1 cm is about $d = 5.6 \times 10^{-6} m$, and the total energy for this sample is $\varepsilon = 5.63 J/m^2$, which is much smaller than that of a iron sample with one single domain ($\varepsilon = 1.8 \times 10^4 J/m^2$). This is why when there is no external field applied to the sample, it tends to form several domains inside[22].

If the thickness is not large enough, the free poles on top and bottom of the sample will interact with each other, storing extra magnetostatic energy. In this case, there will be another smaller domain forming on the surface of the sample, which will make close magnetic loops with the domains inside the sample. In general, the closure domains tend to elongate parallel to the crystal surface if the magnetostriction constant is positive, and shrink when that factor is negative. On the other hand, the closure domains have to be compressed into a triangular shape, in order to accommodate the major domains. An example of well defined domains are shown in figure (2.5)[23].

In previous discussions, all the domains are supposed to be stripes. However, in some magnetic structures, there exists another kind of domains: bubble domains.

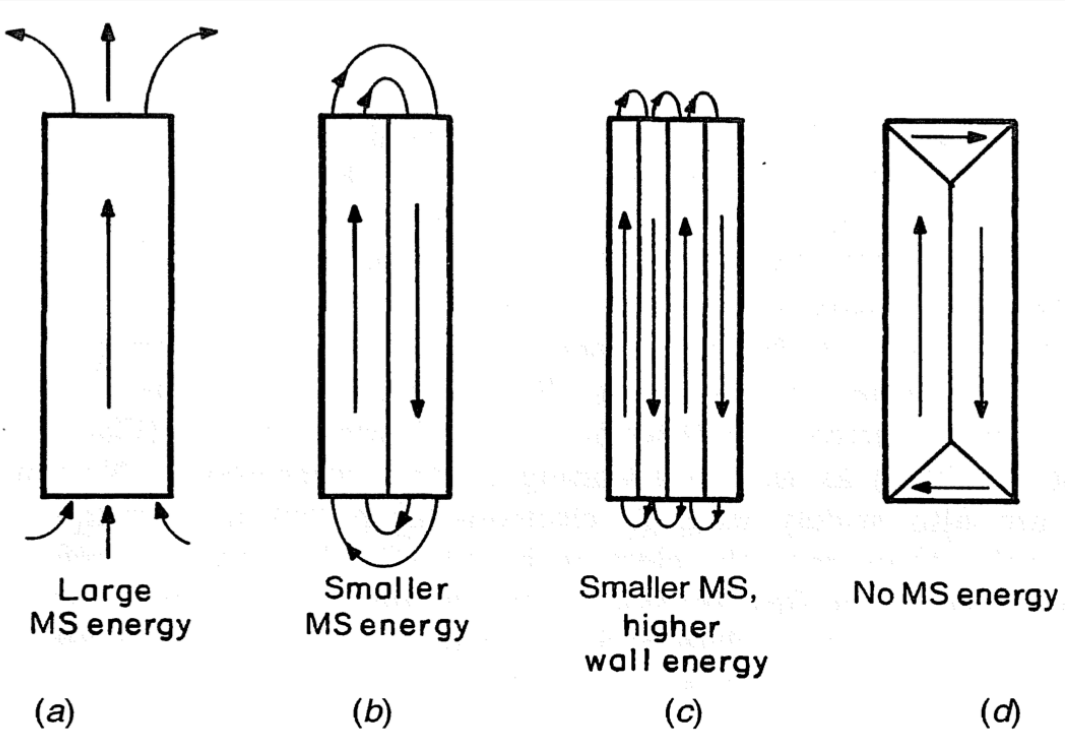

Figure 2.5: (a): A single domain structure will have large magnetostatic energy. (b): When there is one domain wall appears in the middle, the magnetostatic energy will be smaller. (c): When there are more domain walls, the magnetostatic energy will be even smaller, however, the wall energy will be larger. (d). A closure domain wall structure will have zero magnetostatic energy and the total energy is minimized.[23]

This kind of domain often appears when the magnetization direction is out of the surface plane, namely the sample with perpendicular magnetic anisotropy (PMA). In PMA structures, there exists magnetic free poles on the surface. So for bubble domains, the interaction between positive poles and negative poles tend to increase the radius of the domain. However, when the radius increases, the domain wall area also increases, which will lead to an increase in the domain wall energy. Therefore, in order to reach a stable state, a bias field has to be applied[22]:

$$H_d + H_\gamma = H_b \tag{2.47}$$

where H_d is the demagnetization field in the bubble, H_γ is the hypothetical field created by the pressure from the sample to the domain wall, and H_b is the applied bias field. When the bias field is applied, the bubble shrinks. One potential application of bubble domains is to make magnetic memory. The bubble will transfer along a circuit, patterned on a single crystal plate. The magnetization in the bubble is different from that of the outside area, which can be detected by measuring the change of resistance, through the magnetoresistance effect. Thus, a '0' or '1' can be read when the bubble is moving. However, there is a special bubbles, whose radius is insensitive to the bias field, H_b. This is called hard bubble, which is unsuitable to make magnetic memory. One way to remove the hard bubbles is to deposit a thin layer of soft magnetic layer on the crystal, or use ion bombardment to process the surface, in order to remove any complicated spin structures.

Chapter 3

SUPERCONDUCTIVITY

3.1 Discovery of Superconductivity

The superconductivity phenomenon was discovered by Professor Heike Kamerlingh Onnes in 1911, three years after he liquified the helium and reached a temperature about 4.2 K. The first material that was determined to have superconductivity was mercury (Hg), which was chosen due to the high purity that obtained by repeated distillation [27].

Besides the zero resistance, superconductivity also has some other interesting behaviors. In 1933, Meissner and Ochsenfeld found that superconductors were perfect diamagnetism, which was the so-called Meissner effect[28]. Magnetic field will be excluded from entering the superconductor, and, on the other hand, the magnetic field in normal materials will be expelled from it when the temperature drops below a certain temperature, called critical temperature, T_c. More interestingly, when the magnetic field increases, the superconductivity will disappear at some point. This field is called thermodynamic critical field (H_c). Experimentally, people found that the critical field will change with temperature with the following equation:

$$H_c(T) \approx H_c(0)[1 - \frac{T}{T_c}]^2 \tag{3.1}$$

From the equation, one can see that when the temperature increases, the critical field will decrease. In many conventional superconductors, equation(3.1) can well describe the change of critical with temperature. However, in some materials, there exist two critical field, H_{c1} and H_{c2}. And there exist a mixed states between the two

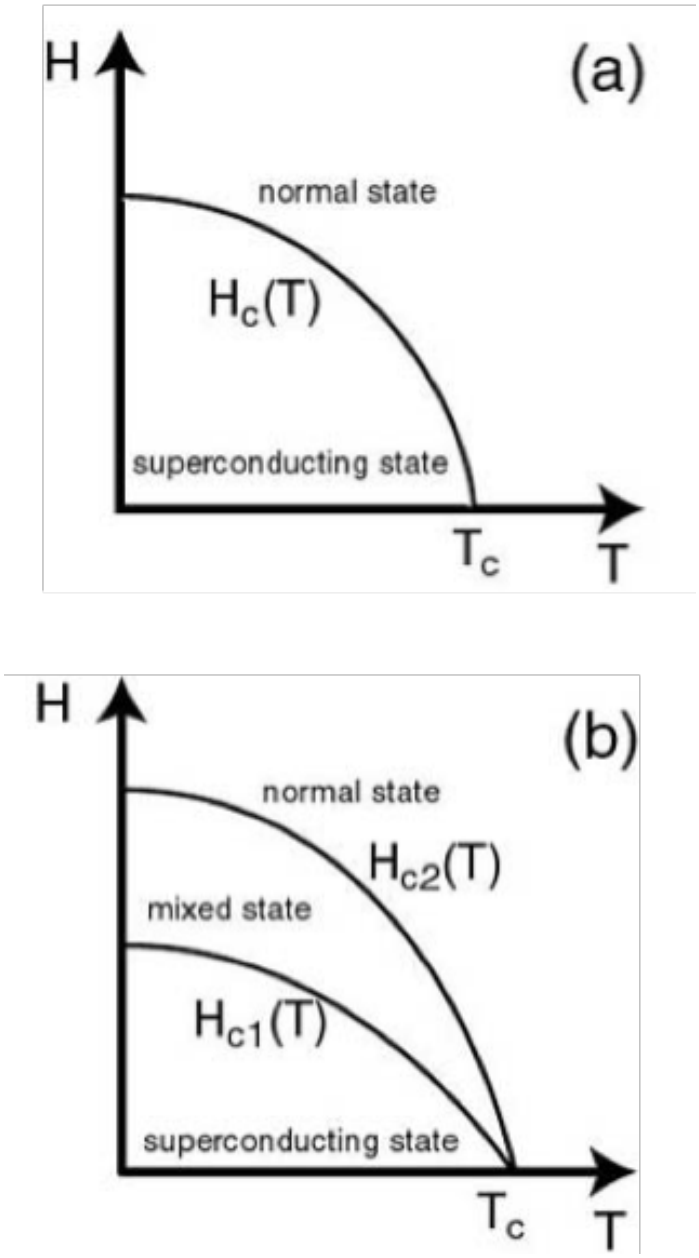

Figure 3.1: Critical field vs. Temperature for type I and II superconductors. (a): For type I superconductor, there is only 1 critical field. And the superconductor has two states: normal state and superconducting state. (b): For type II superconductor, there exist two critical field, H_{c1} and H_{c2}, so that there are three states: normal state, superconducting state and mixed state.[29]

fields, as is shown in figure(3.1)[29].

Since the discovery of superconductivity, scientists were trying to explain the mechanism of this astonishing behavior. And there came many different theories.

3.2 London Equation

In 1935, Fritz London and Heinz London developed the famous London equations. These equations successfully explained some electrodynamic phenomena of superconductors, such as the Meissner effect[29].

Since there is no resistance in superconductor, one needs to assume that there are n_s electrons in unit volume. Thus, the super current caused by these electrons can be written as[29]:

$$\frac{\partial \mathbf{j}_s}{\partial t} = -n_s q \frac{\mathbf{v}}{t} = \frac{n_s q^2}{m}\mathbf{E} \tag{3.2}$$

where $\mathbf{j}_s$ is the super current density, q is the charge, and $\mathbf{v}$ is the velocity of the electrons under the influence of the applied electric field $\mathbf{E}$. On the other hand, due to Maxwell's equation,

$$\nabla \times \mathbf{E} = -\frac{\partial \mathbf{B}}{\partial t} \tag{3.3}$$

One can get:

$$\nabla \times \mathbf{j}_s = -\frac{n_s q^2}{m}\mathbf{B} \tag{3.4}$$

Define a constant, $\Lambda = \frac{m}{n_s q^2}$ and consider that $\nabla \times \mathbf{B} = \mu_0 \mathbf{j}$, one can find the following relation:

$$\nabla^2 \mathbf{B} = \frac{\mu_0}{\Lambda}\mathbf{B} \tag{3.5}$$

Solving equation(3.5), one can get the magnetic flux:

$$\mathbf{B} = \mathbf{B}_0 e^{-\frac{x}{\lambda}} \tag{3.6}$$

where $\lambda = -\sqrt{\frac{\Lambda}{\mu_0}}$ is called the London penetration depth. This indicates that the magnetic field will decay exponentially in the superconductor, which is the Meissner effect.

3.3 The Ginzburg-Landau theory

To understand the mechanism of superconductivity, Vitaly Lazarevich Ginzburg and Lev Landau introduced a complex pseudowavefunction, ψ based on the Landau's second-order phase transition theory. This theory was proposed in 1950, known as Ginzburg-Landau theory (GL theory)[30]. Based on the theory, the local density of the superconducting electrons would be:

$$n_s = |\psi(x)|^2 \tag{3.7}$$

Assuming that $|\psi|$ and $\nabla\psi$ are small, the free energy in the superconductivity state can be expressed as:

$$F = F_n + \alpha|\psi|^2 + \frac{\beta}{2}|\psi|^4 + frac12m^*|(-i\hbar\nabla - 2e\mathbf{A})\psi|^2 + \frac{B^2}{2\mu_0} \tag{3.8}$$

where F_n is the free energy in the normal state, α and β are constants, m^* is effective mass, $\mathbf{A}$ is the magnetic vector potential and and $\mathbf{B}$ is the magnetic flux. By minimizing the free energy, one gets the Ginzburg-Landau equations:

$$\alpha\psi = \beta|\psi|^2\psi + \frac{1}{2m^*}(-i\hbar\nabla - 2e\mathbf{A})^2\psi = 0 \tag{3.9}$$

$$\mathbf{J} = \frac{2e}{m} Re\{\psi^*(-i\hbar\nabla - 2e\mathbf{A})\psi\} \tag{3.10}$$

With these equations, two features of superconductivity were treated, (1), nonlinear effects of strong field and (2) the spatial variation of ns. And this theory successfully explained intermediate state of superconductors, in which both superconductivity and normal states exist when the external field $H \approx H_c$.

As is shown in the figure, $\xi(T)$ is the coherence length, which is introduced in the GL theory:

$$\xi(T) = \frac{\hbar}{\sqrt{|2m^*\alpha(T)|}} \tag{3.11}$$

which describes the distance the wavelength $\psi(\mathbf{r})$ does not change when energy increases.

Together with the penetration depth ($\lambda = -\sqrt{\frac{\Lambda}{\mu_0}}$), the GL parameter is defined as

$$\kappa = \frac{\lambda}{\xi} \tag{3.12}$$

which is almost independent of temperature. When $\kappa \ll 1$, the surface energy associated with the domain wall between the superconductor and normal metal is positive. This defines the type I superconductor. In this kind of superconductors, the magnetic flux will sharply increases from zero to a large value when the external field reach the critical field H_c. While on the other hand, when $\kappa \gg 1$, the surface energy becomes negative, which defines the type II superconductor. This type II superconductor was found by Abrikosov in 1957. His results showed that when $\kappa > \frac{1}{\sqrt{2}}$, there would be an increasing amount of magnetic flux inside the superconductor when the external field increased to the critical field (which is called H_{c1}). And the

superconductivity will disappear if the field keeps increasing to some value (which is called H_{c2}).When the field H satisfies $H_{c1} < H < H_{c2}$, the material is at the intermediated state. In this state, the magnetic flux can penetrate into some domains, while be expelled in other places (figure(3.2))[31]. The flux carried in those domains is:

$$\Phi_0 = \frac{hc}{2e} \tag{3.13}$$

3.4 The BCS theory

Both the London theory and GL theory are phenomenological, and neither of them explained the microscopic mechanism of superconductivity. Until 1957, a theory based on the research of John Bardeen, Leon Cooper and John Robert Schrieffer formed the fundamental of the microscopic theory of superconductivity, called the BCS theory[28].

This BCS theory was inspired by the isotope effect discovered in 1950, by Frohlich. Experimental results showed that the critical temperature T_c for the isotopes of the same superconductivity element had the following relation:

$$T_c \propto M^{-1/2} \tag{3.14}$$

Where M is the mass of the atom of isotope. This effect indicated that the microscopic mechanism of superconductivity would be the interaction between electrons and lattice vibration.

The BCS theory was based on the assumption that the superconductivity appeared because the electrons form a special state - Cooper pairs. In classical mechanics, the electrons will be expelled from each other because of the Coulomb force. However, in quantum mechanics, when considered the electron - phonon interaction, the force

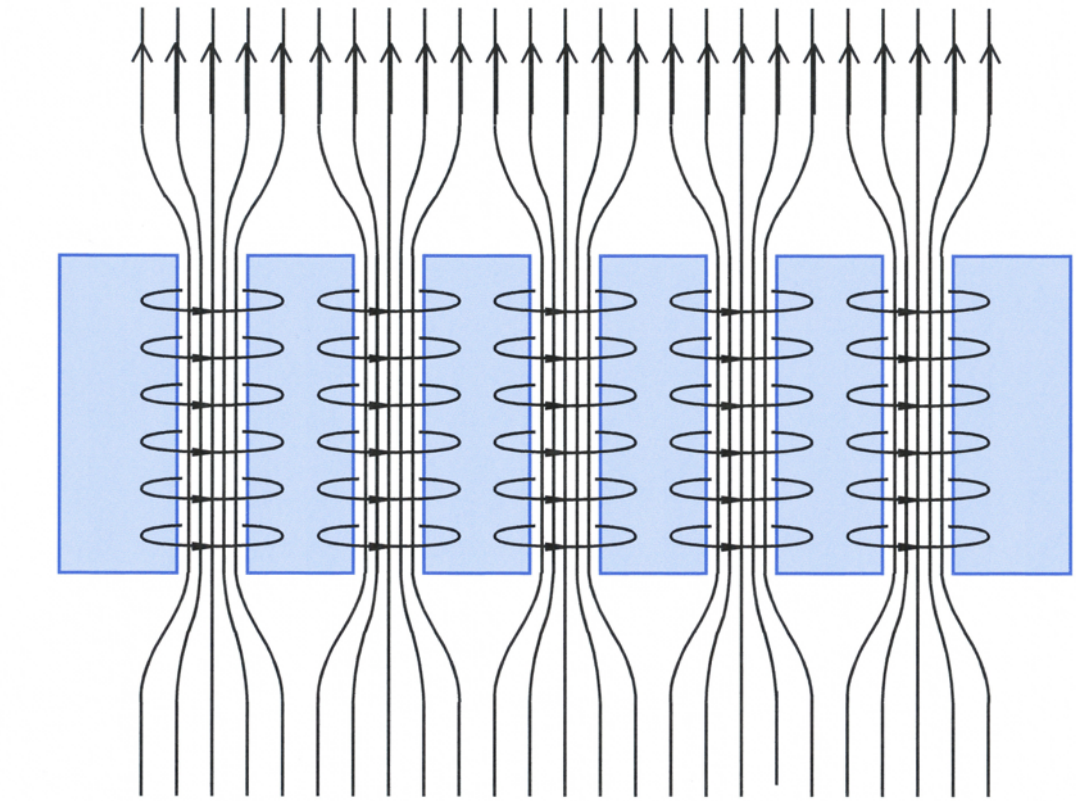

Figure 3.2: For type II superconductor, when the magnetic field is larger than H_{c1}, some part of the superconductor will be become normal state, and magnetic field can penetrate through these areas.[31]

between two electrons could be attractive (figure(3.3)), resulting in a negative potential.

In the normal state, the electrons in the material will obey the Fermi distribution and form a Fermi sphere. While in superconducting state, electrons inside the Fermi sphere, namely $E < E_F$, will remain the same as in the normal state. However, the electrons around the Fermi surface, with opposite momentum and spin, will bind together and form Cooper pairs.

At $T = 0K$, all the electrons close to the Fermi surface will form Cooper pairs, which is called the ground state. To break the Cooper pair, a minimum energy 2Δ is required, which means there would not be any energy state between the ground state and 2Δ. This is the evidence of the band gap in superconductors. According to BCS theory, the band gap can be written as:

$$\Delta = 2\hbar\omega_L e^{-\frac{1}{N(E_F)G}} \tag{3.15}$$

where $\hbar\omega_L$ is the average energy of the phonons, $N(E_F)$ is the density of state in the Fermi level, and G is the electron-phonon coupling efficiency. From the equation, we can see that if $N(E_F)$ and G are larger, the superconducting gap will be larger, which means it is easier to get superconductivity.

As was mentioned above, the superconductivity will disappear when the temperature increase from 0 K to T_c. This indicates that the band gap will change with temperature. The BCS theory gives the relation:

$$\Delta(T) = 3.07 k_B T_c \sqrt{1 - \frac{T}{T_c}} \tag{3.16}$$

Figure(3.4)[32] shows the band gap behavior for three different materials. One can see clearly that the results fit the BCS theory very well.

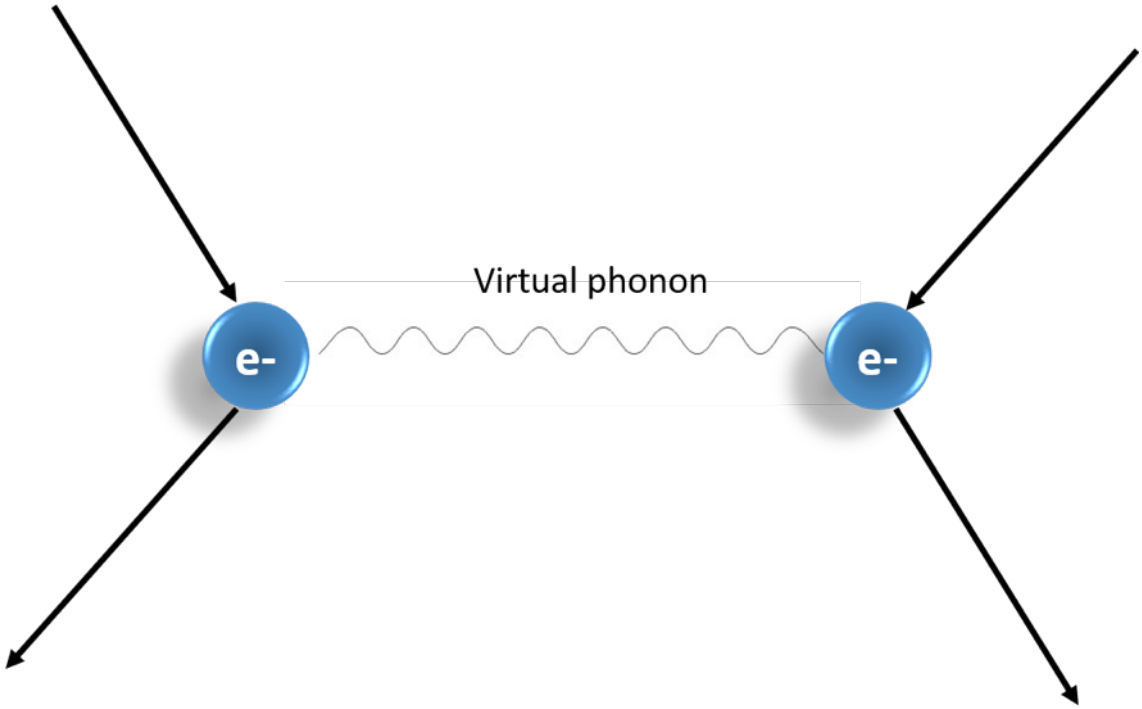

Figure 3.3: Two electrons will have attraction force due to the electron-phonon interaction

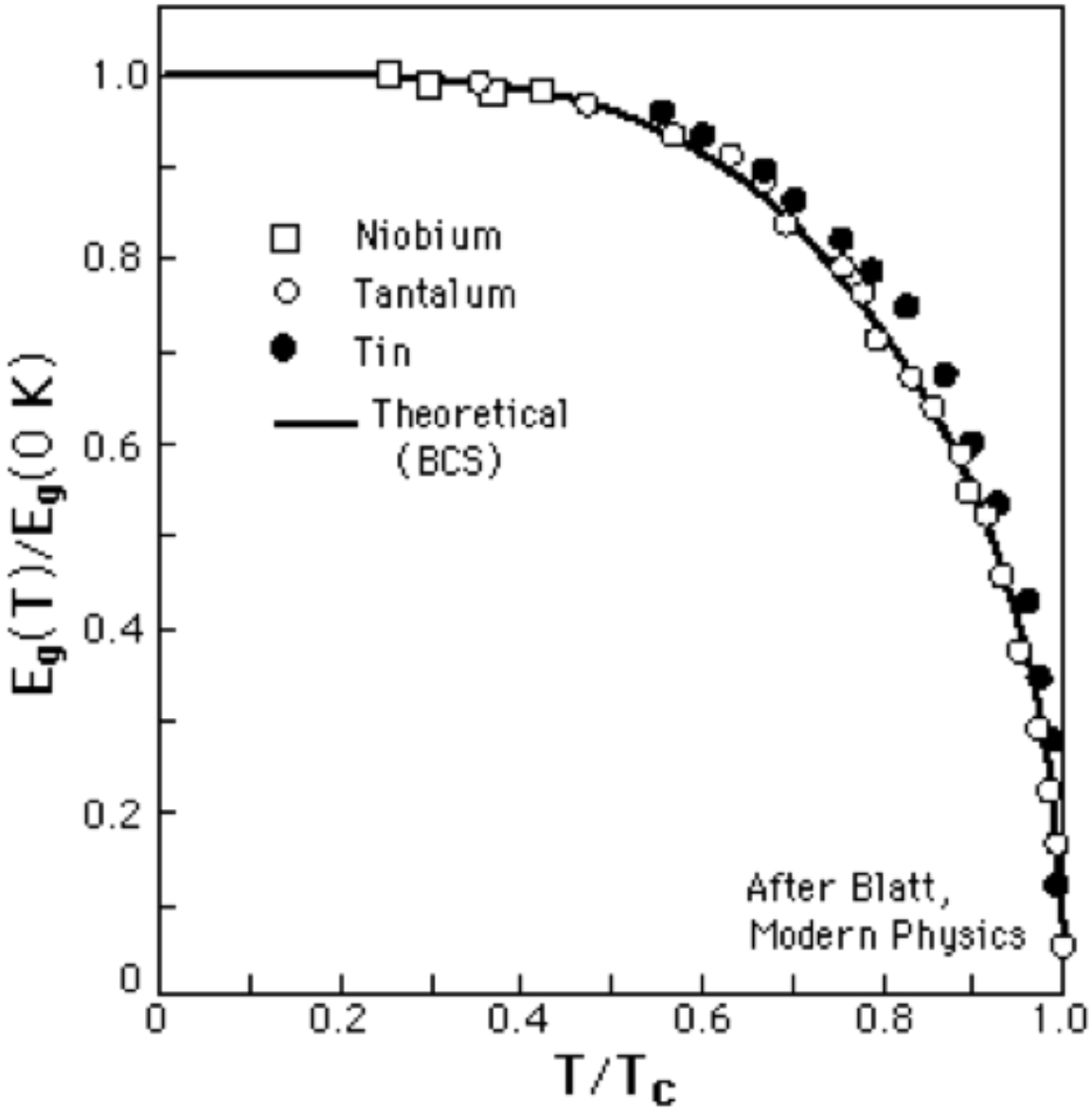

Figure 3.4: Experimental results of the band gap vs temperature relations for Ni, Ta and Sn. The experimental data fits very well with the BCS theory.[32]

The electrons in the Cooper pairs can not be treated as tightly bind pair. The attractive potential between the electrons in each pair is very weak. In quantum mechanics, the uncertainty principle points out that the uncertainty of momentum is $\Delta P \sim \frac{\hbar}{\xi}$, where ξ is the spatial range of one Cooper pair, therefore, the uncertainty of the kinetic energy is:

$$\Delta E = \Delta(\frac{p^2}{2m}) = \frac{p_F \hbar}{m\xi} \tag{3.17}$$

The Cooper pair could form only if $\Delta E < \Delta(0)$, where $\Delta(0)$ is the band gap at T = 0K. In this case, we have:

$$\xi \geq \xi_0 = \frac{\hbar p_F}{\Delta(0) m} \tag{3.18}$$

where ξ_0 is defined as the BCS coherence length. Numerically, ξ_0 $sim 10^{-4} cm$, which is several order larger than the lattice constant. This indicates that two electrons far away will form a Cooper pair, and different pairs will couple with each other. When the temperature changes, the electrons distribution will change, which results in a change of the superconducting band gap. When send a current into a superconductor, all the Cooper pairs will move to the same direction, with the same momentum. In this case, there will be no electron scattering, which results in a zero resistivity. When the current is larger than I_c, the energy will be large enough to break the Cooper pairs into single electrons. In this case, the electrons will be scattered by the lattice when they are moving inside the material, and they do not have the same momentum any more. Thus, the superconductivity will disappear. With BCS theory, more macroscopic phenomena, such as Meissner effect, the specific heat, can be well understood.

Chapter 4

SPIN POLARIZATION AND ANDREEV REFLECTION

4.1 Spin Polarization

The spin of electron generates magnetic moment. Since electrons are fermions, only the electrons that are around the Fermi level can participate in conduction. In non-magnetic metals, the number of spin-up and spin-down electrons are the same. Therefore, the net magnet moments is zero. In ferromagnetic metal, however, one band of spin is majority and the other one is minority, which results in a non.zero magnetic moment. Therefore, the material shows magnetic property. Generally, spin polarization is defined as the percentage difference of the density of states (DOS) of spin-up and spin-down electrons around the Fermi level:

$$P = \frac{N_{\uparrow}(E_F) - N_{\downarrow}(E_F)}{N_{\uparrow}(E_F) + N_{\downarrow}(E_F)} \times 100\% \tag{4.1}$$

where the arrows indicate the direction of spin, and E_F is the Fermi level. For non-magnetic metals, the net magnetic moment is zero, meaning that spin up and spin down electrons are equal. Therefore, the spin polarization is zero. One extreme is half metal. In half metal, there is only one spin band at the Fermi level, whether spin-up or spin-down, are available. Thus, the spin polarization is 1. For all the ferromagnetic materials, one spin band dominates, while there still exists a minority spin band, so that the spin polarization is between 0 and 1.

The definition of spin polarization in equation(4.1) is just for ideal case or in a perfect bulk crystal. However, experimentally, the spin polarization is often measured with the point contact method, in which the interface between the well known material

and the 'to be measured' material may have effect on the P value. Generally, the size of the contact interface will have effect on the P value. For example, if the interface size is smaller than the electron mean free path, one will get the so called ballistic spin polarization, which can be calculated as:

$$P_{ballistic} = \frac{N_{\uparrow}(E_F)v_{\uparrow F} - N_{\downarrow}(E_F)v_{\downarrow F}}{N_{\uparrow}(E_F)v_{\uparrow F} - N_{\downarrow}(E_F)v_{\downarrow F}} \times 100\% \tag{4.2}$$

where $v_{\uparrow F}$ and $v_{\downarrow F}$ are the Fermi velocity for the spin up electrons and spin down electrons, respectively. On the other hand, when the interface size is large than the electron mean free path, the electrons will suffer from scattering from the crystal lattice and the spin polarization can be expressed as [33]:

$$P_{ballistic} = \frac{N_{\uparrow}(E_F)v_{\uparrow F}^2 - N_{\downarrow}(E_F)v_{\downarrow F}^2}{N_{\uparrow}(E_F)v_{\uparrow F}^2 - N_{\downarrow}(E_F)v_{\downarrow F}^2} \times 100\% \tag{4.3}$$

When there exists a thin layer of insulator at the interface between the well know material and the unknown material, the electrons will tunnel into the unknown material through the tunneling effect. Thus, the spin polarization may be different, due to the tunneling matrix [34]:

$$P_{ballistic} = \frac{N_{\uparrow}(E_F)|M_{\uparrow}|^2 - N_{\downarrow}(E_F)|M_{\downarrow}|^2}{N_{\uparrow}(E_F)|M_{\uparrow}|^2 - N_{\downarrow}(E_F)|M_{\downarrow}|^2} \times 100\% \tag{4.4}$$

where $M_{\uparrow}$ and $M_{\downarrow}$ are the tunneling matrices.

The performance of spintronics devices, such as GMR structures, MTJ structures etc, relies heavily on the spin polarization of the ferromagnetic layer [35–43]. For example, the TMR ratio can be calculated by [10]:

$$TMR(\%) = \frac{P_1 P_2}{1 - P_1 P_2} \tag{4.5}$$

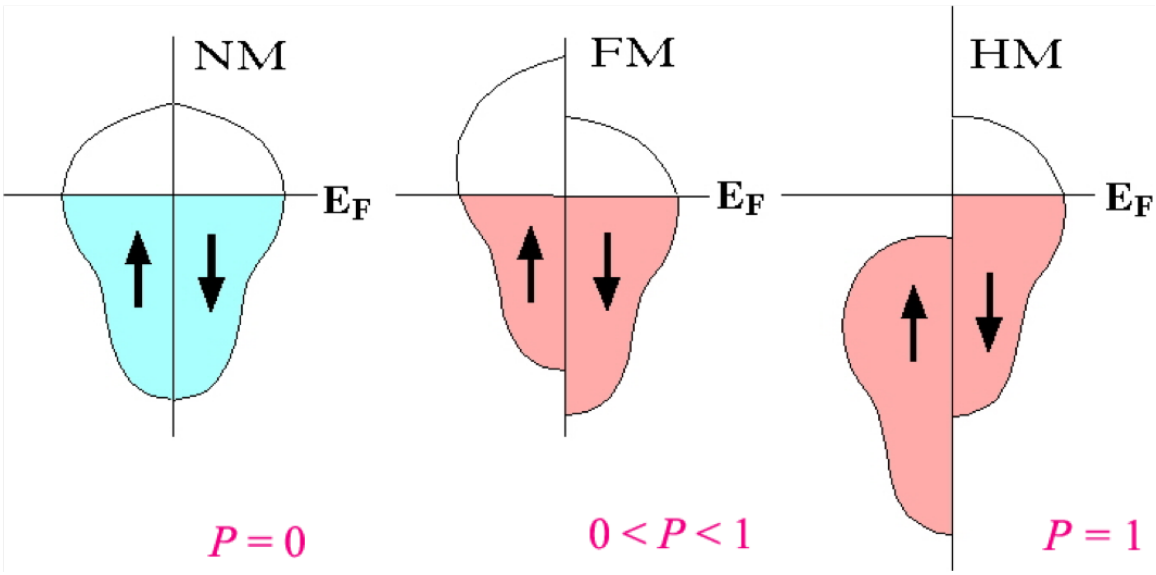

Figure 4.1: Left: For non-magnetic material, the spin polarization is zero. Middle: For ferromagnet, the spin polarization is between 0 and 1. Right: For half metal, the spin polarization is 1.

where P_1 and P_2 are the spin polarization for the two ferromagnetic layer. From the equation, one can see that when both materials reach perfect spin polarization ($P = 1$), the TMR ratio can reach infinite. Therefore, it is crucial to find a material, especially metal, with a spin polarization as high as possible. So far, the only material that has half-metallic properties is the CrO_2, which has a spin polarization about 98.6%, measured with Andreev Reflection Spectroscopy (ARS)[44].

4.2 Andreev Reflection

The Andreev Reflection (AR) will happen at the interface between a normal metal and a superconductor, as is shown in figure(4.2)[45]. The figure shows the energy vs. momentum relationships. In the normal metal side, $E_k = \frac{q^2}{2m}$, while in the superconductor side, the energy will follow the band structure as described in the BCS model. When an electrical current passes through the interface, part of the electrons will enter the band gap and form supercurrent. For example, the electron 0 in the figure will incident into the superconductor. It has a positive momentum and the spin is up (the label is $+q^+$). When 0 enters the superconductor, the momentum becomes +k. Another electron inside the metal, with opposite momentum, -k, and opposite spin, will form Cooper pair with it, as indicates by the electrons 2 and 4. As a result, a hole, with positive charge, negative momentum -q and down spin will be reflected in to the normal metal side.

To achieve the Andreev Reflection, liquid Helium is used to provide low temperature. 4-point-contact method is used to measure the differential conductance of the superconductor, as is shown in figure(4.3).

As is shown in the figure, 2 leads are on the tip and the other 2 on the sample. The leads I+ and I- are used to send current into the sample, while V+ and V- are used to measure the voltage across the two points. The size of the tip varies, making the

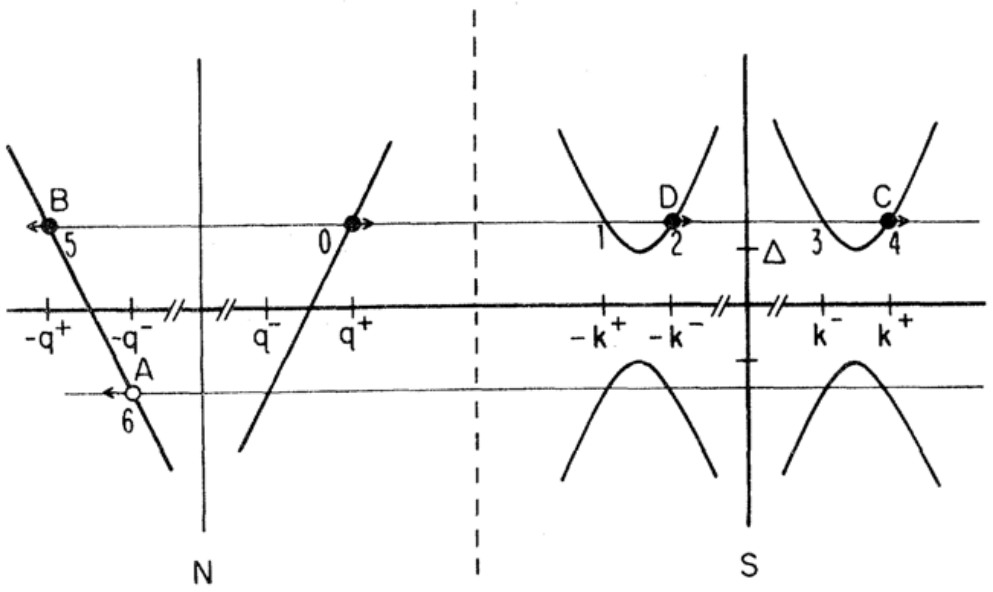

Figure 4.2: Andreev Reflection happens at the interface between a normal metal and superconductor. Solid dot: Electrons; Open circle: reflected hole. q and k: momentum.[45]

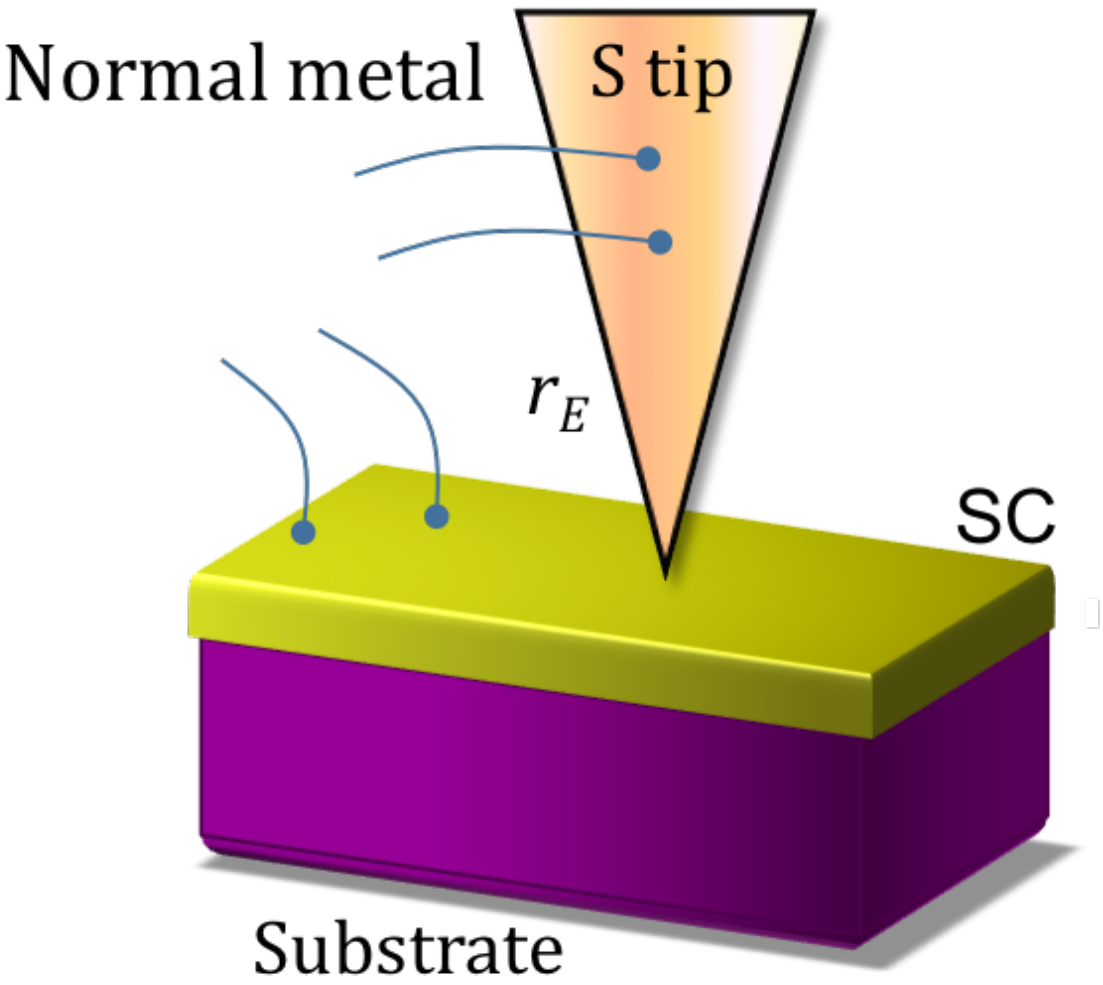

Figure 4.3: For point contact Andreev Reflection spectroscopy, a non-superconductor normal is made into a sharp tip, in order that the incident electron will be in ballistic regime. Two electrodes are on the tip and two electrodes are connected to the sample. Andreev Reflection will happen at the point contact.

electron transport into different regimes. When the point contact diameter a is about 1 to 2 $\mathring{A}$, it is called quantum regime. In this regime, the conductance quantization is clearly observed[46]. If the contact size is larger than the de Broglie wavelength but much smaller than the elastic scattering mean free path, the contact is said to be in the ballistic regime. In this regime, the electrons will rarely be scattered, which is a preferred condition for AR experiment. If the diameter a is larger than the scattering mean free path, the electrons will suffer from scattering when injected into the superconductor. This is called the thermal regime and the Joule heating will raise the local temperature of the point contact, which will make the experiment not stable.

The results of AR experiments can be explained by the BTK model, which was proposed by G. E. Blonder, M. Tinkham and T. M. Klapwijk in 1981[45]. The model starts by assuming that there is no applied voltage at the Normal metal (N) and superconductor (S) interface. In this case, the system is at equilibrium state and all the quasiparticles (0, 1, 2, 3, 4, 5 in figure(4.2)) are occupied with the same probability $f_0(E)$. And for the hole will be $f_0(-E)$. When an electron incident on the interface from the N side with $E > 0$, the probability that it transmits through the interface with the wave vector in the same side of the Fermi surface is C(E) (from 0 to 4); the probability for the transmission with wave vector in the opposite Fermi surface is D(E) (from 0 to 2); the probability for the normal reflection is A(E) (from 0 to 5); the probability for the Andreev reflection is B(E) (from 0 to 6). The conservation of probability requires:

$$A(E) + B(E) + C(E) + D(E) = 1 \tag{4.6}$$

In general, the value of these probabilities depend on the incident angle of the electron. For simplicity, just consider the one-dimension model. The interface of

the NS can be considered as a repulsive potential $H\delta(x)$, which is typical for oxide barrier in a high-current-tunnel junction. Calculate these four probabilities with the Bogoliubov equations, the results are shown in the figure(4.4)[45]:

where $Z = \frac{k_F H}{2\epsilon_F} = \frac{H}{\hbar v_F}$ is the barrier strength, Δ is the superconductor band gap, E is the energy of the incident electron, $\gamma^2 = [\mu_0^2 + Z^2(\mu_0^2 - v_0^2)]^2$, $N_s(E) = \frac{1}{\mu_0^2 - v_0^2}$ and $\mu_0^2 = 1 - v_0^2 = \frac{1}{2}[1 + \sqrt{\frac{E^2 - \Delta^2}{E^2}}]$.

The results are very obvious under some circumstances. As can be seen, when $Z = 0, A = 1\ for E < 0$. This means if there is no barrier potential in the interface, and the energy of the incident electron is lower than the band gap, the electrons in the normal metals will just form Cooper pairs and enter the superconductor gap with a probability 1, resulting in a hole reflected back into the normal metal due to charge conservation. This is why the resistance of the superconductor is zero and the conductance is doubled when the incident current is very small. When the current increases, some electrons will couple into Cooper pairs and enter the superconducting gap, while others with higher energy will do tunneling into the superconductor side. Those Cooper pairs will generate supercurrent, while those electrons not within the band gap will behave like normal electrons. In this case, the conductance of the superconductor will gradually decrease. When the current is larger than the critical current, all electrons will enter the SC without forming Cooper pairs, being scattered by the lattice. Thus, the superconductivity disappears (As is shown in figure(4.5) A). So from the curves we get from ARS, we can know a lot of properties of superconductors, such as superconducting gap, critical current etc.

	A	B	C	D
Normal state	0	$\frac{Z^2}{1+Z^2}$	$\frac{1}{1+Z^2}$	0
General form				
$E<\Delta$	$\frac{\Delta^2}{E^2+(\Delta^2-E^2)(1+2Z^2)^2}$	$1-A$	0	0
$E>\Delta$	$\frac{u_0^2v_0^2}{\gamma^2}$	$\frac{(u_0^2-v_0^2)^2Z^2(1+Z^2)}{\gamma^2}$	$\frac{u_0^2(u_0^2-v_0^2)(1+Z^2)}{\gamma^2}$	$\frac{v_0^2(u_0^2-v_0^2)Z^2}{\gamma^2}$
No barrier ($Z=0$)				
$E<\Delta$	1	0	0	0
$E>\Delta$	v_0^2/u_0^2	0	$1-A$	0
Strong barrier [$Z^2(u^2-v^2)>>1$]				
$E<\Delta$	$\frac{\Delta^2}{4Z^2(\Delta^2-E^2)}$	$1-A$	0	0
$E>\Delta$	$\frac{u_0^2v_0^2}{Z^4(u_0^2-v_0^2)^2}$	$1-\frac{1}{Z^2(u_0^2-v_0^2)}$	$\frac{u_0^2}{Z^2(u_0^2-v_0^2)}$	$\frac{v_0^2}{Z^2(u_0^2-v_0^2)}$

Figure 4.4: The calculation results for the 4 probabilities in the BTK model under different barrier conditions.[45]

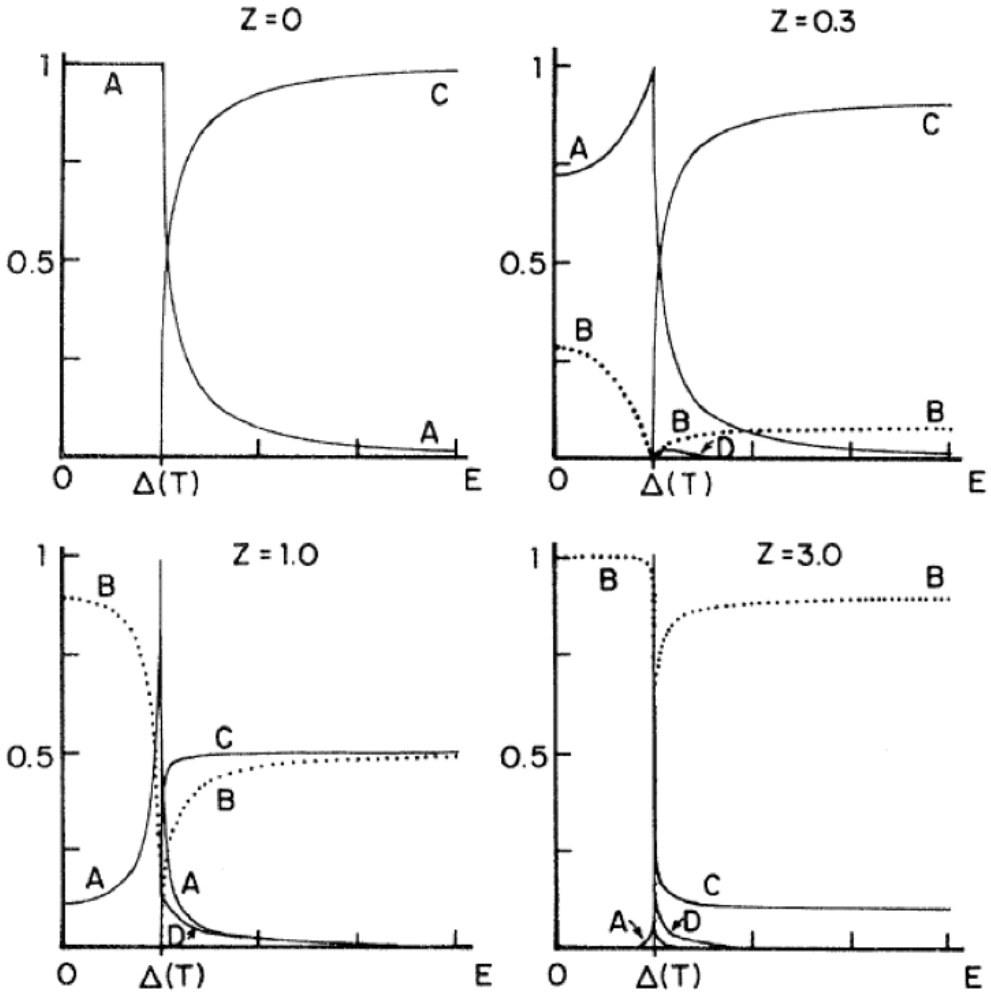

Figure 4.5: Differential conductance vs. energy in different barrier conditions.[45]

Chapter 5

EXPERIMENTAL METHODS

5.1 Magnetron Sputtering

Some materials, such as Fe, Co and Ni, can show magnetic property. When fabricated in nano scale, the magnetic behavior under external magnetic field could become more interesting due to the broken of inversion symmetry and the interaction between the material with the surrounding environment. The prerequisite is to make nano materials with good quality. Currently, there are several fabrication methods, such as magneton sputtering, atomic layer deposition (ALD), chemical vapor deposition (CVD), physical vapor deposition (PVD), sol-gel method, molecular beam epitaxy (MBE), Metal Organic Chemical Vapor Deposition (MOCVD) etc. Generally, magnetron sputtering offers a relative fast deposition rate, and good thin film quality. Therefore, this dissertation work will focus on using magnetron sputtering method.

Figure(5.1)[47] is a sketch of magneton sputtering. All the sputtering processes are done in a vacuum chamber with a base pressure about 2×10^{-8} torr. The target is fixed on a power supply, on which there are several magnets. The surface of the substrate will face the target. When the deposition begins, some Argon (Ar) gas will be sent into the chamber, which make the pressure increase to about 3×10^{-3} torr. The power supply will ionize the Ar atom into Ar ion (Ar^+). Due to the electric force, the Ar^+ will be accelerated to bombard on the target. As a result of the momentum and energy exchange, the target atoms will come out and deposit on the substrate. Those Ar^+ will combine with electrons on the target and become Ar atom

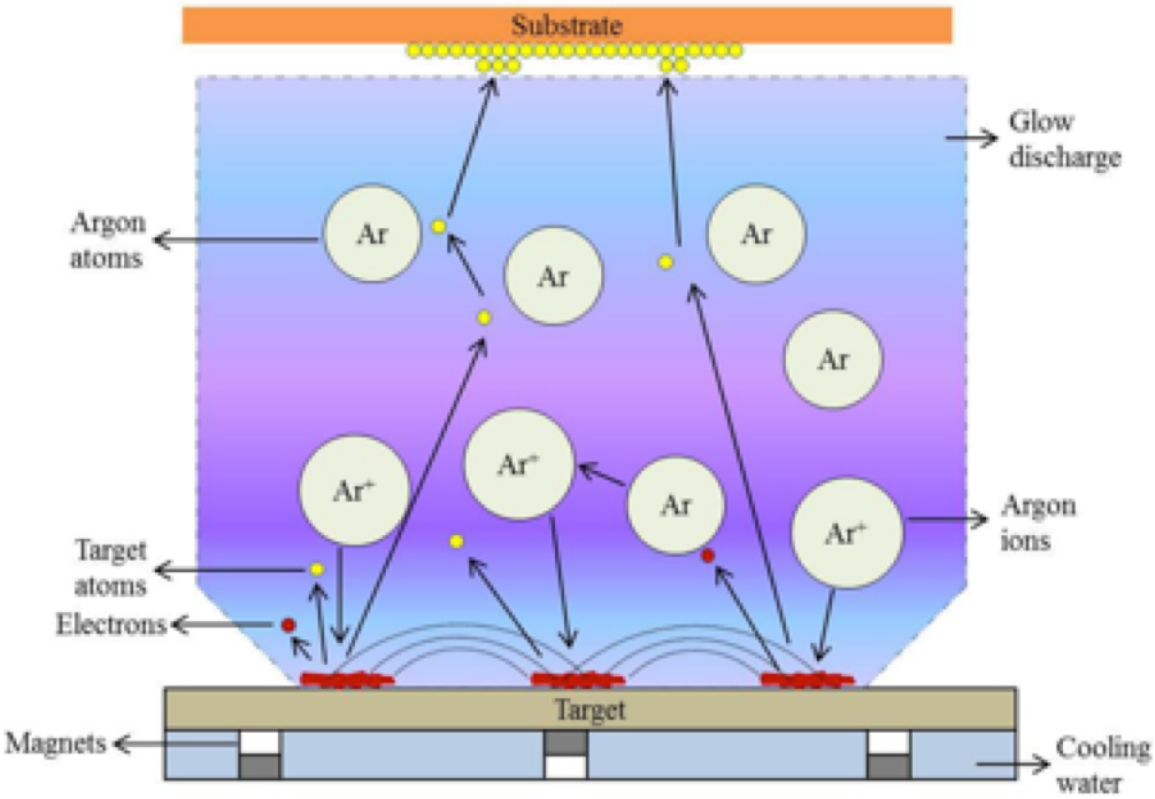

Figure 5.1: Ar atoms will be ionized by the strong electrical field and bombard on the target, thus transfer its momentum to the target atom. The atom will come out of the target and deposit on the substrate. The magnets are used to confine the ions in a certain regime so that the deposition process is effective.[47]

again. With the process going on, Ar atoms, Ar^+, electrons and target atoms will form a special state on top of the target, which is called 'plasma'. The function of the magnet under the target is to confine the plasma in a certain area so that the deposition process can continue. This is the basic working mechanism of magneton sputtering, especially when the target is made of metal.

However, in some cases, insulator target has to be used, such as Magnesium Oxide (MgO), Yttrium Iron Garnet (YIG) etc. In those materials, electrons can not move freely because of the large bandgap of insulators. Therefore, during the deposition process, Ar^+ will keep accumulating on the target. As more and more Ar^+ stay on the target, the electrical potential on the target increases, which will prevent other Ar^+ from bombarding on the target. Therefore, the deposition will gradually stop. The way to avoid this is to apply a Radio frequency (RF) signal[48], instead of DC signal, on the target, as is shown in figure(5.2).

The initial deposition is just like the dc sputtering process: a high negative voltage is applied at the target, which will generate the plasma on top of it to achieve material deposition. After some very short time interval, the signal is switched, meaning the voltage on the target is higher than that on the substrate. In this case, the Ar^+ accumulated on the target will be neutralized by electrons. Thus, when the signal is switched again, the electric potential on the target can be reset as the initial condition, ensuring the continuous deposition process.

Figure(5.3) shows the sputtering system used in this work. A total ten sputtering guns are installed in the main chamber. The substrate holder and shutter (not shown in the figure) are controlled by the motion controller, which is connected to the GPIB interface for remote control. Labview program is used to control the rotation of the holder than shutter, in order to get the desired layer thickness and combination. The cryo pump is used to pump the main chamber all the idle time, to maintain a good

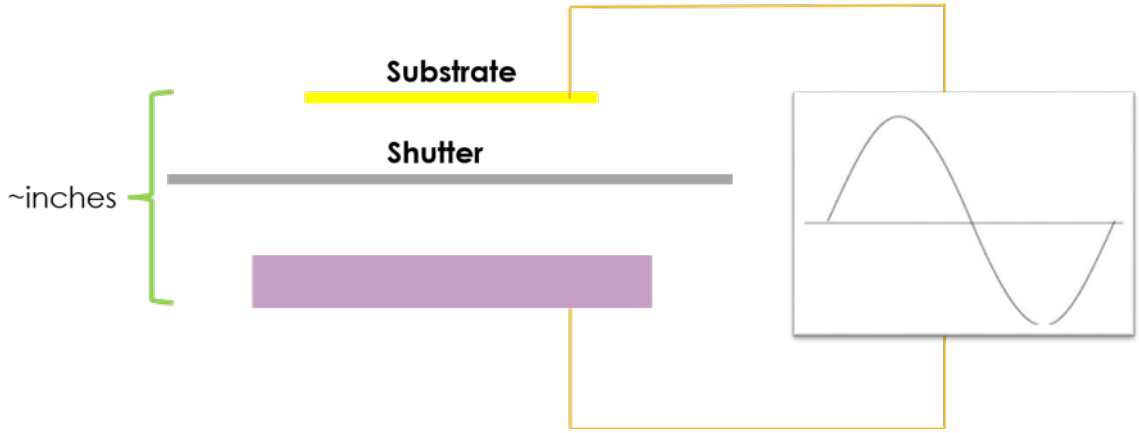

Figure 5.2: When the target is insulator, the magnetron sputtering is different. A RF power supply has to be used to replace the dc power supply, in order to neutralize the Ar^+ accumulated on the target.

vacuum inside the chamber. The vacuum in monitored by the ion gauge mounted on top of the 19-inch rack. The base pressure of the main chamber is around $2\times10^{-8}torr$, which is good enough for most sputtering materials. A gate valve is used to separate the main chamber and the loadlock. The use of loadlock is to prevent the main chamber from contacting the outside environment directly in order to reduce the contamination from the ambient and ensure good thin film quality. A turbo pump is used to pump the loadlock to load and unload the sample. 5 sputtering gun selection gears are installed on the rack, making it possible to switch the guns freely. 4 DC power supplies and 1 RF power supply are also mounted on the rack. Therefore, the sample can contain as many as 5 different layers without stopping the deposition process. A gas controller is used to control the sputtering gas: Ar, O_2 and N_2. Usually, Ar is used for pure metal deposition, with a gas flow of 20 mccm and a deposition pressure of 6 mtorr. When oxide or nitride is needed, Oxygen or nitrogen will be sent into the chamber, together with the Ar gas. A water chiller is also installed (not shown in the figure) in order to cool down the guns during the deposition and protect the magnets in the guns.

5.2 Rutherford Backscattering

After get a nano thin film, the next step is to calibrate the thickness of it. The thickness of the films are very important since different thickness will produce different magnetic properties. For example, very thin Cobalt (Co) and Platinum (Pt) bilayers will show perpendicular magnetic anisotropy. While if the Cobalt layer is too thick, this property will disappear due to the stronger in plane magnetic anisotropy of the Co film. To calibrate the thickness, Rutherford Back Scattering (RBS) is used[49].

RBS was discovered by Lord Ernest Rutherford between 1909 and 1914 with studying the scattering of alpha particles through metal foils. The results of the

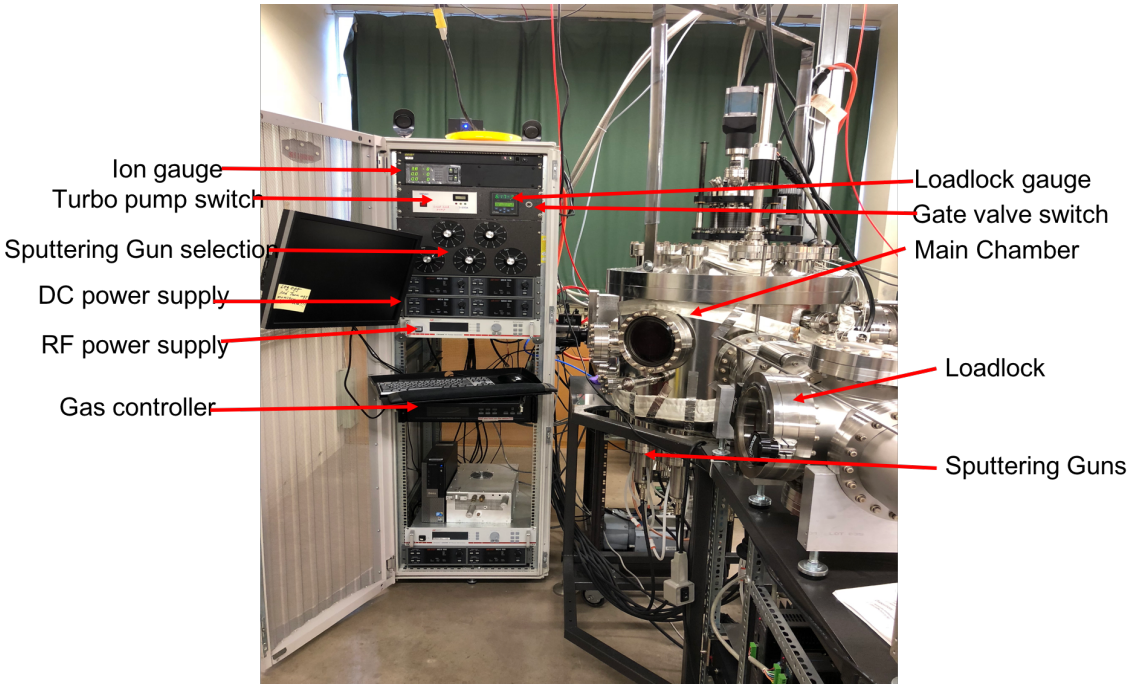

Figure 5.3: Sputtering system used in this work.

experiments led to the development of Rutherford model of the atom structure. Figure(5.4) shows the general process of the backscattering.

When a beam high energy ions bombard on a piece of sample, a small portion of those ions will undergo a direct collision with a nucleus of the atoms in the sample. As long as the energy of the ions is not too high, certain nuclear reaction will not happen and the collision can be regarded as elastic collision. The collision does not involve direct contact between the ions and the nucleus. The energy loss in this process is due to the Coulomb force. Therefore, ions at different positions will be backscattered into different angle. There are several factors that will affect it.

The first factor is kinematics. It is defined by the ratio of the projectile energy after a collision to the projectile energy before a collision[49]. For scattering at the sample surface, energy will lose only due to the momentum and energy transfer between the ions and the sample atoms. If the sample atoms are light, for example, Carbon, Oxygen, Nitrogen etc, a significant fraction of the incident ions' energy will be transferred to those atoms, while for heavy atoms, such as Iron, Nickel etc, the ions will bounce back with almost the same energy and momentum. Therefore, the backscattering technique is more useful to detect light elements.

The second factor is the differential scattering cross section. This is related to the relative number of particles backscattered from sample atoms into a given solid angle for a given number of incident particle. When the ions incident to the atoms, the Coulomb force between the ions and the nucleus will make the ions deviate from its original paths. The differential cross section of the backscattering will be[49]:

$$\frac{d\omega}{d\Omega} = (\frac{Z_1 Z_2 e^2}{4E_0})^2 \frac{1}{(sin\theta/2)^4} \tag{5.1}$$

Where Z_1 and Z_2 are the atomic numbers of the incident ion and target nuclei, E_0 is the initial kinetic energy of the ion, θ is the scattering angle between the wave vector

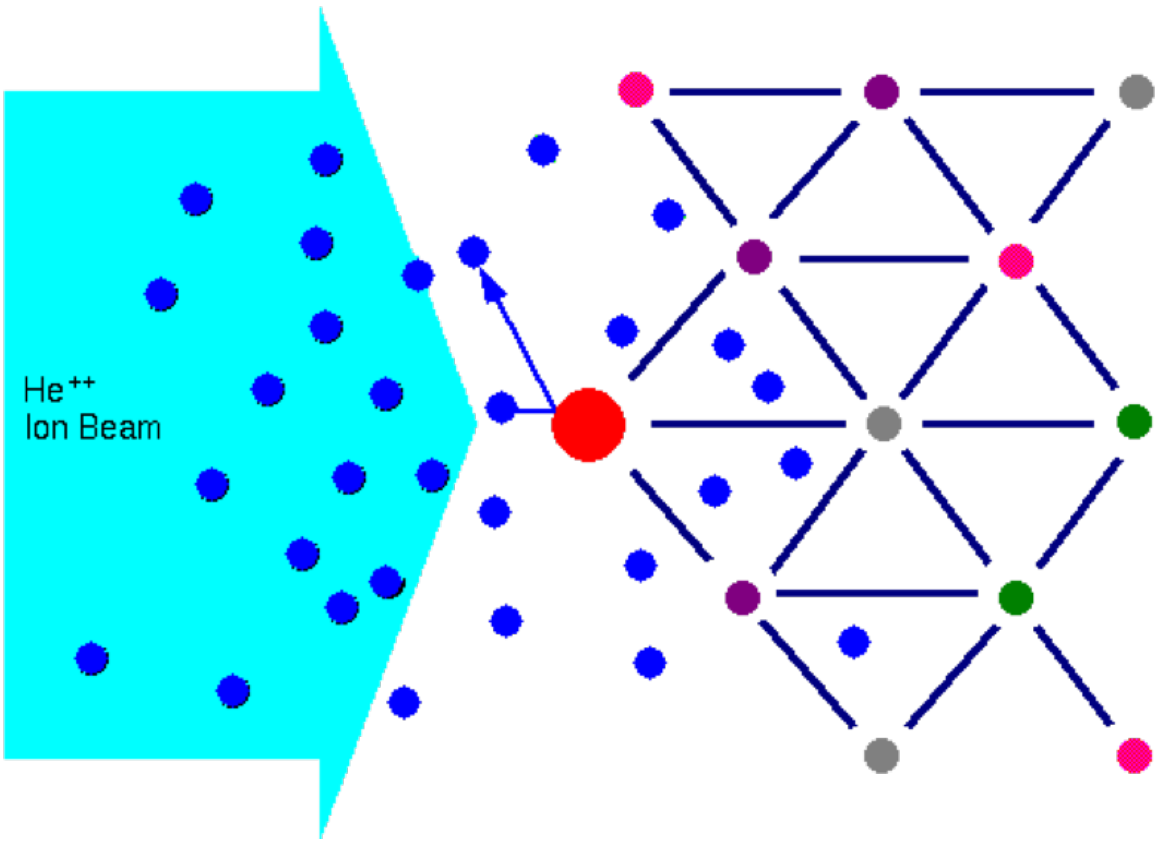

Figure 5.4: In the process of Rutherford backscattering, the He atoms are first ionized to be He^{2+}, which will be accelerated to strike on the sample. When the He ions are approaching the atoms on the sample, the Coulomb force will be stronger so that the ions will be scattered. Since the nucleus are quite small, only a small part of ions will be scattered and the other ions will penetrate through the surface and be scattered by the atoms in deeper layers or even substrate.

before and after collision. As we can see from the equation, for a given scattering angle, the differential cross section will be larger when the target atoms are heavier. As is shown in figure(5.5), the relative generate rate for heavier elements, such as Au, Nb, is larger than that of lighter elements. This is due to the larger cross section in the backscattering process.

The third factor is the stopping power. As is mentioned above, only a small portion of incident ions will undergo backscattering due to the small size of nucleus. A vast majority portion of ions will undergo glancing collisions with the sample atoms, and interact with the electrons in the sample. With the ions going deeper into to the sample, more energy will be lost. Therefore, the backscattering energy for ions scattered from deeper position will be smaller than that from the surface of the energy. By doing calculations about this difference, the thickness of the sample can be calculated.

Those factors listed above provide us a good method to calibrate the sample. By doing careful calculations and fitting of the experimental data, the thickness of the sample, the elemental ratios and the elemental concentrations will be known.

5.3 Vibrating Sample Magnetometer

For magnetic materials, one of the most important measurements is to measure the magnetization. Generally, all the methods can be classified into three categories[22]: (1). Measurement of the force acting on a magnetized body in a non-uniform field; (2). Measurement of the magnetic field produced by a magnetized body; (3). Measurement of the voltage produced in a search coil by electromagnetic induction caused by a change in the position of state of magnetization of a magnetized body.

Vibrating Sample Magnetometer (VSM) falls into the second category. When use VSM, the sample S will oscillate vertically in a uniform magnetic field. The

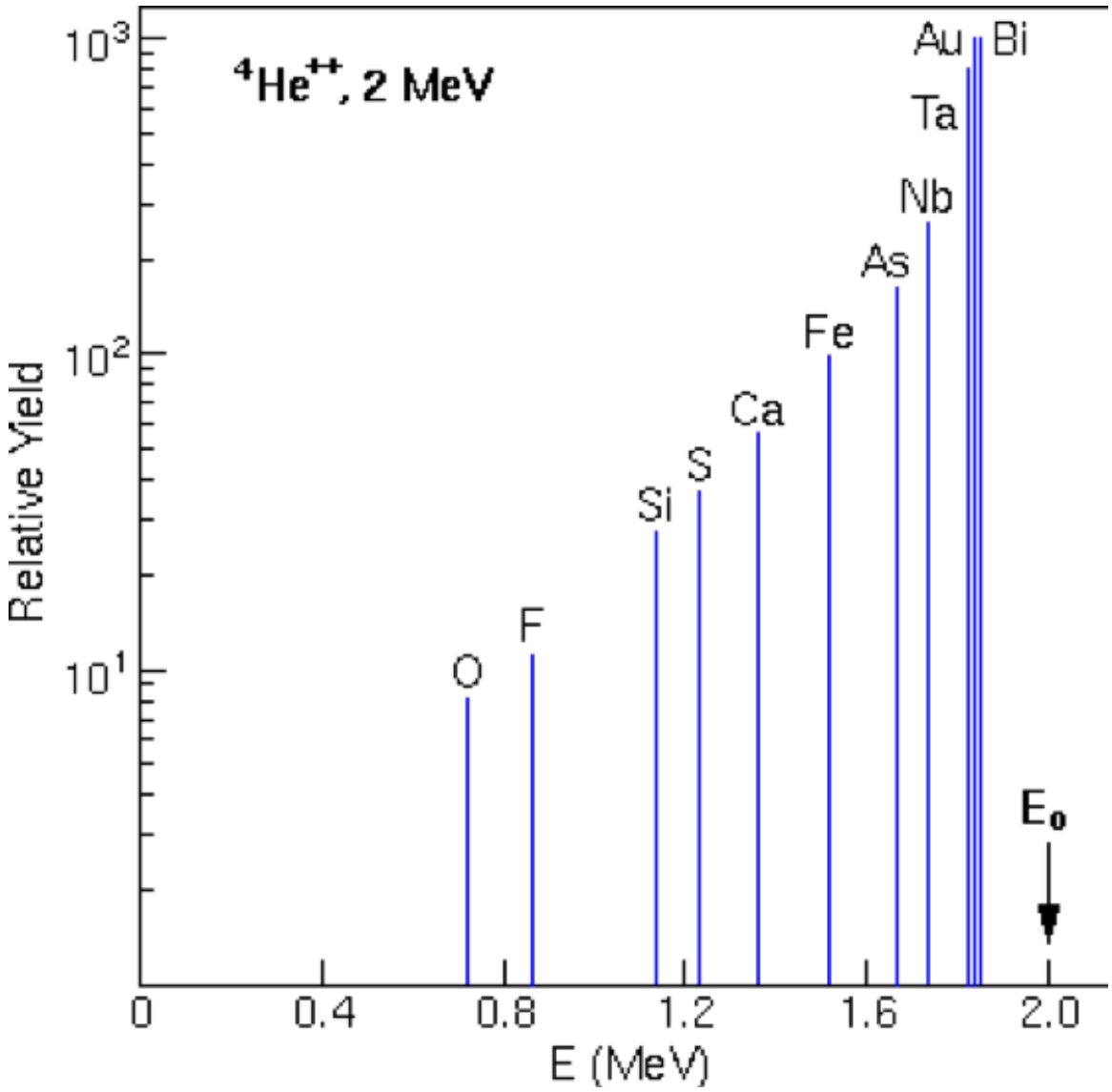

Figure 5.5: RBS is more accurate for heavier atoms. Due to the momentum and energy transfer during the scatter process, heavier atoms will results in larger differential cross section, thus more ions will be scattered.

magnetization of the sample will generate a magnetic field around it. The vibration of the sample will result in a change in magnetic flux in the pick-up coil so that a voltage will be induced due to the Faraday's Law of induction.

As is shown in the figure(5.6), the sample will be placed in the middle of the electromagnet gap, which will make it in a uniform magnetic field environment. There are two signal pickup coils attached to the surface of the magnet. The sample rod is connected to an oscillator, which will make it undergo sinusoid motion in the vertical direction. According to the Faraday's law, the movement of the magnetic material will change the magnetic flux in the pickup coils, thus induces an electrical signal:

$$V = -\frac{\partial \Phi}{\partial t} \tag{5.2}$$

where Φ is the magnetic flux, V is the induced electrical voltage. If the pickup coil has a cross section A and windings n, then the equation can be written as;

$$V = -nA\frac{\partial B}{\partial t} \tag{5.3}$$

When the sample is in a uniform external magnetic field $\mathbf{H}$, it will be magnetized and the magnetization will reach $\mathbf{M}$. Therefore, the magnetic flux density around the sample can be calculated by:

$$\mathbf{B} = \mu_0(\mathbf{H} + \mathbf{M}) \tag{5.4}$$

As is mentioned above, the external field $\mathbf{H}$ is produced by the electromagnetic and can be treated as uniform and constant, then the induced voltage can be written as:

$$V = -\mu_0 nA\frac{\partial M}{\partial t} \tag{5.5}$$

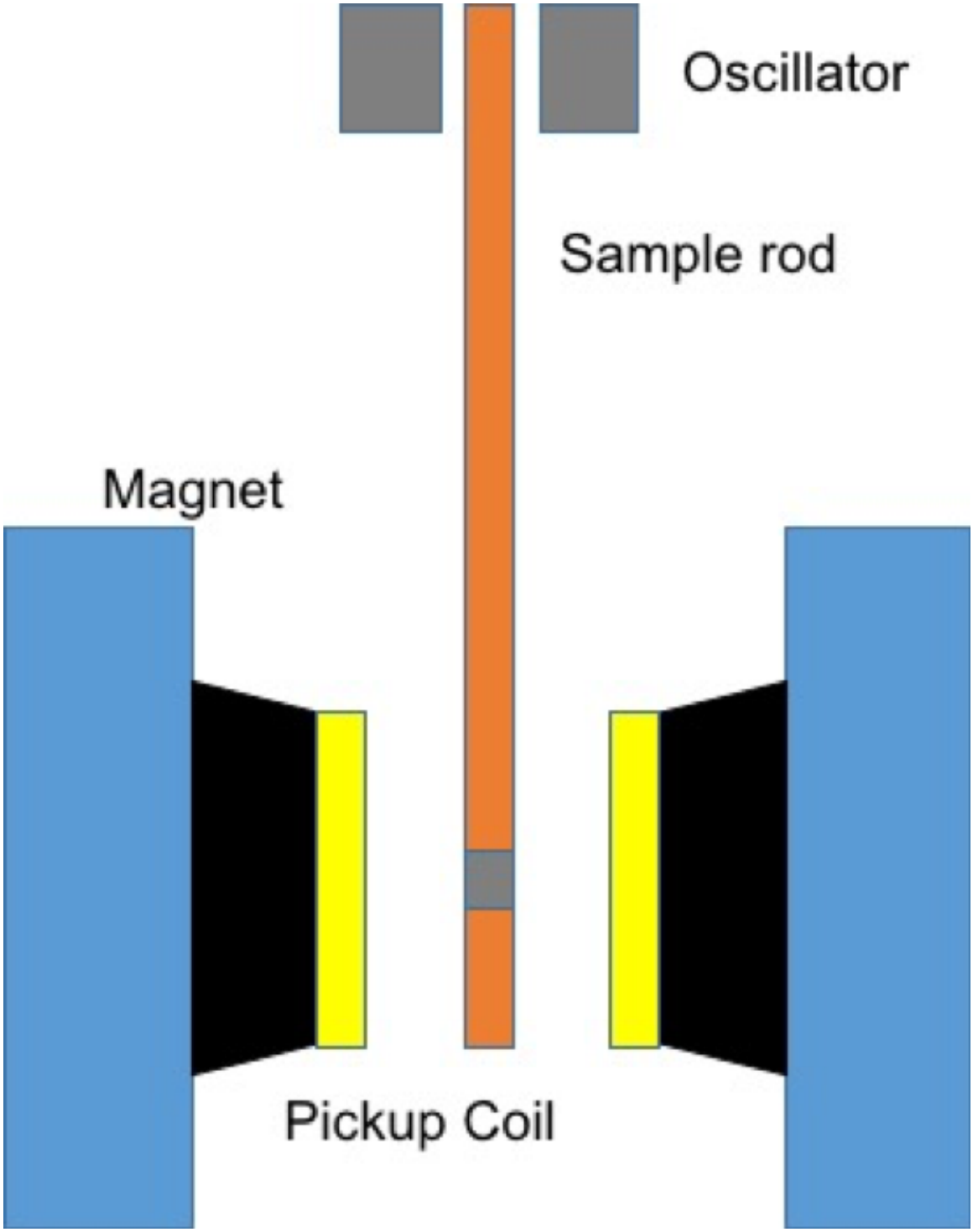

Figure 5.6: In VSM, the sample is vibrating sinusoidally around the center of the two pick-up coil. The magnetization will generate a magnetic field, which will induce a change in magnetic flux in the coil. A voltage is induced due to the Faraday's law of induction and the magnetization of the sample can be calculated based on the induced voltage.

Therefore, the induced signal, which is at the frequency of vibration, is proportional to the magnetization, vibration amplitude and frequency. After the signal is collected by the pickup coils, it will be buffered, amplified and applied to a special demodulator. Then it will be synchronously demodulated with respect to the reference signal derived from a moving capacitor assembly. The resulting signal will only have relation with the magnetic moment magnitude alone.

The VSM in our lab is Lakeshore 7304. It can measure the magnetization from $5 \times 10^{-6} emu$ to $10^{3} emu$. The noise level is about $55 \times 10^{-6} emu$. On the other hand, the maximum magnetic field provided by the electromagnet is $\pm 14.5 kG$, which is good enough magnetize many magnetic materials that has beed used in the lab to saturation magnetization.

5.4 Magnetic Transport System

Besides the measurement of magnetization with VSM, the electron transport properties of the sample is also a key factor for better understanding the material. When electrons are moving inside a material, the scattering from the atoms will result in resistance. The resistivity will be affected by many factors, including temperature, film thickness, crystal quality, magnetization etc. The famous giant magnetoresistance (GMR) effect is the change of resistance in an external field, which has been described in Chapter 1.

Four-Point Measurement

When measure the resistance, the current is sent into the sample and voltage is measured. So the resistance can be calculated by $R = V/I$. However, this measurement contains many different resistance, including the resistance from the wires, the contact, and the sample, as is shown in figure(5.7(a)). When measure a thin film sample,

the contact resistance can be large, due to the contact size and quality. Therefore, the measured resistance may be quite different from the real value.

To solve the problem, a four-point measurement technique is used. In this measurement configuration (figure(5.7(b))), the current is sent into the sample through the outside two electrodes and voltage is measured through the inside two electrode. In this case, the current that goes through the sample is the same as the current goes through the wire. So the reading number from the ammeter is the true current that is sent into the sample. The voltage is measured in the inner circuit. Generally, the resistance of the voltmeter is much larger compared with the resistance from the wires. Therefore, in the inner circuit, the current that goes through the wires can be negligible. The reading from the voltmeter is almost the true voltage on the sample. In this way, the resistance of the sample can be measured accurately.

Figure(5.7(c)) illustrates the 4-point measurement setup in the lab. The sample is mounted in the center of a rotatable electromagnet to get a uniform field in different directions. The four electrodes are attached to the sample as described above. In this way, the magnetoresistance of the sample in different field directions can be measured accurately.

Anomalous Hall Effect Measurement

Hall effect is discovered by Edwin Hall in 1879[28]. When a current is send into a sample and a magnetic field is applied in the out of plane direction, a voltage can be measured in the transverse direction. In non magnetic materials, the electrons will suffer from the Lorentz force from the external field. Therefore, the path of the electrons will be deflected so that they will accumulate at the edges of the sample, thus generated a electrical field. The measured voltage can be expressed as:

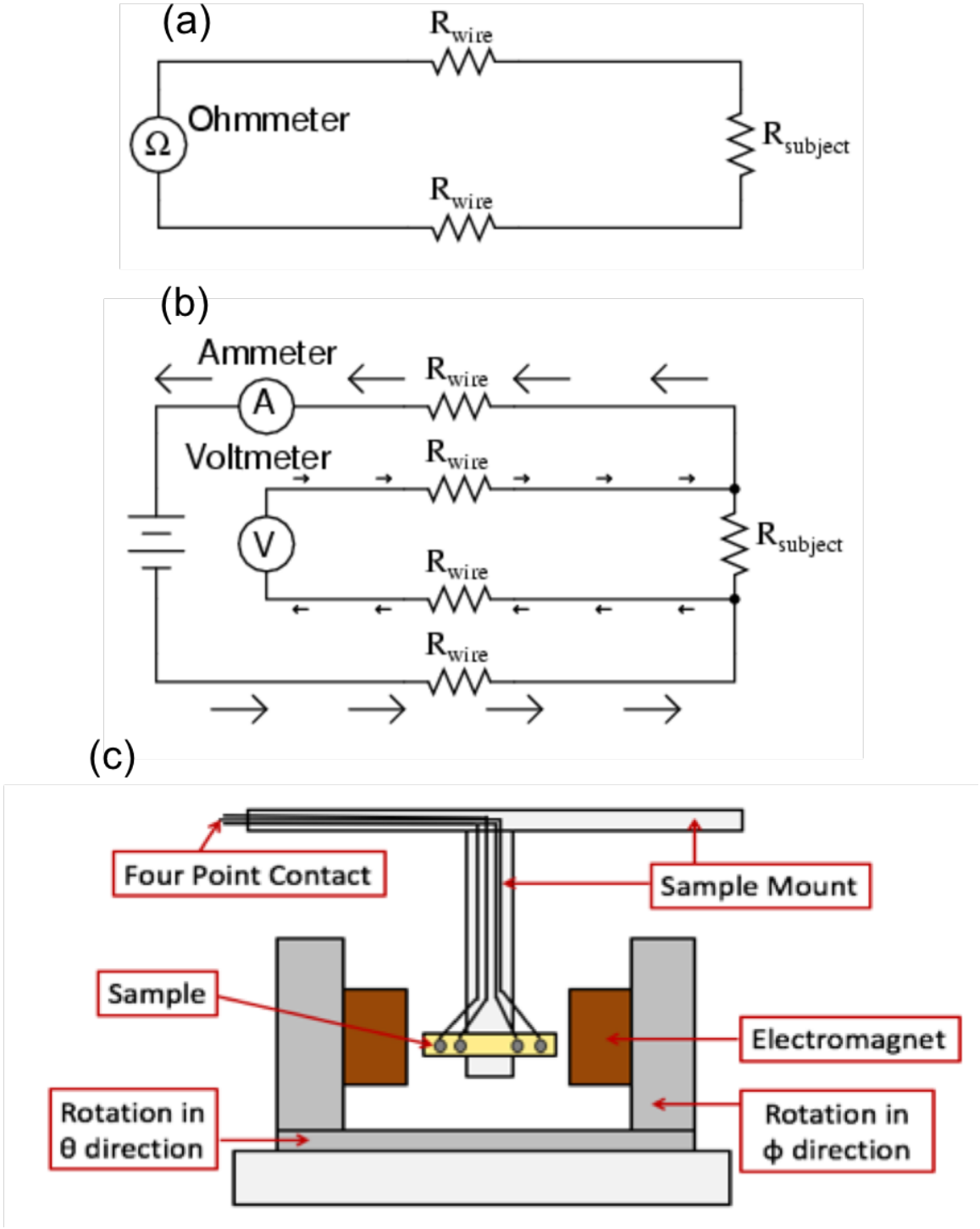

Figure 5.7: (a)Illustration of 2-point measurement. The results contains many components such as wire resistance, contact resistance and sample resistance. (b). Illustration of 4-point measurement. The result reflect the real resistance of the sample. (c) Illustration of the 4-point measurement setup used in this dissertation work.

$$V_{Hall} = \frac{I_x H_z}{nte} \tag{5.6}$$

where I_x means the current is sent in through x direction, H_z means the magnetic field is applied in the z direction, t is the thickness of the sample, n is the electron number density and e is the electron charge. The measurement configuration is the same as in figure(5.7). The only difference is that the two inner voltage electrodes will be aligned vertical to the two outside current electrodes. The voltage will linearly change with the external field, as is shown in figure(5.8(b)).

In anomalous Hall effect (AHE), however, the electrons will not only be deflected by the applied field, but also by the magnetization. Usually, the magnetization will have much larger effect on the deflection. Thus, AHE is a useful way to study the magnetic property of the materials. Generally, the AHE signal contains several parts:

$$V_{AHE} = \frac{I_x H_z}{nte} cos\alpha + \frac{\mu_0 R_s I_x}{t} M cos\theta + \frac{k I_x}{t} M^2 sin^2\theta sin2\phi \tag{5.7}$$

where μ_0 is the vacuum permeability, R_s is the Hall coefficient, M is the magnetization, k is a constant, θ is the angle between magnetization and the out of plane direction, α is the direction of the field from the out of plane direction, and ϕ is the direction of the projection of M in the x-y plane. One can see that the first term is the normal Hall effect, and the other two terms has relation with the magnetization and its direction. By analyzing the measured signal, the magnetic property can be well understood.

5.5 Andreev Reflection Spectroscopy

Andreev Reflection is a powerful way to study superconductivity, as well as the spin polarization in magnetic materials[35, 50–54]. The equipment to measure An-

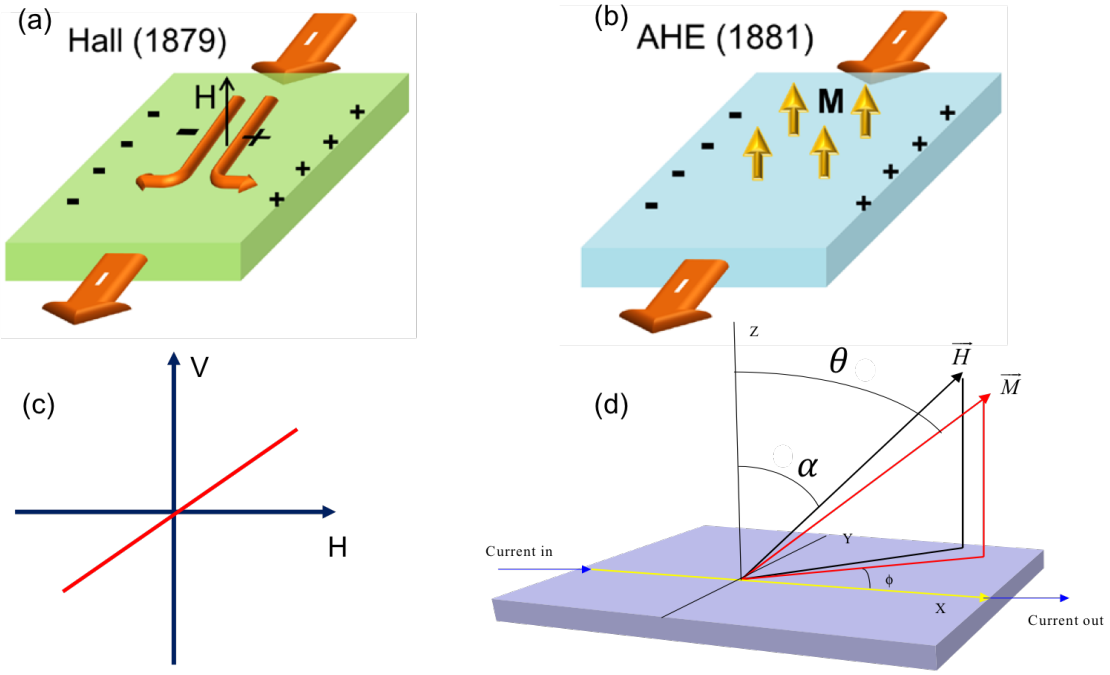

Figure 5.8: (a)Illustration of normal Hall effect. (b). Illustration of Anomalous Hall effect. (c). In normal Hall effect, the Hall voltage linearly changes with the applied field. (d). In anomalous Hall effect, the results has relation with not only field, but also the magnetization.

dreev Reflection is called Andreev Reflection Spectroscopy (ARS).

5.5.1 ARS Mechanical Setup

Tip Preparation

Andreev Reflection is quite sensitive to the interface between the normal metal and the superconductor. Generally, the normal metal should be made into a sharp tip so that the electrons are in the ballistic regime, as is discussed in Chapter 4. In this work, there are two methods to prepare a proper tip: one is to polish the tip mechanically. For some tips, such as Nb rod, and Au plate, the material is quite hard. In order to make a sharp tip, a polishing stone of coarse grade around 1000 is used. Usually, the polished tip is approximately $10 \sim 30\mu m$, which is acceptable to make good point contact.

Some other materials, however, are quite fragile, so that polishing can not ensure a sharp tip. For those materials, it is convenient to create a very sharp tip with atomic level size with simply breaking it apart. The fresh edge usually contains a few atomic layers so that it is perfect for Andreev Reflection measurement. One of this kind of material is $La_{0.67}Sr_{0.33}MnO_3$ (LSMO), which is a half metal with spin polarization as high as 80%. Figure(5.9) shows the experimental spin polarization of LSMO that is used in this dissertation work. It has been measured with a well known superconductor, Pb. The spin polarization value is decided to be higher than 80% when the scattering factor, Z, is smaller than 0.2. Therefore to get good Andreev Reflection measurement, a well prepared tip is of great importance.

Sample Mount Preparation

As is discussed in the previous section, the interface of normal metal and superconductor in the ARS is as small as a few micron. Thus, during the experiment process,

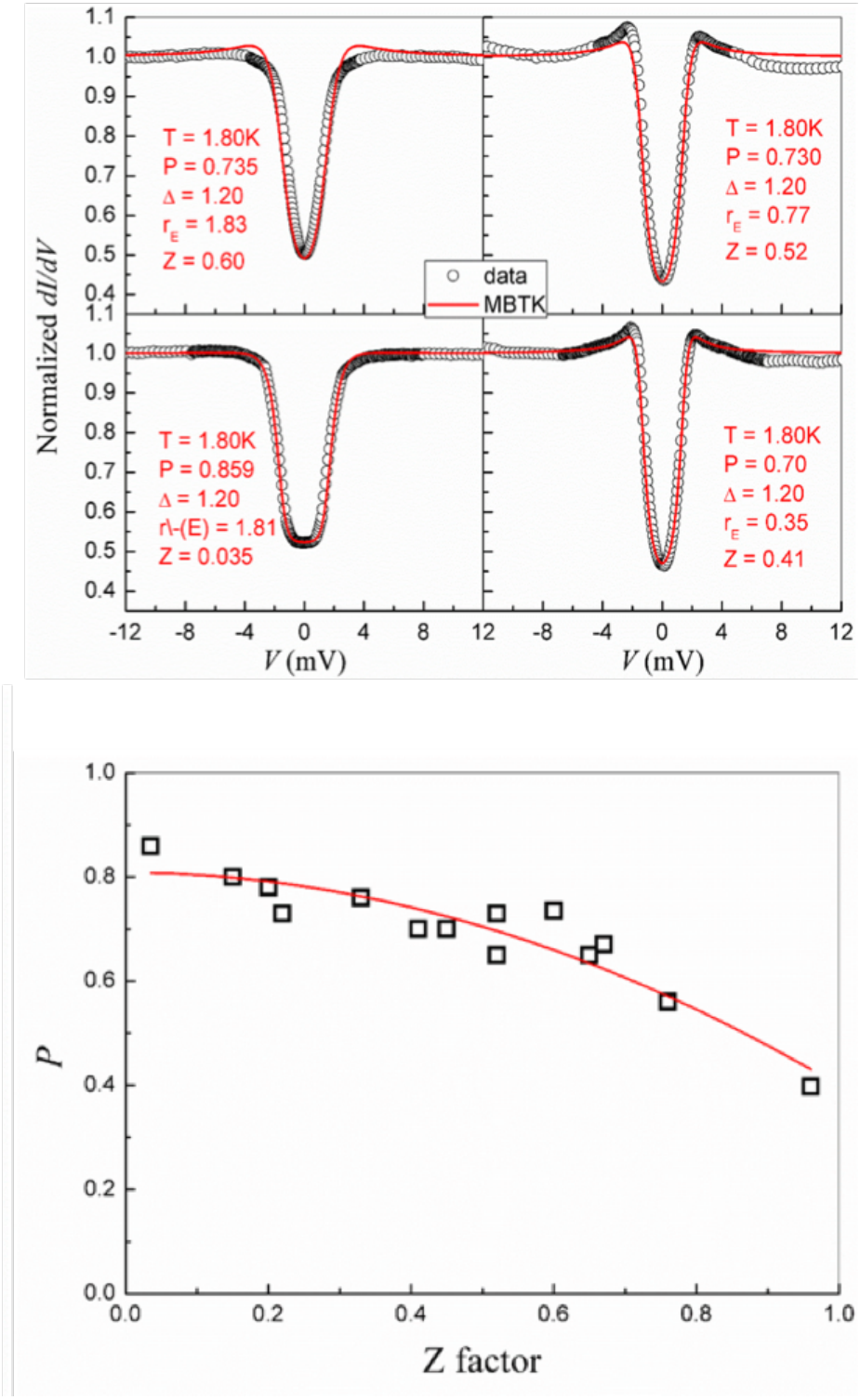

Figure 5.9: Top: ARS measurement of LSMO/Pb with different scattering factor (Z). The open circles represent the raw data and the red curve is the best fit with the mBTK model. Bottom: Spin polarization of LSMO with different scattering factor. The red line is served as eye guideline. Larger scattering factor makes the measured spin polarization value smaller.

any small perturbation can cause the change of contact, which is highly undesirable. On the other hand, Andreev usually appears at low temperature, due to the need of a superconducting state. Therefore, the mounting of the sample is the key for a successful measurement.

Figure(5.10) shows the sample mounting configuration that is used in this dissertation work. The total rod is about 60 in long. The sample is mounted to the bottom of the rod, and the four wires on the sample for the 4-point measurement is connected to the wire connectors on the top of the rod. Therefore, the sample is far away from any measurement instruments, which can greatly reduce the noise. A well prepared sharp tip is placed right on top of the sample, without touching the sample surface before experiment. The tip is connected to a differential screw, the position of which can be adjusted by rotating the turning rod on top of the rod. Each full turn of the rod is about $25\mu m$, which makes it convenient to precisely control the position of the tip. The interface of the sample can be changed by rotating the turning rod, so that the contact size, as well as the scattering factor and contact resistance, can be different. Only when the contact size reaches the ballistic regime, the Andreev reflection curve can be successfully measured. The whole rod is enclosed into a vacuum jacket. Before experiment, the jacket is pumped to reach a vacuum level about $10^{-6} torr$. After that, pure Helium gas is sent into the jacket to reach a ambient pressure. The Helium gas is served as an exchange gas for efficient cooling down of the sample, and also prevent any other gas, such N_2, moisture, from entering the vacuum jacket during or after the experiment, in order to protect the electrical wires inside.

5.5.2 ARS Electrical Setup

The Andreev reflection measurement is conducted by measuring the differential conductance, dI/dV, of the point contact. The electrical setup is shown in figure(5.11). The current is sent into the sample by the Keithley 6221 current source. And the voltage is measured by Keithley 2182A nano voltmeter. A Stanford 830 DSP Lock-in Amplifier is used to send a small sinusoidal current to the tip, in order to tell if there is any point contact established inside the sample tube. The resistance shown in the amplifier also indicates the contact resistance. By rotating the turning rod on top of the sample tube, the resistance will change, which represents a change in the contact size and scattering factor. All the electric cables are connected to a home-made switch box, in order to reduce the electrical noise. A Keithley 7001 Switch System is used to switch between different measurement channels. Therefore, the differential conductance and the temperature in side the sample tube can be measured simultaneously. A LM-500 Liquid Cryogen Level Monitor is connected to the liquid Helium dewar in order to monitor the real-time liquid Helium level. The ARS can only work when the Helium level is larger than 12 inches from the bottom of the reservoir because of the superconducting magnet located over there. In order to run the system safely, the magnet has to be submerged into the liquid Helium all the time. A Cryocon 32B Temperature Controller is used to monitor the temperature inside the sample tube. However, this value is just as a reference because the measured value is the temperature of the exchange gas, instead of the real temperature on the sample, which has to be measured by measuring the resistance of the thermal coupler located on the back of the sample. A Model 4G Superconducting Magnet Power Supply is used to control two superconducting electromagnets, one in the vertical direction and the other one is in the horizontal direction. Usually, the largest field for the vertical

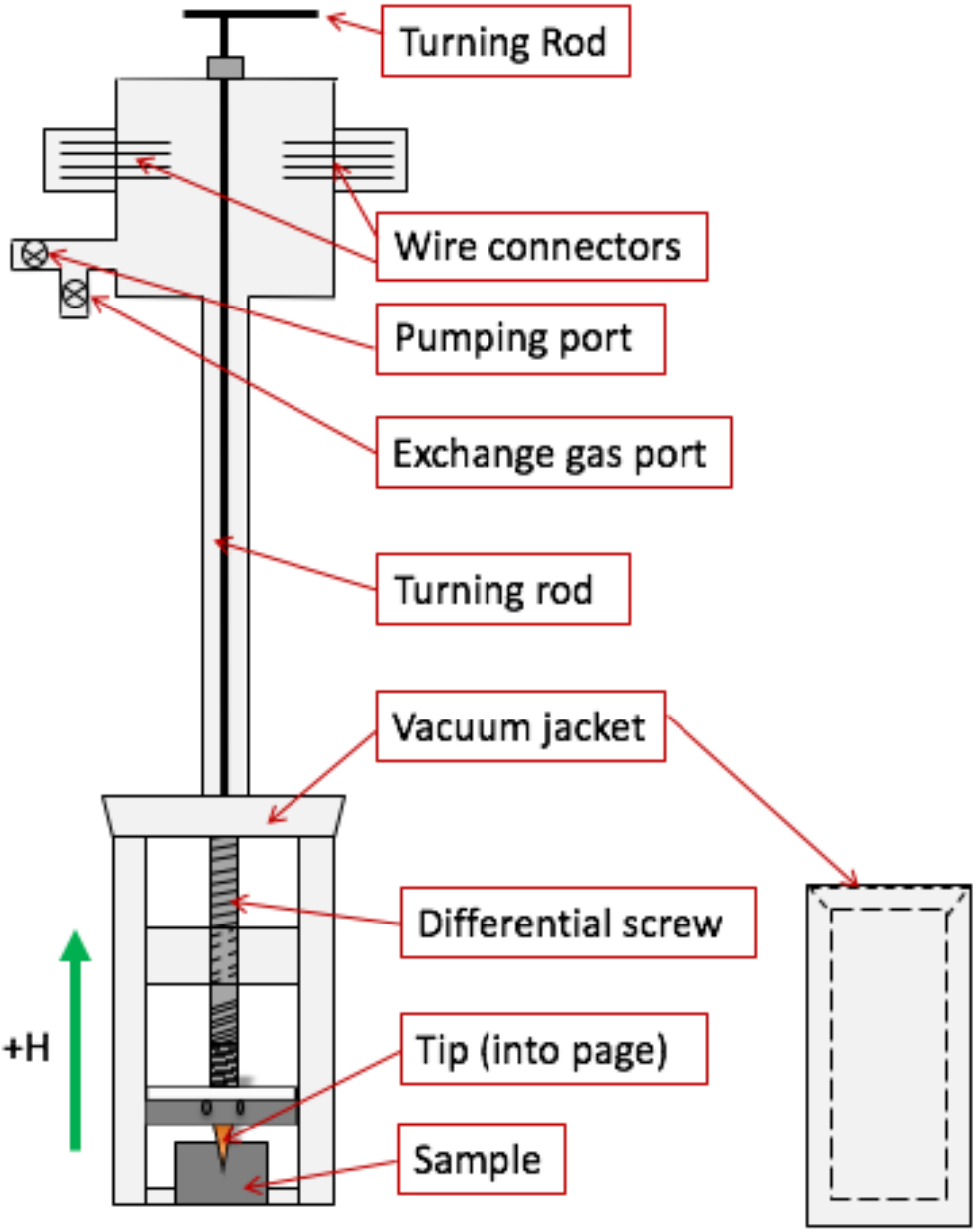

Figure 5.10: Sample mount configuration of ARS.

field can be as high as 9T, and the horizontal one can be around 5T. In order to achieve such high magnetic field, a large current has to be sent to the magnets, which is the reason that the magnets should be submerged into the liquid Helium all the time.

5.5.3 ARS Cryogenic Setup

Due to the necessity of a superconducting state in the Andreev reflection measurement, it is important to maintain a low temperature during the measuring process. ARS uses liquid Helium as cryogen to realize a temperature of about 4.2K, and even lower temperature can be realized by pumping the system.

A sketch of ARS cryogenic setup is shown in figure(5.12). A 4-layer-jacket structure makes the low temperature stable and the liquid Helium can be used for a relative long period. The most outside jacket is a vacuum jacket. Before the initial cool down, a turbo pump is used to pump this jacket in to a vacuum of $10^{-7} torr$. After the pump procedure, this jacket is well sealed by a valve so that the vacuum can remain for a long time. This good vacuum layer will protect all the inside cryogen from contacting the outside environment so that the cryogen will vaporized very slow. Next layer is a liquid Nitrogen jacket. Before the experiment, this jacket is also pumped to a good vacuum about $10^{-5} torr$ to remove all the moisture inside the system, in order to protect the system from any frozen. This jacket will prevent the liquid Helium layer to be contacted with room temperature and keep the inside system at a low temperature, which will save the liquid Helium. Important to mention that the liquid Nitrogen needs to be refilled every 6 hours due to the vaporization. Next to the liquid Nitrogen jacket is another vacuum jacket, which is also pumped to a good vacuum of 10^{-7} initially. This layer will further protect the liquid Helium from contacting on the relative higher temperature liquid Nitrogen layer, which greatly slows the vaporiza-

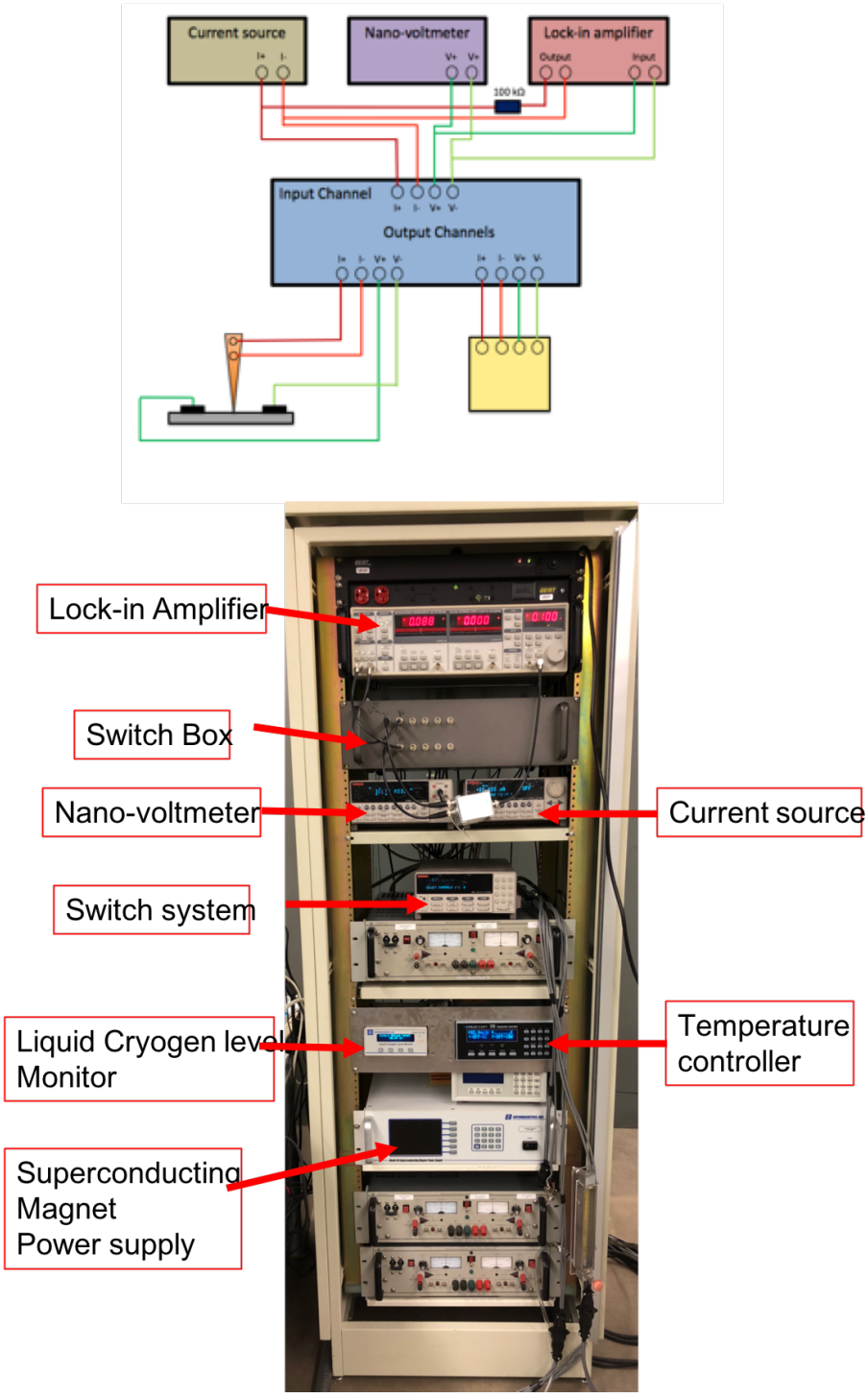

Figure 5.11: ARS electrical setup.

tion process of the Helium so that the experiment can last longer. The last jacket is a 50 litter liquid Helium reservoir, on the bottom of which installed two superconducting magnets. In the center of the ARS is the sample tube, which is separated from the liquid Helium reservoir by a needle valve. After mount the sample on the sample rod, it is inserted into the ARS sample tube area. Then the needle valve is opened to allow liquid Helium to enter this space, in order to cool down the sample. The location of the sample is right in the center of the two magnets so that the amplitude and direction of the field can be accurately controlled by the operator.

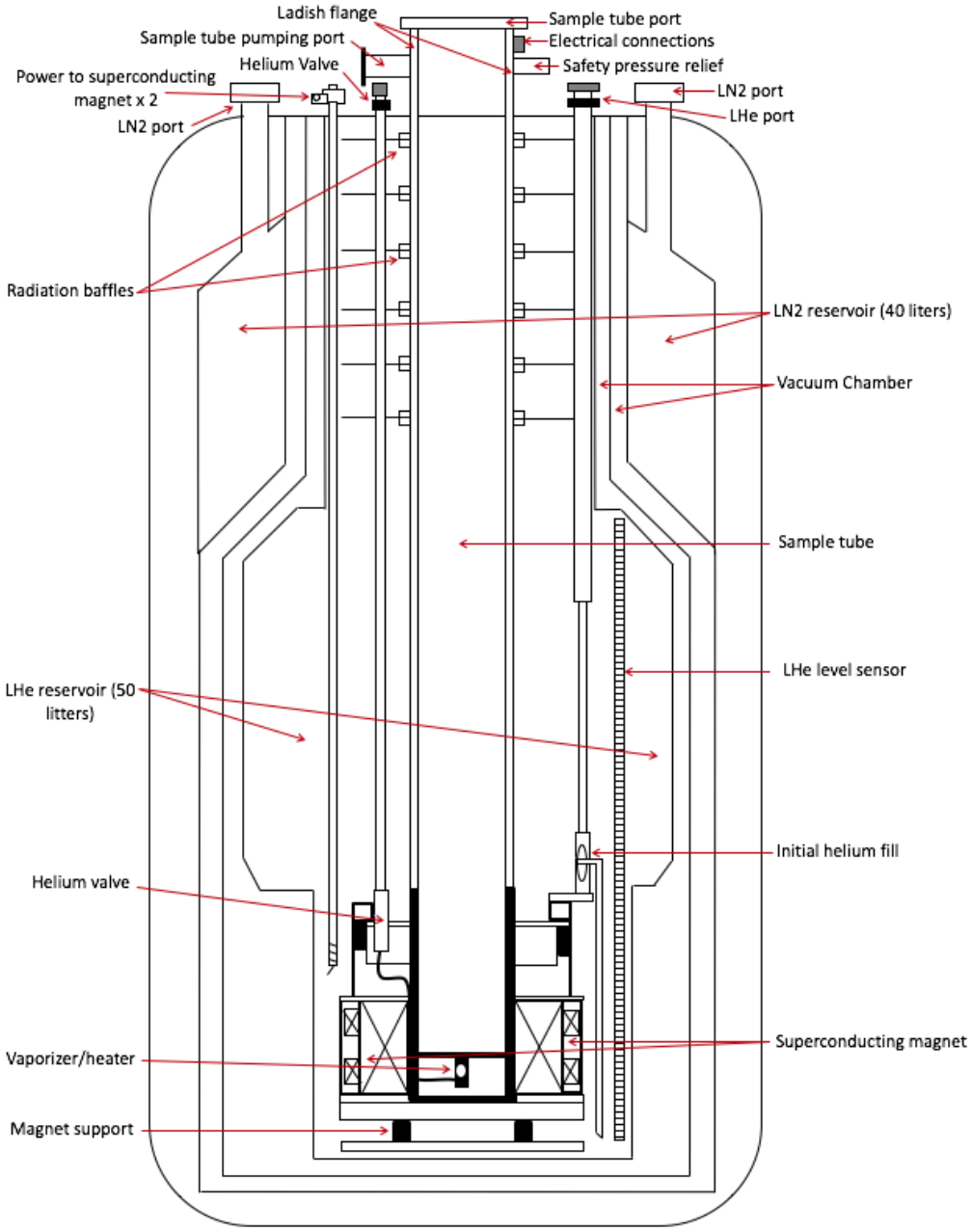

Figure 5.12: ARS cryogenic setup.

Chapter 6

SPIN POLARIZED CURRENTS IN PERPENDICULAR MAGNETIC STRUCTURES

Magnetic materials or structures with magnetization direction perpendicular to the surface are said to have perpendicular magnetic anisotropy (PMA). PMA materials can be used to fabricate, magnetic recording medium, which is of great importance in the data storage technique. Compared with the conventional longitudinal recording medium, the higher areal density of perpendicular material enables the higher capacity. On the other hand, the development of thin film deposition technique further improves the storage and reduces the sizes of the devices sizes, which is the key to integrate more storage in a smaller area. Nowadays, more and more data memory devices are based on perpendicular magnetic materials, including magnetoresistive random access memory (MRAM), hard disk drives etc. Therefore, it is of great importance to study the mechanism and magnetic behaviors of those perpendicular magnetic structures.

6.1 Motivation

Magnetic recording is the storage of data on a magnetic medium. As of today, this technology is widely used in the storage of computer data, audio and video signal. In 1928, Fritz Pfleumer developed the first magnetic tape recorder[55], which was designed to record analog audio signals. Later, with the rapid development of computer science, analog recording gradually faded and has been replaced by the digital recording technology.

For analog recording, the writing head magnetizes the tape with a magnetic field,

which is produced by a current proportional to the strength of the signal. After the writing process, the amplitude of the remnant magnetization is proportional to the applied field, thus the original signal. During the read out process, the read head reads the magnetic field produced by the magnetized tape, and then reproduces the original signal. This recording technology was popular in the past 30 years, but has declined popularity nowadays due to the limited storage space, slow speed and relatively large size[56].

Instead of creating a magnetization proportional to the signal strength, the digital recording just requires a bistable state, i.e. '0' and '1'. For some magnetic materials, the sharp switching of magnetization with applied magnetic field provides such advantage. Generally, digital recording media can be classified into two categories. Volatile memory provides a temporary storage of data for computing or programming purposes. However, the data will be lost after the power is shut off. On the other hand, the non-volatile memory is a media that can store the data for a long time. Such kind of memory includes floppy disks, hard disk drives (HDDs), flash memory etc[57].

For magnetic recording media, information is stored in a lot of tiny units, called bits. Each bit consists of hundreds of single domain magnetic elements, such as nano particles and grains. The anisotropy of the material decides the switching of the medium, therefore, the accuracy of the recording. To achieve reliable accuracy, the recording material should be able to be magnetized with a reasonable field, which requires the material to have a proper coercivity and saturation field[23]. If the coercivity and saturation field are too large, the material is hard to be magnetized. In this case, small magnetic fields, which are produced by relatively weak signals, can not be recorded and information will be lost. On the other hand, however, if the coercivity and saturation field are too low, the recording bits are so easy to be

magnetized that all the noise will be recorded as well.

In spite of the coercivity and saturation field, a large remnant magnetization is also required4. After the writing process, the information is supposed to be stored and should be able to be read out for a long time range. If a material has small remnant, the magnetization of the bit will become much smaller, which can not provide a magnetic field strong enough to be read out.

To achieve higher storage in a small volume, the bits have to be located on a circular track in a disk, instead of sitting along a straight line, as the tape does. The disk needs to be controlled to move at a certain speed, which is slow enough for a write head to write information in the bits and fast enough for a read head to read information continuously. Thus the bits must pass the head at a regular clock speed and they must be arranged with strict spatial periodicity[23].

6.1.1 Longitudinal Magnetic Recording

In conventional longitudinal magnetic recording media (LMR), the easy axis of each particles in one bit is along the track direction (figure(6.1))[58]. The current generated by the signal will produce a magnetic field at the write head according to the Faraday's Law. For longitudinal medium, the particles in each bit have an easy axis along the track direction. Therefore, the tangential component of the magnetic field, which is called fringe field, will magnetize each bit to its easy axis.

After the writing process, the magnetization of each bit will generate a magnetic field around it (figure(6.2))[23]. For a single bit with thickness δ in the y direction and w in width, the magnetic field can be calculated with:

$$H_x(x,y) = \frac{4\pi M_r}{\pi}[arctan(\frac{y+\delta/2}{x}) - arctan(\frac{y-\delta/2}{x})] \tag{6.1}$$

When $y = 0$, i.e. at the surface of the bit, the field becomes:

$$H_x(x,0) = \frac{4\pi \times 2M_r}{\pi}[arctan(\frac{\delta}{2x})] \approx \frac{4\pi M_r \delta}{\pi x} \tag{6.2}$$

Therefore, the strength of the field produced by one bit is proportional to the product of the remanence (M_r) and the thickness of the recording material. The field of a single magnetic transition is plotted in figure 3 for y=0 (thin solid line) and y=0.5 (thin dash line).

In reality, the bits are close to each other. And the boundary between neighboring two bits is not sharp. The magnetostatic energy at the transition is minimized by a smearing of transition over a length a long the track direction:

$$M_x(x) = \frac{2M_r}{\pi} arctan(x/a) \tag{6.3}$$

This magnetization decreases with the stray field:

$$H_x(x,y) = \frac{4\pi M_r}{\pi}[arctan(\frac{y+a+\delta/2}{x}) - arctan(\frac{y-a-\delta/2}{x}) - 2arctan(\frac{a}{x})] \tag{6.4}$$

The field for $a = 0.5$ and thickness $\delta = 1$ is plotted in figure(6.2) for $y = 0$ (thick solid line) and $y = 0.5$ (thick dash line).

For a disk, there are a lot of bits on a track. In this way, the shape of the stray field on top of the bits are roughly sinusoidal, and drops off exponentially with distance above the disk:

$$H_x \propto e^{-ky} sin(kx) \tag{6.5}$$

$$H_y \propto e^{-ky} sin(kx) \tag{6.6}$$

where $k = \frac{2\pi}{\lambda}$ and λ is the wavelength of the recorded bits (figure(6.3)). From the above equations, we can see one the limits of the longitudinal medium. To improve

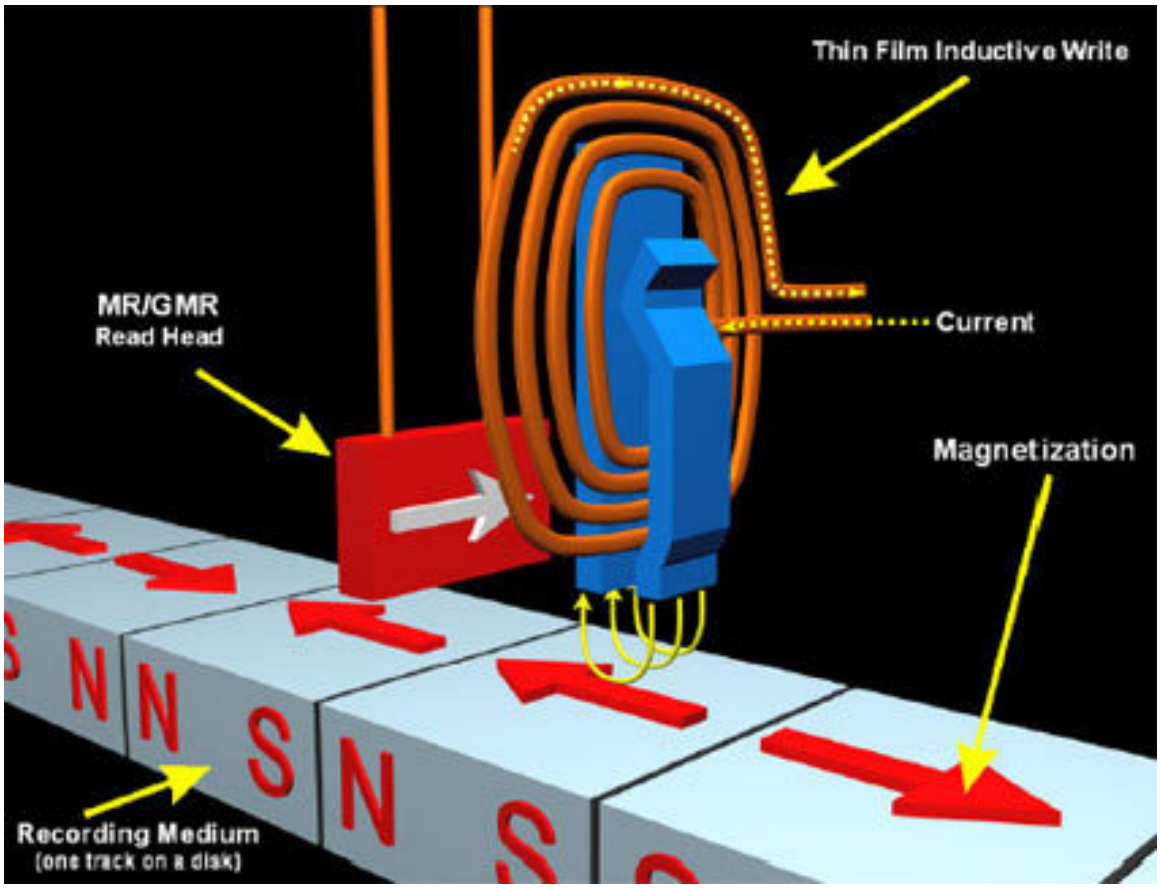

Figure 6.1: The bits in the longitudinal medium is magnetized by the fringing field from the write head. The direction of the magnetization represents the information being written. The read head is based on a GMR structure, which will sense the change of the magnetization of each bits, and get '0' or '1'.[58]

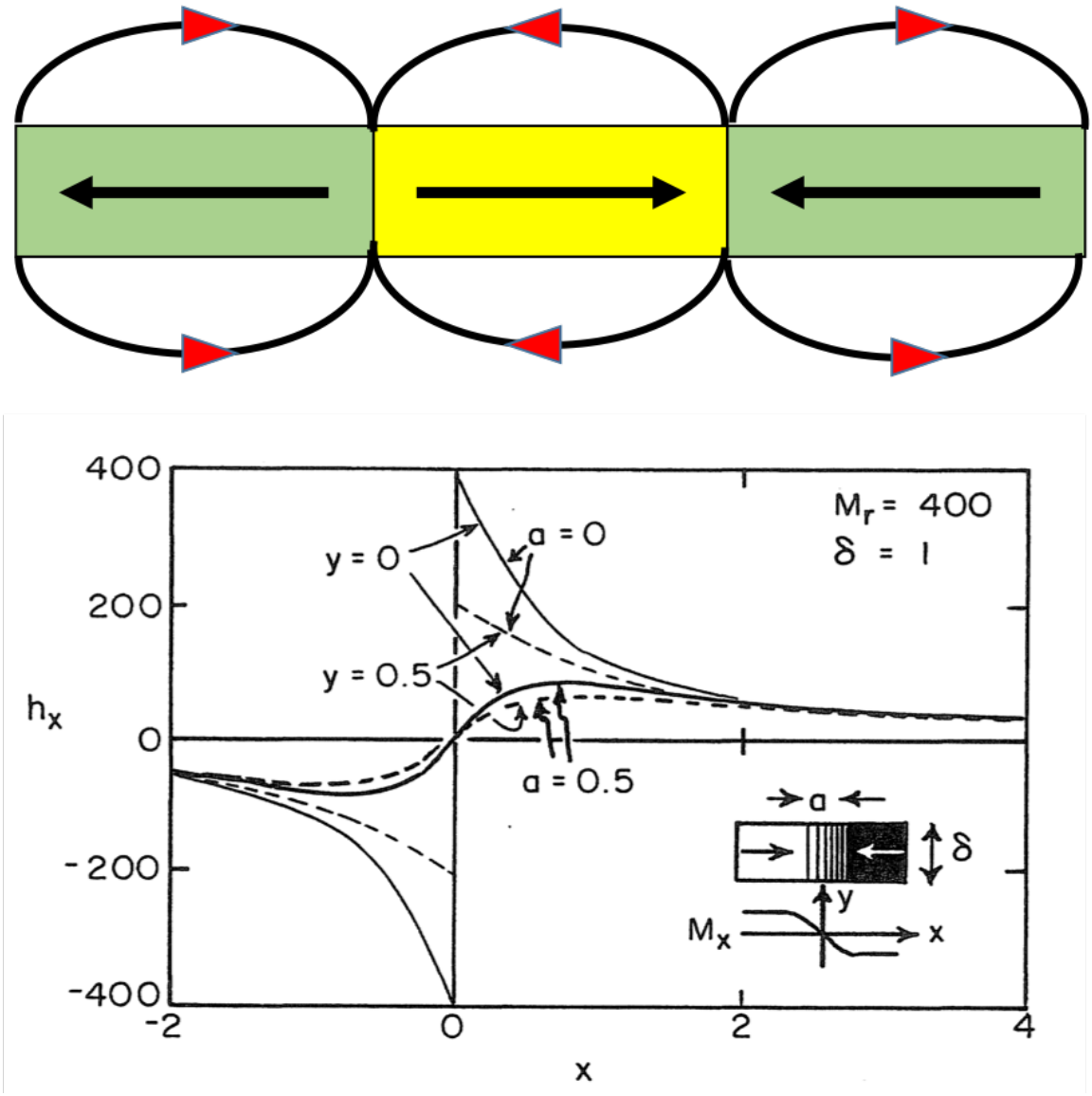

Figure 6.2: Top: The bits with different magnetization will generate different magnetic field around themselves. Bottom: Magnetic field on different location around two neighboring bits with opposite magnetization.[23]

the storage capacity, the bit density should be higher, which means each bit must be smaller. From figure(6.3) we can clearly see that smaller bit size means smaller λ, thus larger k. In this case, the stray field decays more rapidly so that the write and read processes become harder. On the other hand, theoretical study shows that for longitudinal recording bits, the demagnetization factor is:

$$N_L = \frac{M_r t}{\lambda} \tag{6.7}$$

So smaller wavelength also means larger demagnetization factor, which makes the medium more difficult to be magnetized. To reduce N_L, the thickness of the medium should be reduced. However, decreasing the thickness means decreasing the signal strength, which makes the medium unfavorable for recording purpose. One way to break the limit of the longitudinal medium is to use perpendicular recording medium, the easy axis of which is perpendicular to the medium plane. In this situation, the demagnetization becomes:

$$N_P = \frac{M_r \lambda}{t} \tag{6.8}$$

Therefore, the recorded information can be packed with greater density.

6.1.2 Perpendicular Magnetic Recording

Perpendicular magnetic recording (PMR) was first proven advantageous in 1976 by Professor Shun-ichi Iwasaki in Tohoku University in Japan[59]. PMR media break the thermal limit of the longitudinal media, and allows higher areal density. In 2005, Toshiba produced the first commercially available PMR disk drive, which had a size of 1.8 inch and a storage of 80 gigabytes. Later in January 2006, Seagate Technology began selling its first 2.5-inch hard drive with perpendicular recording technology. One year later, Hitachi announced the first 1 terabytes hard drive. In 2009, Western

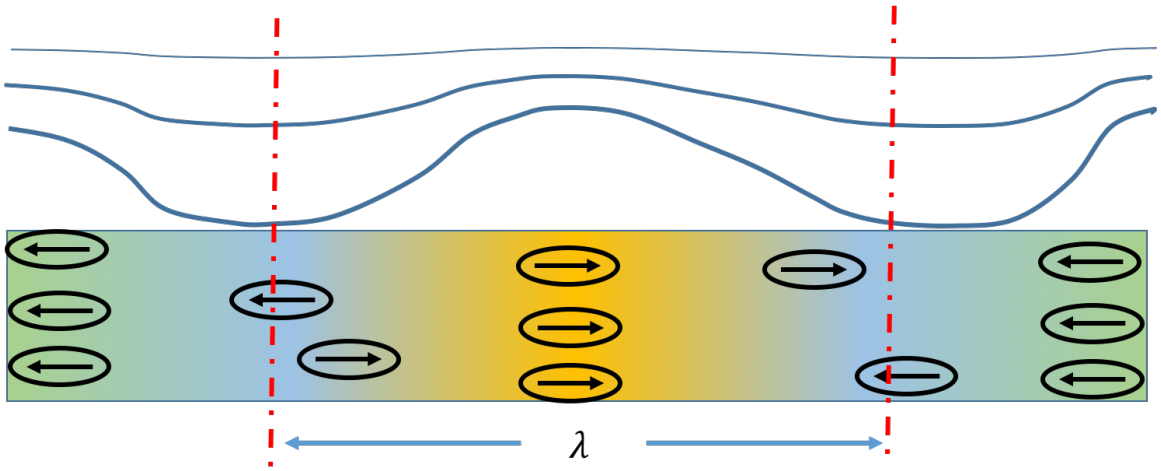

Figure 6.3: Each magnetized bit produces a magnetic field around it. When consider all the bits, the field form a sine distribution. The field decays exponentially with the distance to the surface of the bits.

Digital announced the first 2.0 terabytes SATA hard drive with PMR. In the figure 6.4 , a sketch of the PMR structure from Hitachi is shown.

The whole structure was deposited on a glass or metal substrate. Two soft magnetic underlayers was separated by a spacing layer. With a proper thickness of the spacing layer, the magnetizations in the two neighboring would form anti-ferromagnetic coupling, which is a reliable reference layer for recording. The seedlayers would provide a special growth direction of crystal in the later process, and the growth underlayers served as a buffer layer to reduce the lattice match and improve the crystal quality. The oxide-segregated magnetic layers were the true recording layer, with a magnetic easy axis perpendicular to the thin film. On top of the recording layer, a thin layer of carbon overcoat was deposited. During the writing and reading processes, the write head and read head are very close to the disk, usually tens of nanometer. The overcoat layer would prevent the recording layer from being damaged when the heads accidentally touch the disk.

For a good recording material, the squareness of the M-H loop is the key factor to ensure the bistable state for digital recording. The loop squareness can be defined as[23]:

$$S = \frac{M_r}{M_s} = m_r \tag{6.9}$$

where M_r is the remanence and M_s is the saturation magnetization. However, this factor can not well describe the squareness because it can not express the change of magnetization when the field changes direction. A modified squareness factor can be written as:

$$S^\star = 1 - \frac{M_r}{\chi_0 H_c} \tag{6.10}$$

Figure 6.4: Perpendicular magnetic recording structure used in Hitachi.[60]

where H_c is the coercivity of the material and χ_0 is the susceptibility. If the $S^\star$ is larger, the magnetization switching is sharper, which means better perpendicular magnetic anisotropy.

The early recording media for digital recording were mostly making use of the particulate materials1, which the anisotropy mainly came from the shape anisotropy of the unit particles. With the rapid development of thin film technique, the particulate media have been replaced by thin film materials, which can greatly reduce the size of the devices. For thin film media, the required anisotropy comes from the crystal anisotropy, therefore, the crystal direction is an important factor to consider.

Perpendicular media are generally deposited on a thin layer of high permeability, longitudinal material. For writing process, when the head, which has a tip size as small as one bit, passes each bit, the field will magnetize it. The high permeability underlayer effectively creates an image pole tip, focusing the flux. To form a complete magnetic field loop, a return pole, which has a much larger size, should be made. The focused flux in the underlayer can go back to the return pole, through the recording layer. The coercivity of the recording layer should be fairly high, and the size of the return pole should be large enough that when the magnetic flux passes though the media layer, the magnetization in those bits will not be changed (figure(6.5))[23].

Noise in Perpendicular Media

Compared with particulate media, thin film is more prone to noise. This is because for a particulate media, each particle is almost completely isolated with each other. And the larger particle size reduces the effect of noise. However, for a thin film medium, the grain boundaries are narrow enough so that the adjacent grains tend to couple by exchange coupling or dipole field. Thus at the boundary of each bit, a zigzag domain wall will be formed with an amplitude[23]:

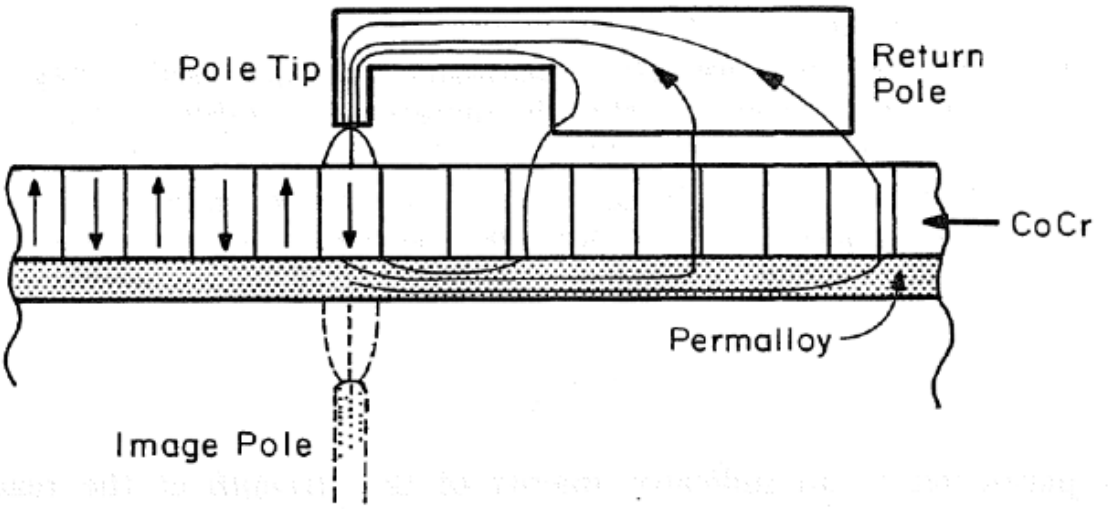

Figure 6.5: In perpendicular recording structure, the pole in the write head can be much smaller than that of the longitudinal structure. The focused magnetic flux can switch the magnetization more efficiently, reducing the power consumption.[23]

$$Z \sim \frac{M_s^2}{K^{1/2}} \tag{6.11}$$

Where M_s is the saturation magnetization and K is the anisotropy coefficient. From the equation, one way to reduce the noise is to increase the anisotropy. However, this is not an easy way since the increased anisotropy will make it harder for the write process. Another method is to increase the bit density, which will increase the signal to noise ratio (SNR):

$$SNR \propto N^{1/2} \tag{6.12}$$

6.2 Mechanism of Perpendicular Magnetic Anisotropy

Perpendicular magnetic anisotropy can be found in several materials and structures. For multilayer structures, Co/Pt, Co/Pd, Co/Ni, CoFe/Pd, CoFe/Pt, Co/Cr/Pt etc. can all show perpendicular magnetization. On the other hand, some alloys, such as CoFe, CoPt and CoCr, and some rare earth transition metals (RE-TM), also have the similar property. For any magnetic materials, the crystalline and stress-induced anisotropy have effect on the direction of easy axis. If the materials become thinner and thinner, the surface and interface anisotropy dominate the direction of the magnetization.

Co/Pt bilayer structure is one of the earliest perpendicular magnetic anisotropy structures people studied. The bulk Cobalt has a hcp structure, which makes the easy axis of Co along the c direction. For a single layer of Co, however, the magnetization easy axis is usually in plane, which is determined by the strong shape anisotropy of the thin film structure. However, when a very thin layer of Co is deposited on top of a thin layer of Pt, the easy axis will be pulled our of plane. In this structure,

besides the shape anisotropy of the thin film, other anisotropy also have effect on the magnetization.

Magnetocrystalline Anisotropy

Magnetic anisotropy is used to describe the internal energy dependence on the direction of the spontaneous magnetization. Generally, magnetic anisotropy terms has the same symmetry as the crystal structure, which is also called magnetocrystalline anisotropy. For Cobalt, the easy axis of magnetization is along the c axis, which makes a uniaxial anisotropy. As the magnetization is pulled away from the easy axis, the internal magnetic energy will increase with the increasing of the angle θ. Usually, this energy can be expressed as[23]:

$$E_a = K_{u1}sin^2\theta + K_{u2}sin^4\theta + K_{u3}sin^6\theta + K_{u4}sin^6\theta cos6\varphi \tag{6.13}$$

where $K_{ui}\ with\ i = 1, 2, 3...$ are the anisotropy constant, θ is the angle between the magnetization $\mathbf{M}$ and the easy axis, and φ is the azimuthal angle of the magnetization in the plane perpendicular to the easy axis. If the constants K_{ui} are positive, the magnetic energy is minimum when the angle θ is zero, which represents easy axis; otherwise, the energy is maximum at zero angle, indicating the hard axis. Since $sin\theta$ and $cos\theta$ are smaller than 1, the first two terms are usually much larger than the rest. Therefore, for most purposes, it is sufficient to only keep those two terms.

For Cobalt at room temperature, the experimental anisotropy constants are:

$$K_{u1} = 4.3 \times 10^5 J/m^3\ and\ J_{u2} = 1.5 \times 10^5 J/m^3 \tag{6.14}$$

So the Co anisotropy is zero when the magnetization is along the easy axis, and gradually increase when the magnetization are pulled to other directions.

Shape Anisotropy

As is mentioned in the previous section, the bulk Co has a hcp structure, which makes the c axis a preferable direction for spontaneous magnetization. However, for Cobalt thin film, the situation will be different [61]. When deposited on a crystallized substrate, the Co thin film may form a fcc structure, which has a (111) plane. In this case, the uniaxial anisotropy does not apply anymore. Instead, for cubic structures, usually the cubic anisotropy will apply. Therefore, the perpendicular axis is no longer an easy axis. The cubic anisotropy will make the easy axis along the $x, yandz$ directions, and for (111) plane, the magnetization will lie in the thin film plane direction.

On the other hand, for thin film Co, another anisotropy, called shape anisotropy, starts to dominate. The magnetic moment of each atom can be regarded as the result of the magnetic dipole, which is similar to the electric dipole moment. In this method, assume there exists magnet poles (positive and negative), and the two poles with opposite sign will form a dipole, therefore, a moment. For Co thin film, if the magnetization is out of plane, then there will be free poles on the surface, which will increase the magnetostatic energy. Even if the whole thin film has many tiny domains, since in each domain, the magnetic moments are either point up or point down, therefore the density of magnetic free poles on the surface will not decrease. Thus, the perpendicular direction is not preferred for spontaneous magnetization.

However, if the magnetization is in plane, there will be no magnetic free poles on the surface of the thin film. Instead, they only exist at the two ends of the sample. Since for a thin film, the size of the surface is much larger than that of the two ends, the magnetic free poles are much fewer in this case, which greatly reduces the magnetostatic energy, no matter how many domains exists inside the film. Therefore, the shape anisotropy dominate the magnetization direction of the Co thin film.

Magnetoelastic Effects

During the process of magnetization, the shape of the specimen of ferromagnetic materials may change. The external and internal magnetic field will change the crystal constant slightly, and causes strain. This is called magnetostriction. Even though the deformation is quite small, it may change the magnetic property of the material, especially for thin films.

The deformation is often expressed by $\delta l/l$, where δl is the change in shape during magnetization process and l is the original shape or size. Just like the magnetization can reach a saturation when the external field is large enough, the change of shape also has a limitation, which is called the saturation magnetoelastic, λ. In a ferromagnetic material, there exist many domains within which the directions of magnetization are different. Thus, the crystal lattice will spontaneously deformed in the direction of domain magnetization. When an external field is applied, the magnetization direction in each domain will rotate to the direction of the field, and eventually reach saturation when the field is large enough. In this case, the magnetostriction also researches saturation. Suppose the total change in the direction of magnetization is e, then the saturation magnetostriction can be calculated as[23]:

$$\lambda = \frac{\delta l}{l}|_{sat} - \frac{\delta l}{l}|_{dem} = \frac{2}{3}e \tag{6.15}$$

The origin of magnetostriction is the interaction between the magnetic moments from each atom. Suppose the distance of between two magnetic moments is r, which is variable in the magnetization process, then the interaction energy can be written as[23]:

$$w(r, cos\varphi) = g(r) + l(r)(cos^2\varphi - \frac{1}{3}) + q(r)(cos^4\varphi - \frac{6}{7}cos^2\varphi + \frac{3}{35}) + ... \tag{6.16}$$

where $g(r)$ is the exchange interaction between two moments, which is independent of the direction of magnetization. The second term represents the dipole-dipole interaction, which depends on the magnetization direction and is the principal origin of magnetostriction. The third term and all other terms are much smaller than the first two terms so that they are negligible. Therefore, the total interaction energy can be written as:

$$w(r,\varphi) = l(r)(\alpha_1\beta_1 + \alpha_2\beta_2 + \alpha_3\beta_3)^2 - \frac{1}{3} \tag{6.17}$$

where $(\alpha_1, \alpha_2, \alpha_3)$ represent the direction cosine of the domain magnetization and $(\beta_1, \beta_2, \beta_3)$ are for that of the bond direction. In a crystalized sample, the deformation of the lattice can be represented by the strain tensor, which can be used to calculate the bond direction $(\beta_1, \beta_2, \beta_3)$. Therefore, the the energy expressed in equation (6.17) is related to the lattice strain and the domain magnetization direction, and can be called magnetoelastic energy. Thus, the origin of magnetostriction is the magnetoelastic energy induced by the magnetocrystalline anisotropy of the deformed crystal.

The atoms at surface or interface will have different structure and magnetic properties with the bulk. The surface magnetism will depend on the atoms local environment such as the symmetry, the number of nearest neighbors, and the distance between the surface atoms and the bulk material.

At surface, the coordination and bonds are reduced which will lead to significant changes in electronic structure. For example, Ni has 28 electrons outside the nucleus, which has an arrange of $[Ar]3d^8 4s^2$. At the surface, each Ni atom has 9 nearest neighbors (for (111) surfaces) or 8 nearest neighbors (for (100) surfaces), while the bulk Ni atoms have 12 nearest neighbors. As the result, calculations show the magnetic moments at the surface are enhanced. The surface charges that go into the vacuum

are almost s and p electrons, while d electrons become more localized. This spatial separation of d electrons and s-p electrons increases the localization d electrons, thus the magnetic moments.

On the other hand, the atomic planes near the surface usually show a smaller distance to the bulk than that of the lattice constant. This is due to the lacking of bond of the surface atoms. At the surface, the compression of s band electrons are not as strong as in the bulk, resulting in a reduced s electron density, which leads to less screening effect to the d electrons on the surface. Therefore, the atoms at the surface experience stronger attraction and reduced repulsion from their neighbors, which will cause surface relaxation.

Besides surface relaxation, when a thin film is deposited on another material with different lattice constant, a large lattice mismatch will occur. The mismatch can be written as:

$$\eta = \frac{a_1 - a_2}{(a_1 + a_2)/2} \tag{6.18}$$

where a_1 and a_2 are the lattice constant for the two materials. When a thin film with thickness d grows on another thin film (or substrate), the elastic energy per unit area is proportional to $\frac{\eta^2 d}{2}$. And there exists an critical thickness, d_c, above which the strain energy will exceed the energy cost for the formation of dislocation. Thus, it is favored to form more dislocations. Calculations show that the critical thickness varies inversely with the strain. Generally, the average magnetoelastic energy varies approximately as $\eta(\frac{d_c}{d})^3$, which means the thinner the thin film is, the stronger the anisotropy will be.

6.3 Co/Pt Bilayer

Co/Pt bilayer structure is one of the earliest multilayer perpendicular magnetic anisotropy structures people discovered [62, 63]. This bilayer structure has several applications in industry, including the heat assisted magnetic recording media, magneto-optical studies, laser induced ultrafast demagnetization dynamics studies [64]. Generally, this multilayer PMA structure has larger coercivity, making it a good candidate for fabricating magnetic tunnel junction.

Bulk Co has a hcp crystal, with the lattice constant $a = b = 250.71pm$ and $c = 406.95pm$. Pt has a fcc structure with $a = b = c = 392.42pm$. The large difference in the lattice constants leads to huge lattice mismatch for this bilayer structure. This mismatch, which will cause large strain and magnetoelastic energy, pulls the easy axis of the Co thin film from in plane to out of plane. Besides, the atomic orbit interaction also has effect on the magnetic behavior. At the interface between Co and Pt, the strong hybridization will enhance the spin-orbit coupling, thus enhance the perpendicular magnetic anisotropy [65–68].

6.3.1 Sample Preparation

The Co/Pt bilayer structure is deposited on a Si substrate with a 500 μm thermally oxidized SiO_2 layer, by the DC magnetron sputtering system. The Ar base pressure is about $2 \times 10^{-8} torr$ under room temperature. To realize good PMA property, a layer of Pt buffer is deposited first, and then a thin layer of Co, about $4\mathring{A}$. Next, a thin layer of Pt, about $6\mathring{A}$, is deposited. Now a Co/Pt bilayer structure is formed. To realize stronger signal, another n periods of Co/Pt bilayers are deposited on top of the first one. So the whole sample is: $Pt(x)[Co(4)Pt(6)]_n$, where x means that the thickness of the Pt buffer layer varies, and n is the total period of Co/Pt bilayer.

First, to find the optimal Pt buffer layer thickness, a Pt wedge is deposited, with $x = 0\ to\ 60\mathring{A}$, and $n = 4$ is fixed. The Pt buffer layer will optimize the crystallization of the Co layer. And the Pt (111) plane is help for the Co (hcp) crystal growth so that the easy axis could be out of plane. If the there is no buffer layer, the thin Co layer on the substrate will turn to be (111) plane so that the easy axis tends to be in plane. After the sample is fabricated, it is cut into 6 pieces with the same size. To test if all the pieces have good PMA, anomalous Hall effect is measured for all pieces. The sample and the measurements results are shown in figure(6.6). As can be seen from the results, when the Pt buffer layer is thinner, a sharp switching loop is observed (piece #1 to #4). This means that in those samples, the easy axis of the Co layers are out of plane. If one takes a closer loop at the curve, one can see that the coercivity of the graph is about 360 Oe, which is large enough for the purpose of magnetic memory fabrication. Usually, the Co/Pt bilayer structures are used in heat-assisted magnetic recording. A laser (or other small heat source) is used to head the recording bits, reducing the coercivity and then the information can be written on them. On the other hand, the good square shape of the loop indicate a large remanence, making it suitable for permanently store the data. When the magnetic field generated by the write head magnetizes the recording bit, the magnetization will reach saturation and the information is written on the bit. After the writing process, the read head moves to another place, and the large remanence will keep the data, unless it is been written again. Therefore, large remanence is preferred for data storage.

For sample pieces #5 and #6, the squareness of the loop is not as good as the previous pieces. The coercivity is smaller, which makes the magnetization easier to be changed by a small field. This should be avoidable for data storage medium because smaller coercivity makes the recording bits easier to be switched by external noise. On the other hand, the smaller remanence is not suitable for data storage since it will

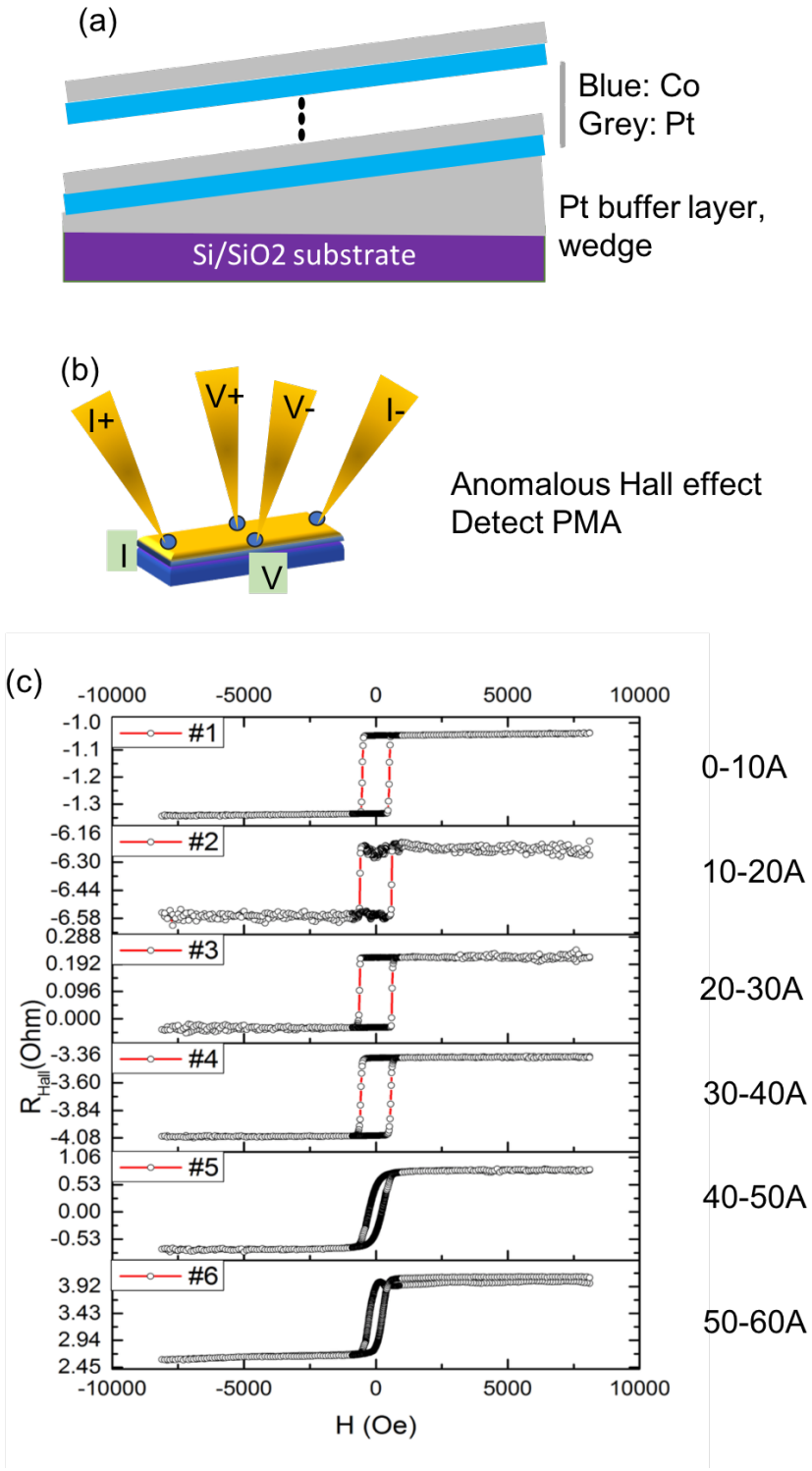

Figure 6.6: (a). Illustration of the sample with a wedge Pt buffer layer; (b). Illustration of anomalous Hall effect measurements; (c). Results of anomalous Hall effect measurements for different pieces.

generate smaller magnetic field for the read head, which will cause read fault. The reason for the worse PMA may due to the current shunting effect caused by the thick Pt buffer layer. The conductance of Pt is $0.96 \times 10^5 S/cm$, which is comparable to that of Co ($1.72 \times 10^5 S/cm$)[28]. Since the thickness of the buffer layer in pieces #5 and #6 is more than 10 times thicker than that of Co thin layer, most currents in those samples may flow through the Pt buffer layer, instead of the Co layer. Therefore, the magnetization information is lost.

Besides the optimal Pt buffer thickness, another interesting parameter to explore is the number of Co/Pt bilayer period. To study the period dependence of PMA, a series of samples with Co/Pt periods $n = 4, 8, 12, 16$ *and* 20, respectively, have be fabricated, with Pt buffer layer is $35\mathring{A}$. After the fabrication, the anomalous Hall effect measurements have be conducted on each sample, and the results are shown in figure(6.7).

From the results, one can see that when the number of period is 4, a good sharp switching is achieved. When the number of period increases, the squareness of the loops become worse so that the PMA property gradually disappears. When the number of periods is larger than 12, the remanence start to decrease, making it not suitable for fabricating data storage medium anymore. One of the reason is that with the number of periods increasing, the total thickness of Pt layer becomes thicker, which will draw much current flow inside. As a result, the electrons will suffer from scattering in the Pt layers and lose the magnetic information. On the other hand, the Pt thin layer might be magnetized due to the magnetic proximity effect. The magnetized Pt layer may have a magnetic easy axis in plane, which may affect the magnetization in the Co layer, through the exchange interaction. Pt is a material with a Stone criteria close to 1, which makes it easy to be magnetized[22].

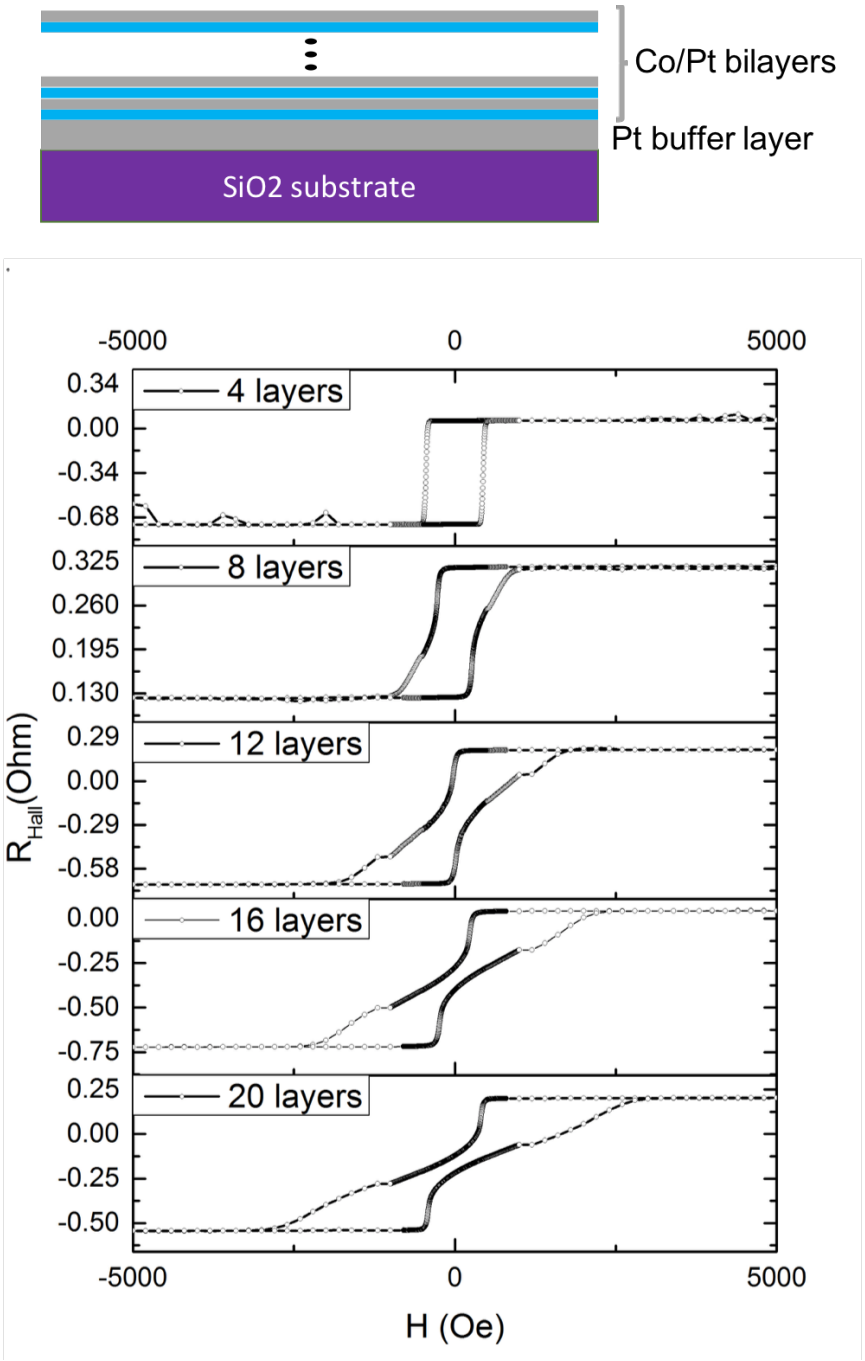

Figure 6.7: Top: Illustration of the sample with a different number of Co/Pt bilayer; Bottom: Results of anomalous Hall effect measurements on samples with different Co/Pt periods

6.3.2 HM/FM/Oxide Structure

Besides Co/Pt bilayer structure, which both layers are metal, nowadays people are more interested in another structure, namely Heavy Metal (HM)/ Ferromagnet (FM) /Oxide structure. This kind of structure is a promising candidate to fabricate high quality magnetic tunnel junction (MTJ). In MTJ structure, electrons tunnel through a thin layer of insulating barrier from a ferromagnetic layer to another. When the magnetization of the two ferromagnetic layers are aligned parallel, the resistance is minimum; while if they aligned antiparallel, the resistance is maximum. This behavior is first discovered by M. Julliere in 1975[10]

To realize good PMA behavior, Ta and Hf are chosen as the heavy metal, CoFeB is chosen as the ferromagnetic layer and MgO is chosen as the oxide layer. First calculation showed that the PMA property is induced by the interaction between Fe ion in the CoFeB and O ion in the MgO[69, 70]. Some experiment indicated that during the process of sample deposition, the B atoms may diffuse from the CoFeB layer to the bottom heavy metal, improving the Fe-O interaction, which will enhance the PMA[71]. On the other hand, some other studies showed that the interaction between the heavy metal and the CoFeB may also increase the PMA[72, 73]. Besides, Rashba effect and Dzyaloshinskii-Moriya interaction have also been extensively studied, in order to explain the current induced magnetization switching in the CoFeB layer[74–81]

The sample is fabricated by magnetron sputtering with a base pressure about $2.0 \times 10^{-8} torr$. A heavy metal layer, Ta, of 20 $\mathring{A}$, is sputtered on the thermally oxidized Si substrate. Next, a layer of CoFeB is grown, followed by a layer of MgO about $20\mathring{A}$. Then a thin layer of Ta (about $10\mathring{A}$) is deposited on top of MgO for protection.

Since the magnetic axis direction is determined by many factors, including the shape anisotropy, interface anisotropy, Fe-O interaction etc, it is important to find out the best thickness of CoFeB layer. The first sample fabricated has the structure $Ta(20)/CoFeB(0-10)/MgO(20)/Ta(10)$, with all the numbers in the units $\mathring{A}$. After deposition, the sample is cut into 9 pieces and anomalous Hall effect is measured for all the pieces.

From the results in the right of figure(6.8), one can see that when the CoFeB thickness is less than $4.4\mathring{A}$, the hysteresis loop is not a square, with a very small coercivity about 5 Oe and smaller remanence. On the other hand, the loop does not reach saturation when the field increases and thus shows a paramagnetic behavior. The reason may due to the very thin thickness of the CoFeB layer. When this layer is very thin, a continuous film may not be formed. In this case, the exchange interaction between the ferromagnetic atoms may not be strong enough so that the layer would show superparamagnetism. On the other hand, due to the lack of Fe atoms in the CoFeB layer, the interfacial Fe-O interaction may not overcome the shape anisotropy induced by the grain of CoFeB, which would have effect on the PMA. When the thickness is thicker than $5.5\mathring{A}$, good PMA can be observed from the squareness of the loop. With the thickness increasing from $5.5\mathring{A}$ to $8\mathring{A}$, the PMA remains and the coercivity increases to maximum at $6.6\mathring{A}$ and slightly decreases when the thickness is about $8\mathring{A}$. Therefore, the best thickness for PMA is about $6.6\mathring{A}$. When the thickness reaches $8.8\mathring{A}$ or higher, the loop squareness becomes worse, which indicates the fading of PMA property. This reason may be different from the case of very thin CoFeB layer. When this layer is thick, the thin film shape anisotropy will be stronger, so that the in plane exchange interaction of each layer may be stronger, which will overcome the perpendicular anisotropy at the interface between CoFeB and MgO. On the other hand, the B atom may not be efficiently diffuse to the bottom Ta layer, due to the

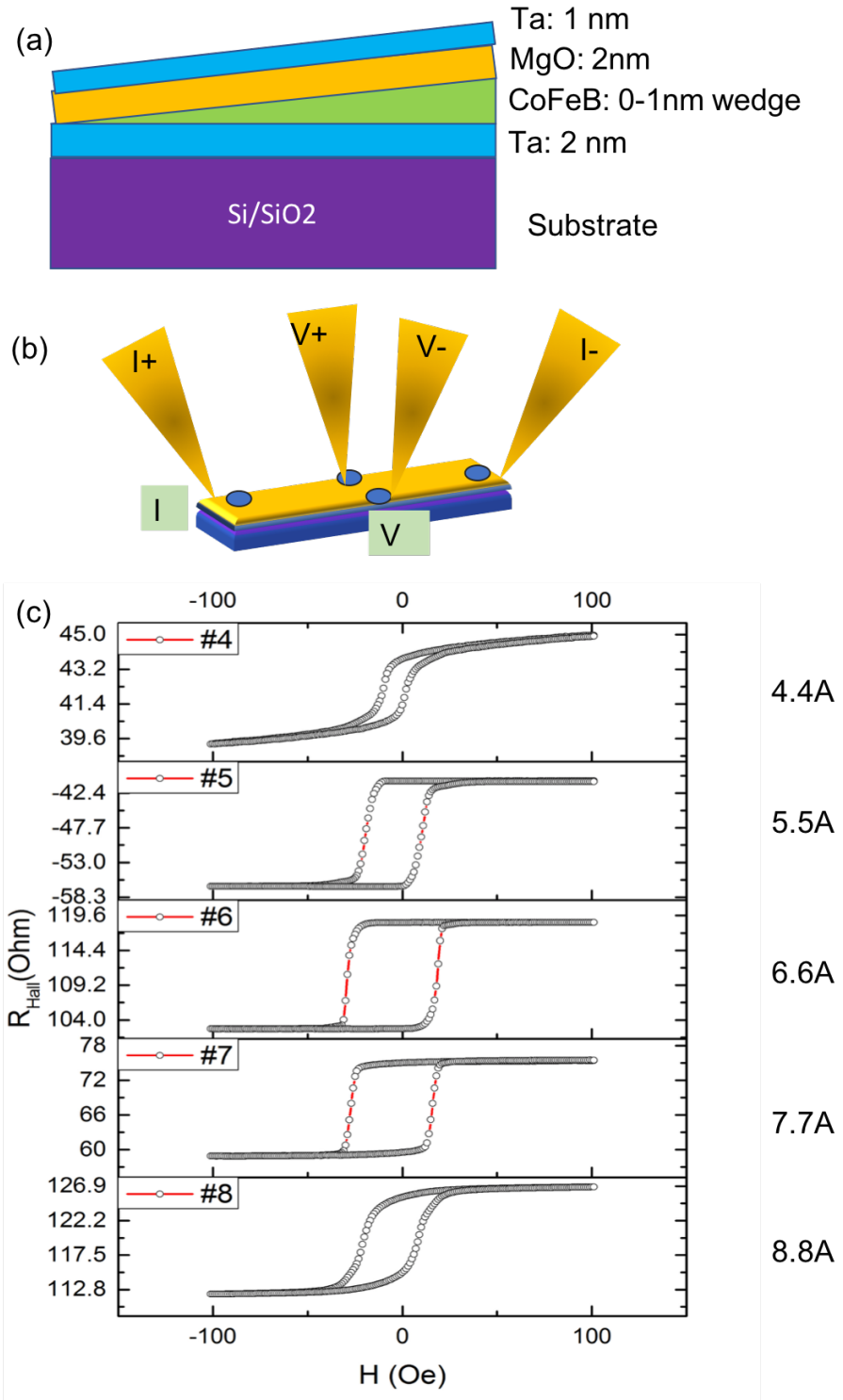

Figure 6.8: (a). Illustration of the sample with a CoFeB wedge; (b).Illustration of anomalous Hall effect measurement. (c). Results of anomalous Hall effect measurements on samples with different CoFeB thickness

thick CoFeB layer, which may jeopardize the PMA.

After find out the best thickness for PMA, a detailed Hall measurement is conducted for the sample pieces with the best PMA. As is shown in the figure(6.9), a current of 0.2 mA is sent into the sample through the two horizontal leads (indicated by the yellow dots), and voltage is measured through the two leads in the vertical locations. When the field is in the positive direction (assume from outside the paper to inside of the paper), and reaches saturation, all the magnetic moments are aligned with the field direction. The electrons will be deflected to one side of the sample, due to the external field and the magnetization direction, resulting in a electrical potential difference between the two sides of the sample. Assume the upside of the sample has a negative potential and the downside of the sample has a positive potential. When the magnetic field decreases, the magnetization of the sample holds to the same direction due to the strong PMA. And when the field starts to go to the negative direction, the magnetization starts to flip to the opposite direction, resulting in a decreased Hall voltage, thus a smaller Hall resistance. At some certain field, the Hall voltage will drop to zero, resulting in a zero Hall resistance shown in the loop, called zero Hall step. When the field keeps increasing to this direction, the Hall voltage stays at zero for a small field range, and then starts to change from positive to negative and keeps increasing in the negative direction. When the field is large enough, all the magnetic moments are flipped to align with the field, and saturation is achieved again.

One explanation of the zero Hall step is that there exists a slanted domain wall in the CoFeB layer. When the field is large enough so that the magnetization reaches saturation, there is no domain wall in the sample. Since in the sample, the CoFeB is a wedge, so when the field changes from positive to negative direction, the area with thinner CoFeB flip first. In figure(6.9), the blue area represents the flipped area, which has a positive potential on the upside of the sample and a negative potential

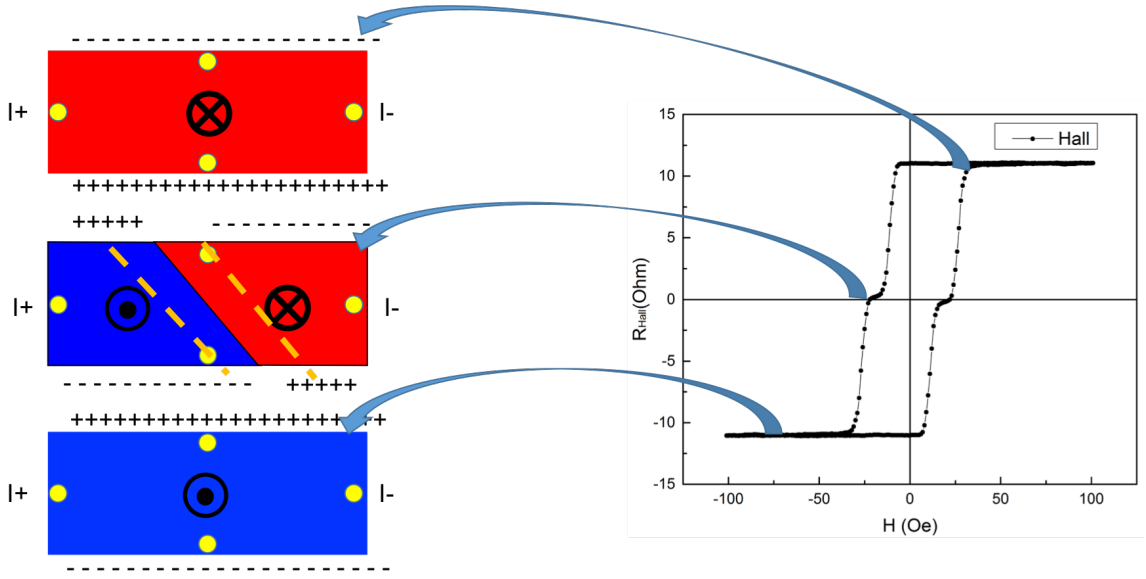

Figure 6.9: Left: Illustration of the anomalous Hall measurement. The four yellow dots represents the Indium leads. The two horizontal ones are the current leads and the other two vertical ones are for voltage measurements. The + and - sign indicated the electrical potential of the Hall signal on different locations of the sample. Right: Results of anomalous Hall effect measurements

on the downside of the sample, just opposite with the signs in the red area. When the field keeps increasing in the opposite direction, the slanted domain wall will move from left side of the sample to the right side of the sample. When the field reaches a certain value, the domain wall will cross the two voltage leads. The Hall resistance can be calculated by:

$$R_H = \frac{B_z}{nte} + \frac{R_s M}{t} \tag{6.19}$$

where B_z is the field in the z direction, n is the electron number density, e is the electron charge, t is the layer thickness, M is the magnetization and R_s is the anomalous Hall coefficient. From the above equation, the Hall signal only depends on the thickness of the CoFeB layer, so that as long as the slanted domain wall is between the two voltage leads, the Hall voltage is zero so as to the Hall resistance. When the field keeps increasing, the domain wall will remain between the two leads. Thus the Hall signal will be zero in this range. However, when the field becomes larger, eventually the slanted domain wall will pass both the voltage leads, one can start to observe the anomalous Hall effect again. And when the field is large enough, all the magnetization will flip, reaching saturation. Thus, the potential in the upside becomes positive and downside becomes negative.

To further confirm the slanted domain wall behavior, the anisotropic magnetoresistance (AMR) is measured on the same piece of sample. Current is still sent with the two horizontal leads, labeled by I+ and I- in figure(6.10). Voltage is measured through leads pair 1 & 2 and 3 & 4. When the voltage is measured through 1 & 2, assume the initial voltage is negative when the magnetization reaches saturation. Therefore, the voltage difference is zero between the two leads. When the field is applied in the opposite direction, the slanted domain wall begins to appear from the left side of the sample (where the CoFeB is thinner). At some certain field, the do-

main wall will pass the lead 1, so that the voltage at 1 is positive and voltage at 2 is negative. The difference, $V_1 - V_2$, gives a positive value, thus result in a peak in the measured curve (indicated by the red peak in the purple dashed box). With the field continuing increasing in this direction, the slanted domain wall will keep moving. If the domain wall passes through both 1 and 2, the voltage at both location becomes positive, giving a zero signal again.

When the signal is measured through leads 3 and 4, it is slightly different. Initially, the case is similar with the previous measurements, with both leads carrying a positive voltage and a zero voltage difference. When the slanted domain wall appears due to the application of opposite field, it passes lead 3 ahead of 4, making the voltage at 3 a negative value. So $V_3 - V_4$ is a negative value, which gives a dip in the black curve. When the slanted domain wall pass though both leads, the voltage at those locations become negative, resulting in a horizontal line in the result. More importantly, the peak in the red curve and the dip in the black curve (in the purple dashed box) appears at different location. This does confirm that this behavior is due to the slanted domain wall because the wall will pass the voltage leads at different side of the sample under different magnetic field. When the field is scanned in the opposite direction, it results in a dip in the red curve and the peak in the black curve. Again, the peak and dip appear at different location, which further confirms the existence of the slanted domain wall inside the CoFeB layer.

Moreover, the slanted domain wall has a thickness dependence. The results in figure6.8 show that when the thickness of CoFeB is too thin or too thick, the PMA is not as good as that in the samples with CoFeB thickness around 7 $\mathring{A}$. So when detailed anomalous Hall effect are measured for those samples, the slanted domain wall behavior is not as obvious as that in the ones showing good PMA. From the illustration in figure(6.11), one can see that when the CoFeB layer is thin (#4), the

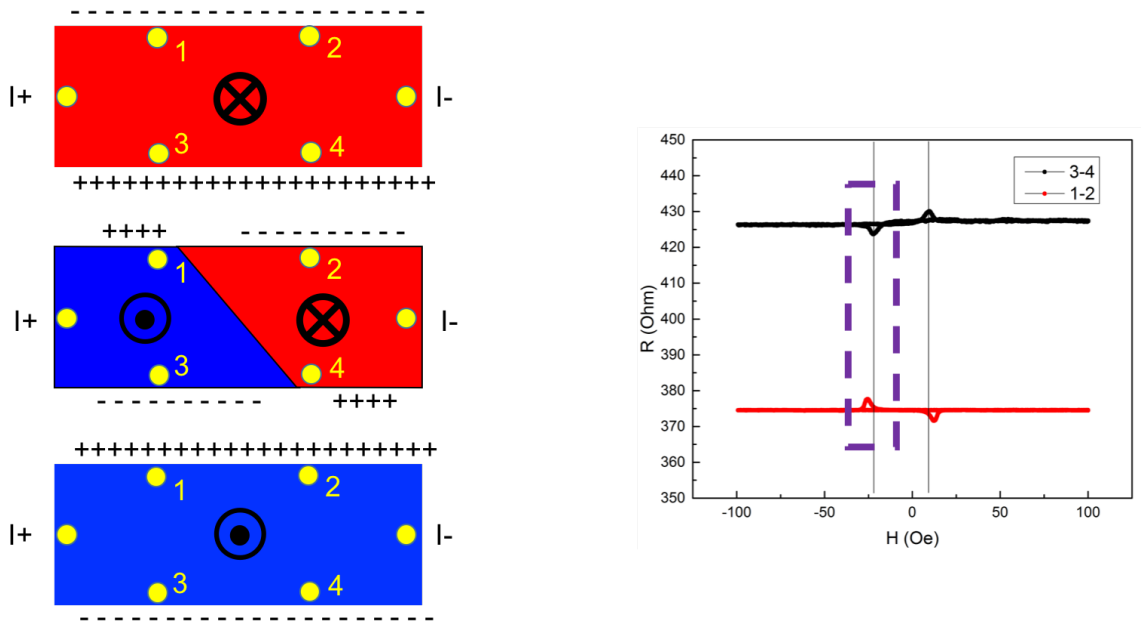

Figure 6.10: Left: Illustration of the AMR measurement. The two yellow dots labeled by I+ and I- represents the current leads, and the four labeled by 1, 2, 3 and 4 represent the voltage leads. The voltage signal is measured by the potential difference between leads 1 & 2 and 3 & 4. Right: Results of anomalous Hall effect measurements

squareness of the loop is not good and the coercivity is small. So the zero Hall step is not clear. For samples #6 and #7, the loop shows clear PMA property, and the step in the middle of the loop is quite obvious. And when CoFeB becomes even thicker (#8), the PMA property gradually fades and thus the step vanishes. One possible reason for this thickness dependence is that the domain walls in the good PMA samples are much thinner than that in the non PMA samples. When the domain wall is thin, it is easier for the two voltage leads to fall into two different domains simultaneously when the domain wall is moving by scanning the external field. When the domain wall is thicker, the two voltage leads will fall into a single domain, resulting in just a normal hysteresis loop without any zero Hall step. Even though they can be in two domains, due to the thickness of the domain wall, this split may only last within a small range of magnetic field, which will cause a quite indistinct step in the loop.

This slanted domain wall behavior can be used to fabricate new domain wall based spintronics devices. One of the outstanding property of it is the possible infinite MR ratio. The magnetoresistance (MR) ratio is calculated by:

$$MR(\%) = \frac{R_s - R_0}{R_0} \tag{6.20}$$

where R_s represents the resistance at saturation and R_0 represents the resistance at the zero Hall step. From the previous data, $R_0 = 0$ when the slanted domain wall lies in between the two voltage leads, making the MR ratio infinite. More importantly, the zero Hall step exists in a range of magnetic field, which makes it possible to fabricate any devices that requires very high MR ratio.

Besides, this structure also indicates the single domain behavior in the CoFeB layer. The movement of domain wall is controlled by apply external field, and can be monitored by measuring the Hall resistance. This makes it possible to integrate this structure in the domain wall spintronics logical devices.

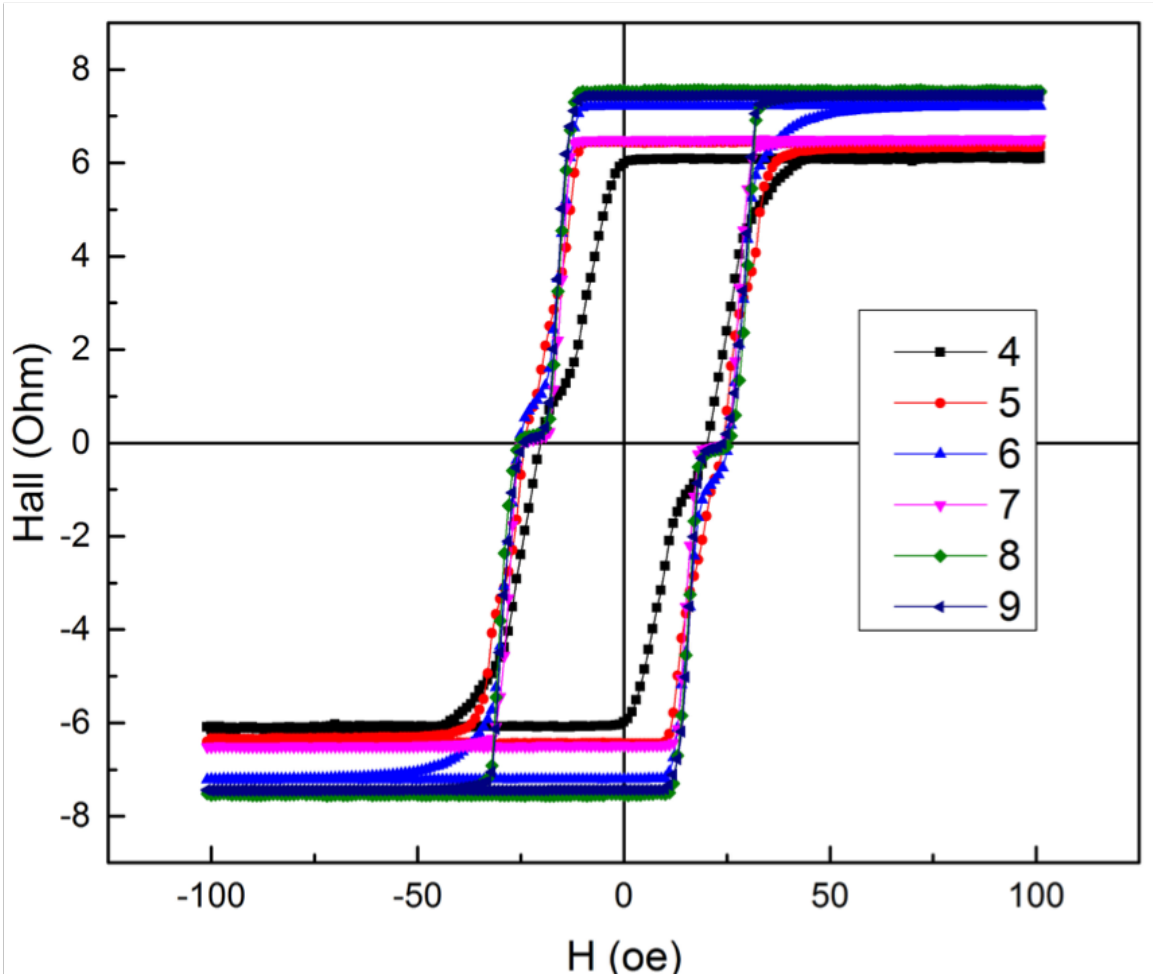

Figure 6.11: The number in the legend represents the thickness of the CoFeB layer. For the #4, #5 and #8curve, the magnetization is not quite perpendicular, which barely shows any zero Hall step in the loop. And very clear step can be observed for #6 and #7 samples, in which very good PMA can be achieved.

In conclusion, perpendicular magnetic anisotropy is successfully achieved in the sample Ta/CoFeB/MgO. Results show that the PMA is quite sensitive to the thickness of the CoFeB. Besides, detailed anomalous Hall effect measurements show that there exists a zero Hall step in the middle of the hysteresis loop, which results from the slanted domain wall movement inside the CoFeB layer. And this zero Hall step has a thickness dependence of the CoFeB layer, which may caused by the wall thickness differences in the PMA sample and non PMA sample.

6.4 Acknowledgement

This work was supported as part of SHINES, an EFRC center funded by the U. S. Department of Energy, Office of Science, Basic Energy Science, under award SC0012670.

Chapter 7

TRIPLET SUPERCONDUCTIVITY

7.1 Motivation

Since the discovery of superconductivity in 1911, much effort has been put in this area to find more superconductors. Superconductivity has been detected in many materials when the temperature is sufficient low. Usually, the highest critical temperature (T_c) for metals in the periodic table is usually about a few Kevin, while some material can only show superconductivity under high pressure. For example, Si will become superconductor when the pressure is about $15GPa$ and $T_c = 8.2K$[82]. To put the superconductor materials in applications, a higher T_c is preferred. During the last few decades, much effort has been put in searching for high T_c superconductor (HTS). In 1986, J. Georg Bednorz and K. Alex Muller, at IBM, discovered superconductivity in a new ceramics materials, which awarded them with the 1987 Nobel Physics Prize[83]. The proposed material was a barium doped compound of Lanthanum and copper oxide, which had a $T_c = 35K$. Currently, the SC with highest T_c is the mercury barium calcium copper oxide ($HgBa_2Ca_2Cu_3O_8$), with T_c about 133K[84].

Besides T_c, the spin in the SC has also attracted a lot of attention, especially after the proposal of BCS theory. The spin configuration in one Cooper pair is of great interest. According to quantum theory, two electrons can not occupy the same quantum state since they are Fermions. Therefore, the total wave function for the Cooper pair should be antisymmetry: if the spatial symmetry is odd, the spin symmetry should be even; if the spatial symmetry is even, the spin symmetry should

be odd. As a consequence, superconductivity can be classified into two categories: spin-singlet and spin-triplet.

Up to today, almost all the superconductors are s-wave SC with an isotropic superconducting gap[29]. All the high T_c cuprates are d-wave SCs with an anisotropic gap structure with nodes and knobs, due to an intriguing and still unknown pairing mechanism[85]. The Fe pnictide SCs, which were suspected to be d-wave SCs, were proved to be s-wave[86], even though the two spins follows an unconventional s_{pm} pairing. The p-wave SCs were predicted in the BCS theory in 1950s[29]. However, little experimental confirmation have been made about that category[87–89]. Currently, only the superfluid He^3 is proved to have triplet spin pairing[90–92]. The searching for solid states p-wave pairing is still one of the most challenging research topics. Over the years, there have been several SCs that were predicted or suspected to be triplet, including the heavy fermion such as UPt_3[93–97], some SC without inversion symmetry[98, 99], ferromagnetic proximity effect induced triplet spin pairing[100], and Fe-SC[101] etc. Experimentally, triplet SC exhibit similar properties as those of singlet SC, such as sudden drop of resistance, Meissner effect and so on. Therefore, distinguishing triplet SC from singlet SC is a tough job and requires specific technique. One of these few complex experiments is the nuclear magnetic resonance (NMR) Knight shift[102] and phase sensitive methods with sophisticated data analysis method[103]. So far, the strongest triplet SC candidate may be the layered perovskite Sr_2RuO_4[87–89]. However, this material has a quite low T_c, which is below 1K. On the other hand, the fabrication of high quality superconducting thin film also prevents people from getting solid experimental confirmation of the spin pairing configuration.

Triplet SCs can offer insight for understanding unconventional superconductivity and new applications in quantum computing[104, 105]. Additionally, the supercurrent in triplet SC can be a super spin polarized current, which carries spin angular mo-

mentum without causing Joule heating, so that it can greatly benefit the development of new spintronics devices[104]. Therefore, it is of great importance to experimentally confirm the existence of triplet SC.

7.2 Singlet and Triplet Superconductivity

As is discussed in Chapter 3, the two electrons in one Cooper pair have a weak attraction through the electron-phonon interaction. In quantum theory, suppose the two electrons interact with each other through the potential $V(\mathbf{r}_1-\mathbf{r}_2)$, which is independent of the spins and other electrons below the Fermi level, then the Schrodinger equation can be written as[106]:

$$-\frac{\hbar^2}{2m}(\nabla_1^2+\nabla_2^2)\psi(\mathbf{r}_1-\mathbf{r}_2)+V(\mathbf{r}_1-\mathbf{r}_2)\psi(\mathbf{r}_1-\mathbf{r}_2)=(\triangle+\frac{\hbar^2k_F^2}{m})\psi(\mathbf{r}_1-\mathbf{r}_2) \quad (7.1)$$

where $\triangle$ is the energy difference between the Cooper pair and two independent electrons.

Consider the center of mass of the two electron, $\mathbf{R}=\frac{\mathbf{r}_1+\mathbf{r}_2}{2}$, and the relative motion of the two electron is $\mathbf{r}=\mathbf{r}_1-\mathbf{r}_2$, then equation can be written as[106]:

$$-\frac{\hbar^2}{m}\frac{\partial^2\psi(\mathbf{r})}{\partial\mathbf{r}^2}+V(\mathbf{r})\psi(\mathbf{r})=(\triangle+\frac{\hbar^2k_F^2}{m})\psi(\mathbf{r}) \quad (7.2)$$

In momentum space, the wave function can be calculated by[106]:

$$g(\mathbf{k})=\int d^3re^{-i\mathbf{k}\cdot\mathbf{r}}\psi(\mathbf{r}) \quad (7.3)$$

Therefore, the wave function in the momentum space is:

$$\frac{\hbar^2}{m}k^2g(\mathbf{k})+\int\frac{d^3k'}{8\pi^3}V(\mathbf{k}-\mathbf{k}')g(k')=(\triangle+\frac{\hbar^2k_F^2}{m})g(\mathbf{k}) \quad (7.4)$$

On the other hand, the interaction between the two electrons in the momentum space can be calculated by:

$$V(\mathbf{k}-\mathbf{k}^{'}) = \int d^3 r e^{-i(k-k^{'})r} V(\mathbf{r}) \tag{7.5}$$

The wave vector, $\mathbf{k}$, also depends on the direction:

$$V(\mathbf{k}-\mathbf{k}^{'}) = \sum_{l=0}^{\infty} V_l(k,k^{'}) \sum_{m=-l}^{l} Y_{lm}(\widehat{k} Y_{ml}^{*}(\widehat{k^{'}})) \tag{7.6}$$

where $Y_{lm}(\widehat{k})$ are the spherical harmonics, l is the orbital angular momentum and m is the z-projection of l.

The weak attraction between the two electrons in the Cooper pair is supposed to happen in a thin layer on the Fermi surface, with a thickness about $\varepsilon_l \ll \varepsilon_F = \frac{\hbar^2 k_F^2}{2m}$. Therefore, the potential becomes[106]:

$$V_l(k,k^{'}) = \begin{cases} -V_l, for\ \varepsilon_F < \frac{\hbar^2 k^2}{2m}, \frac{\hbar^2 K^{'2}}{2m} < \varepsilon_F + \varepsilon_l \\ 0, outside\ the\ interval(\varepsilon_F, \varepsilon_F + \varepsilon_l) \end{cases} \tag{7.7}$$

Solve the Schrodinger equation, one can find:

$$\triangle_l = 2\varepsilon_l e^{-\frac{2}{N_0 V_l}} \tag{7.8}$$

where $N_0 = \frac{m k_F}{2\pi^2 \hbar^2}$ is the density of states at the Fermi level for one spin projection. This equation means that the weak interaction between the two electrons induces a bound state with an energy related to the orbital angular momentum.

Besides, the superconducting states in the momentum space is:

$$g_l(\mathbf{k}) = \sum_{m=-l}^{l} a_{lm}(k) Y_{lm}(\widehat{k}) \tag{7.9}$$

For a given angular momentum l with different coefficient $a_{lm}(k)$, the critical temperature is the same. On the other hand, the orbital wavefunction, $g(\mathbf{k})$, is even when the values of l are even and odd for odd l:

$$g_l(\mathbf{k}) = (-1)^l g_l(\mathbf{k}) \tag{7.10}$$

The spin wavefunction can be expressed with χ_{12}, with the subscription representing the spin component of the two electrons. Therefore, according to Pauli's exclusion principle, the total wavefunction should be antisymmetry:

$$g_l(\mathbf{k})\chi_{21} = -g_l(\mathbf{k})\chi_{12} \tag{7.11}$$

Use $|\uparrow>$ to represent spin up electron and $|\downarrow>$ for spin down electron. If, in one Cooper pair, the two electrons have antiparallel spin, the total spin angular momentum, $S = 0$. Therefore, the wave function corresponds to one spin projection:

$$S_z = \frac{1}{\sqrt{2}}(|\uparrow\downarrow> - |\downarrow\uparrow>) \tag{7.12}$$

The superconductors with this kind of spin configuration are called singlet superconductors.

On the other hand, the spin may occupies triplet states (S=1). In this case, there are in total three spin projection on the quantization axis, namely:

$$S_z = \begin{cases} 1, |\uparrow\uparrow> \\ 0, \frac{1}{\sqrt{2}}(|\uparrow\downarrow> + |\downarrow\uparrow>) \\ -1, |\downarrow\downarrow> \end{cases} \tag{7.13}$$

In this case, the superconductors are called triplet superconductors.

Generally, the total orbital angular momentum number, L, can be any integer. When $L = 1, 3, 5...$, the superconductors are triplet, and corresponding to p-wave, f-wave etc. When $L = 0, 2, 4...$, the superconductors are singlet called s-wave, d-wave etc.

For p-wave SC, the two spins can be aligned parallel, which is similar to ferromagnetism. However, usually, superconductivity and ferromagnetism are not compatible. Superconductors have Meissner effect, which expel all the magnetic flux out of them when the applied field is below critical field. Therefore, the discovery of p-wave superconductivity is difficulty. On the other hand, even if there exists any triplet SC, it is quite difficult to distinguish them from singlet SC, experimentally, because the detection of spin pairing configuration in SC is not a trivial task.

7.3 Andreev Reflection for Different Superconductivity

To distinguish triplet SC from singlet, Andreev Reflection Spectroscopy (ARS) is used. As was discussed in Chapter 4, ARS is a powerful method to study both SC and magnetic materials. The results of ARS measurements are based on the superconducting band structure and the non-SC metal used.

Figure(7.1) shows the difference between the triplet and singlet SC when measured with ARS. For singlet SC, the two electrons in the Cooper have to be aligned antiparallel. Therefore, when a non-magnetic normal metal is used to make point contact on the SC, and one electron is sent into the metal, this electron will couple with another electron, form a Cooper pair, and go into the SC. Therefore, one electro is sent in and two electrons are detected so that the differential conductance will be doubled, compared with the value outside the superconductor gap. However, if the non-magnetic metal is replaced by a half metal, the result is quite different. In half metal, there is only one spin band available. Therefore, when an electron is sent into the half metal,

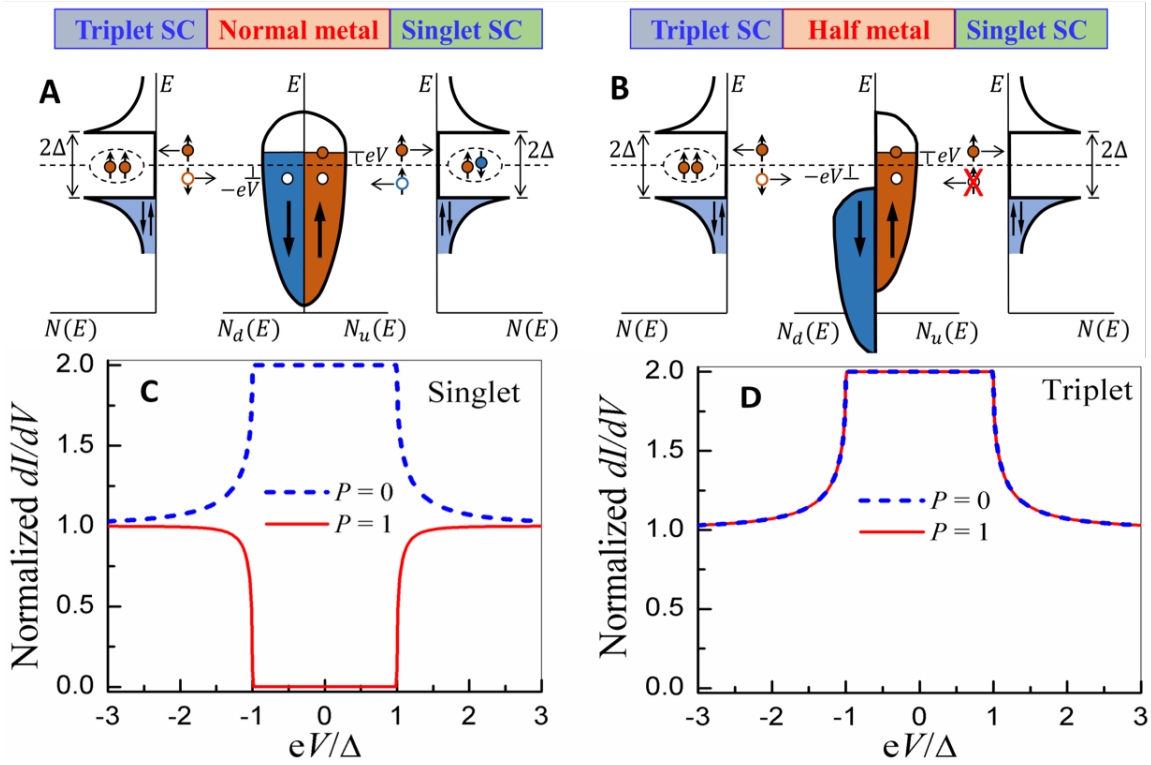

Figure 7.1: A: Andreev Reflection measurements for triplet and singlet SC with non magnetic normal metal. B: Andreev Reflection measurements for triplet and singlet SC with half metal. C & D: AR results for singlet and triplet SC, respectively. Dash line: Measurements with non magnetic normal metal; Red solid line: measurements with half metal.

this electron can not find a another electron with opposite spin. Thus, no Cooper pair can be formed and the differential conductance will drop to zero. However, it is quite different for triplet SC. When a non-magnetic normal metal is used to make a point contact on the triplet SC, and one electron is sent into the metal, this electron can find another electro and form a Cooper pair. So the differential conductance will double. On the other hand, when a half metal is used to make point contact, since the two electrons in one Cooper can have parallel spin, thus, a coming electron still can find another electron with proper spin, either parallel or antiparallel, and go into the SC side. As a consequence, the differential conductance still will double. This is the crucial difference between singlet and triplet SC when conducting the Andreev Reflection measurement. By observing the changing in differential conductance, one can easily distinguish triplet SC from singlet SC.

7.4 p-wave Candidate: Bi/Ni Bilayer

Bi is a non-superconducting semi metal in its thermodynamically stable rhombohedra structure, which is shown in figure(7.2(a)). On the other hand, Ni is a ferromagnetic material, which is non superconducting. However, after a 3 nm Ni is deposited on 20 nm Bi, a superconductivity behavior can be observed when the temperature is below 4K (inset of figure(7.2(a))). In this structure, Ni still remains ferromagnetism at room temperature (figure(7.2(b))). The incompatibility of ferromagnetism and SC indicating that this is the most dramatic nucleation of SC, with a non superconducting material become superconductor when covered by a layer of ferromagnet.

The crystal structure of the sample can be detected by RHEED and cross section scanning transmission electron microscopy (STEM). The bilayer structure is deposited on a MgO(001) substrate. A 3 nm Ni(001) layer is first epitaxially deposited on the

substrate at room temperature, and then the system is cooled down to 110K, with a 20 nm rhombohedra Bi(110) layer deposited on top afterwords. Figure(7.2(c)) shows the results of RHEED and STEM measurement, which reveals a high quality sharp interface. On the other hand, the appearance of superconductivity does not depend on the growth sequence. As comparison, when a 20 nm Bi layer is deposited on the MgO substrate first, and then a 3 nm Ni layer is deposited on top of the Bi, superconductivity can still be observed, as is shown in figure(**??**(d)). Again, this superconductivity does not affect the magnetism of Ni under room temperature (7.2(e)). However, the combination of the bilayer structure is of great importance. The orange dots in figure(7.2(e)) shows that when a layer of 20 nm Bi is deposited on a thin layer of Cu, there is no superconductivity. However, when the Bi/Ni bilayer is deposited on top of a Cu thin layer, the superconductivity comes back[107].

More interestingly, the superconductivity of the bilayer structure heavily depends on the thickness of both Bi and Ni layer. For a fixed thickness of Bi, e.g., 20 nm, a Ni layer with increasing thickness always decimates superconductivity. For $t_{Ni} = 2nm$, T_c is about 4 K but reduced to 2 K for t_{Ni}=4nm. This is due to the stronger exchange field from a thicker Ni layer. Remarkably, increasing the thickness of the Bi layer can restore the decimated superconductivity and T_c recovers back to about 4 K. Further increasing the Ni layer proceeds to reduce T_c. As a result, there are numerous thickness ranges to explore the unusual and indeed unprecedented superconductivity in epitaxial Bi/Ni, and above all, the observation of p-wave superconductivity.

To further study the superconductivity in epitaxial Bi/Ni, the critical field for the structure Bi(15nm)/Ni(2nm) is measured, for both perpendicular (figure(7.4(A))) and parallel (figure(7.4(B))) to the film plane. To describe the field dependence, we identify from each resistance vs. temperature curve three characteristics temperatures of onset ($0.95R_N$), mid-point ($0.5R_N$) and zero-resistance ($0.05R_N$), where R_N

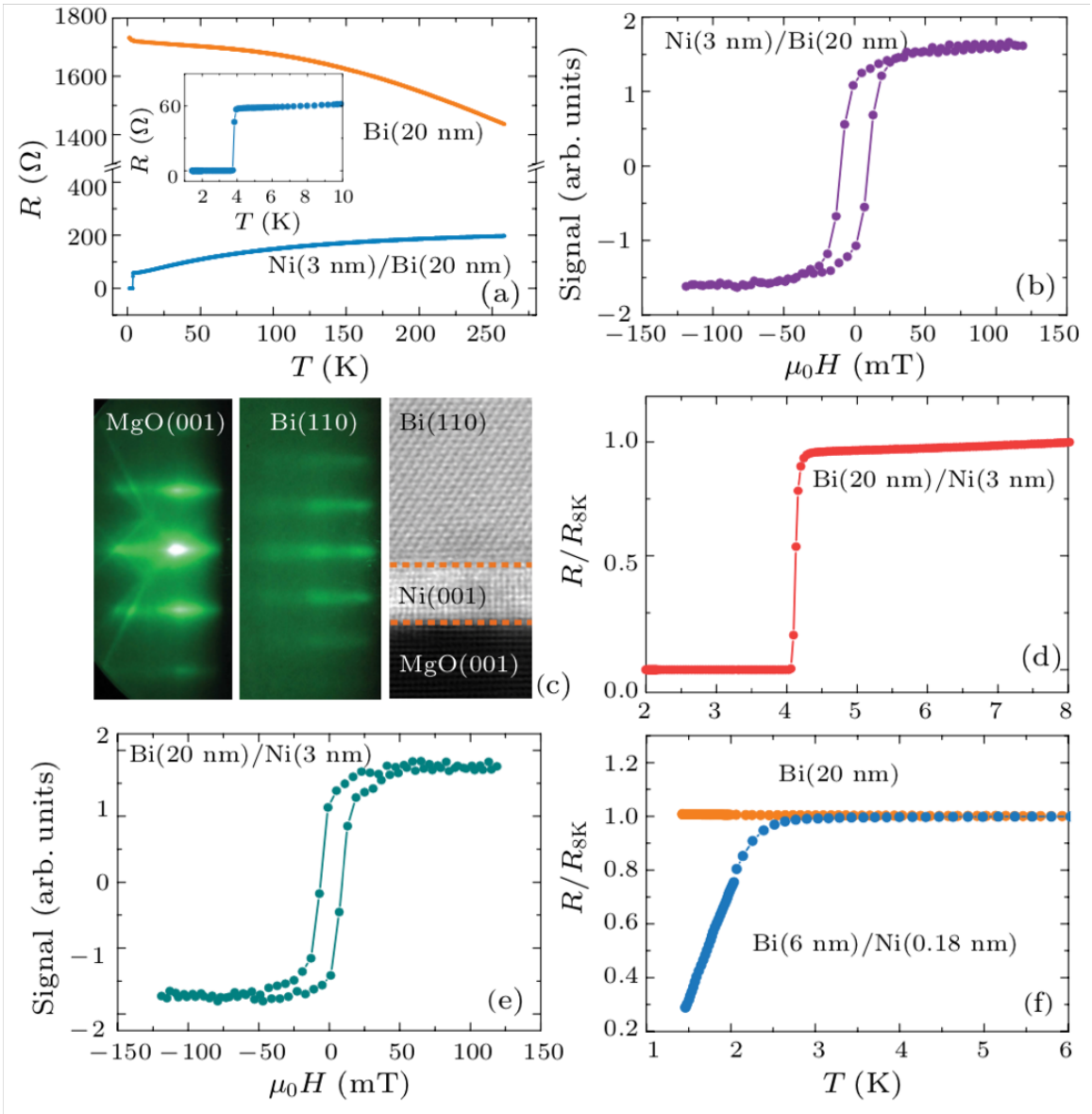

Figure 7.2: A: Single layer of rhombohedra Bi is non-superconducting. Single Ni is non superconducting neither. B: Ni(3nm)/Bi(20nm) shows magnetic property at 300K (MOKE). C: RHEED and cross-section SEM shows good layered structure. D: Bi(20nm)/Ni(3nm) shows superconductivity under 4K. E: Bi(20nm)/Ni(3nm) shows magnetic property at room temperature. F: R-T curves for Bi/Cu/MgO and Bi/Ni/Cu/MgO structures.[107]

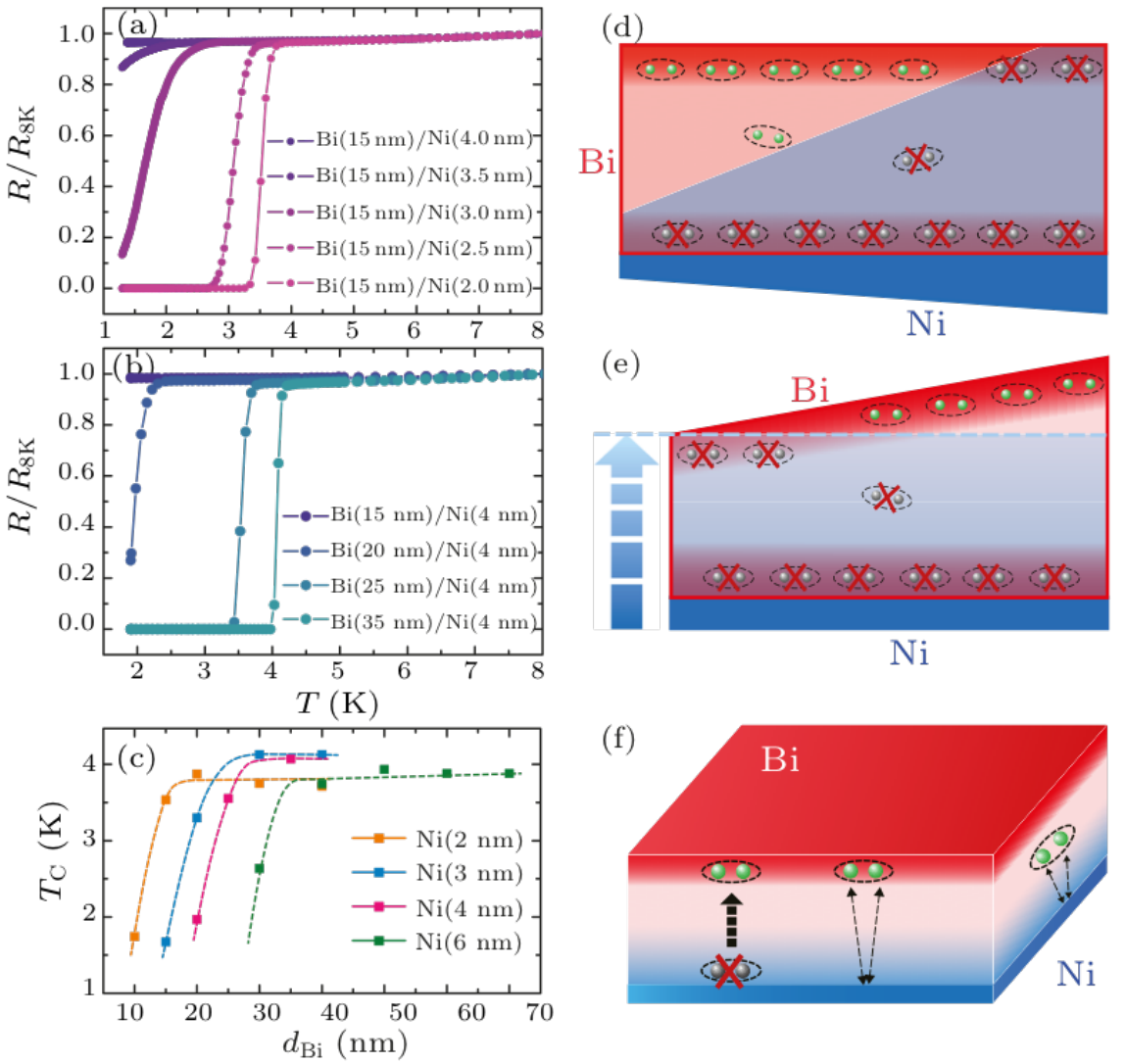

Figure 7.3: (a) and (d): For a fixed Bi layer of 15 nm, the superconductivity appears when Ni layer is thin. When Ni is thicker than 4 nm, the superconductivity is gone. (b) and (e): When Ni is a fixed layer of 4 nm, there is no superconductivity when Bi layer is thin, and appears when Bi layer is thicker than 25 nm. (c) and (f): Thickness dependence of superconductivity on both Bi and Ni layer.[107]

is the normal state resistance. For increasing magnetic fields, the three characteristics temperatures shift to lower values as shown in figure(7.4(C)), which display the temperature dependence of the upper critical fields in the two directions. For the perpendicular field (open symbols), which has a lower upper critical field, the temperature dependence is essentially linear down to 2.0 K. Fitting the results to the Werthamer-Helfand-Hohenberg (WHH) formula of $H_{C2}^{\perp}(0) = 0.69\frac{dH_{C2}^{\perp}}{dT_c}|_{T_c}$[108], the upper critical field at T = 0 K from the zero-resistance data (indicated by the empty blue triangle) is about 1.9 T. For the in-plane field (solid symbols), the upper critical field can be well described by $H_{C2}^{\parallel}(T) = H_{C2}^{\parallel}(0)(1 - T/T_c)^{\alpha}$, but the fitted exponent α is about 2/3, quite different from 1/2 as found in other quasi-2D superconductors[109, 110]. This is illustrated in the onset data (solid purple triangles) in figure(7.4(C)), where $\alpha = 2/3$ (solid purple curve) clearly gives a best fit to the results than that with $\alpha = 1/2$ (dashed purple line). We note in figure(7.4(C)) that the upper critical fields of both directions extrapolated to T = 0 K are substantially above the Pauli limit of $B_{Pauli} = 1.83T_c = 7.1T$ [111, 112], which has been used for the indication of unconventional including p-wave superconductivity[88]. However, conclusive p-wave pairing requires spin injection with energies within the gap. Finally, as expected for quasi-2D superconductors[110, 113], the ratio $H_{C2}^{\parallel}/H_{C2}^{\perp}$ of epitaxial Bi/Ni diverges when the temperature approaches T_c as shown in the inset of figure(7.4(C))[107].

To further study the spin pairing in the Cooper pair of Bi/Ni structure, Andreev Reflection Spectroscopy with Au and LSMO tips have been used. As is discussed above, the increasing or decreasing of differential conductance in AR measurements corresponds to the different spin pairing configuration in the Cooper pair. Figure (7.5(A)) shows the AR measurements for a s-wave superconductor, Pb. For s-wave SC, the superconducting gap is isotropic. The two spins in one Cooper is antiparallel.

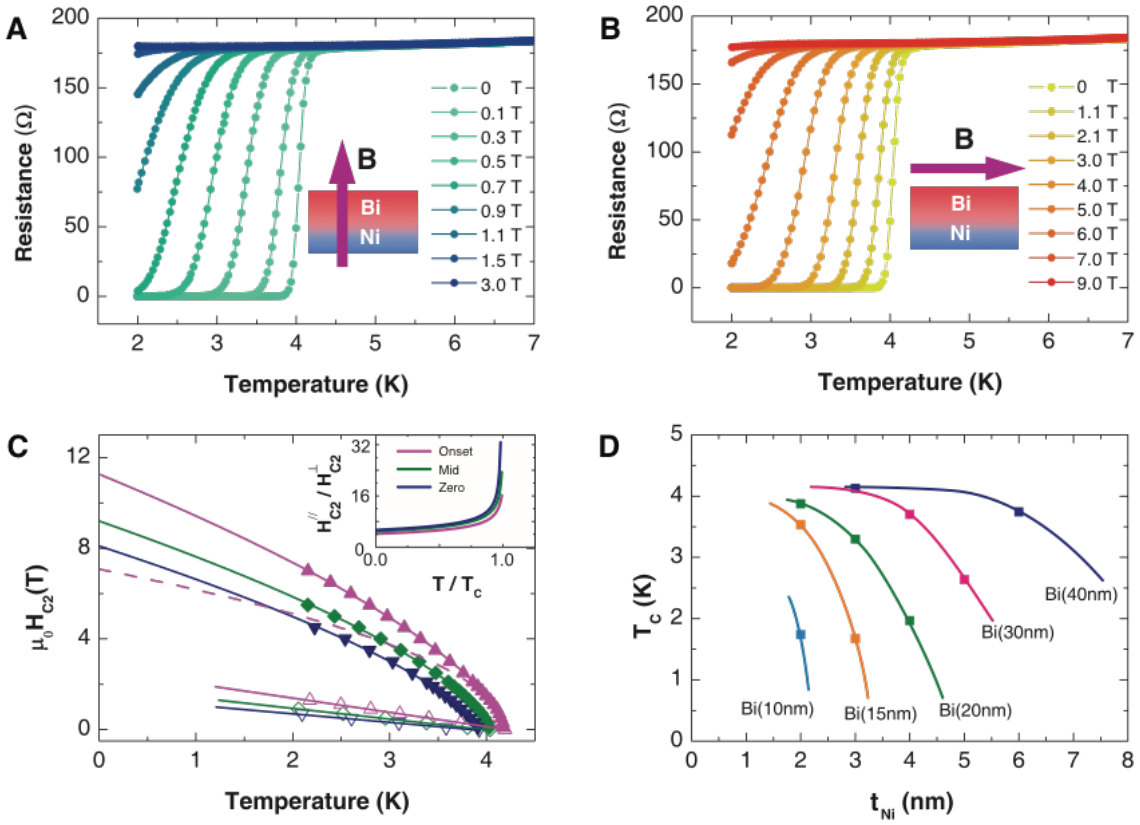

Figure 7.4: Superconducting transition of Bi(15nm)/Ni(2nm)/MgO in (A) perpendicular and (B) in-plane magnetic field. (C) Temperature dependence of upper critical fields H_c for perpendicular (open symbols) and in plane (solid symbols). The solid curves are fittings using $H_{C2}^{\parallel}(T) = H_{C2}^{\parallel}(0)(1 - T/T_c)^{\alpha}$ with $\alpha = 2/3$ and the dashed curve with $\alpha = 1/2$. The divergent nature of the ratio on approaching T_c is shown in the inset (D) Dependence on superconducting transition temperature T_c on Ni thickness for different Bi thicknesses. The lines are guides to the eyes.

Therefore, when a non-magnetic metal, Au, is used to make contact on Pb, the measured differential conductance increases. The ARS results shown in figure(7.1) are for ideal one-dimensional contacts for P = 0 and 1 at T = 0 K. Real contacts usually encounter interfacial scattering and 3D interface, which distorts the ARS results and requires more detailed analyses to extract the gap value. Therefore, it is common to get a double-peak spectrum for a s-wave SC with isotropic gap in AR measurement. On the other hand, when a half metal, LSMO, is used to do the AR measurement, the differential conductance drops, which is also typical for the s-wave superconductor. Another example is for YBCO, a singlet d-wave SC. Generally, a d-wave SC has a four-leaf like gap structure, with nodes and knobs at different location of the gap. The AR results show a peak in the Au-YBCO contact and a dip in the LSMO-YBCO contact, and the single peak of the Andreev bound state results from the nodes in the gap. The solid curves are fitted results using formalism that has been developed [114, 115] and the extracted gap values from Au and LSMO of the same SC are essentially the same. These results show that a highly spin-polarized current can indeed suppress the Andreev conductance. The ARS using both Au and LSMO tips provide unequivocal identification of single SCs, s-wave or d-wave.

However, the AR results show a completely different behavior for the Bi/Ni bilayer. Figure (7.5(C)) shows the AR results when the Au and LSMO are used to make contacts on the top of Bi(110) surface of the Bi(20nm)/Ni(2nm) bilayer. Most remarkably, the ARS using both Au and LSMO are very similar, much larger than 1, as shown in figure (7.5(C)). This indicates that the Bi/Ni cannot sense the spin-polarized current, a defining property of a triplet SC as shown in figure (7.2). To further reveal the nature of the superconductivity in Bi/Ni, some more contacts with various contact resistances on the top of the sample have been measured, as shown in figure (7.6). When the Au tip is contacting on the top surface (figure (7.6(A)),

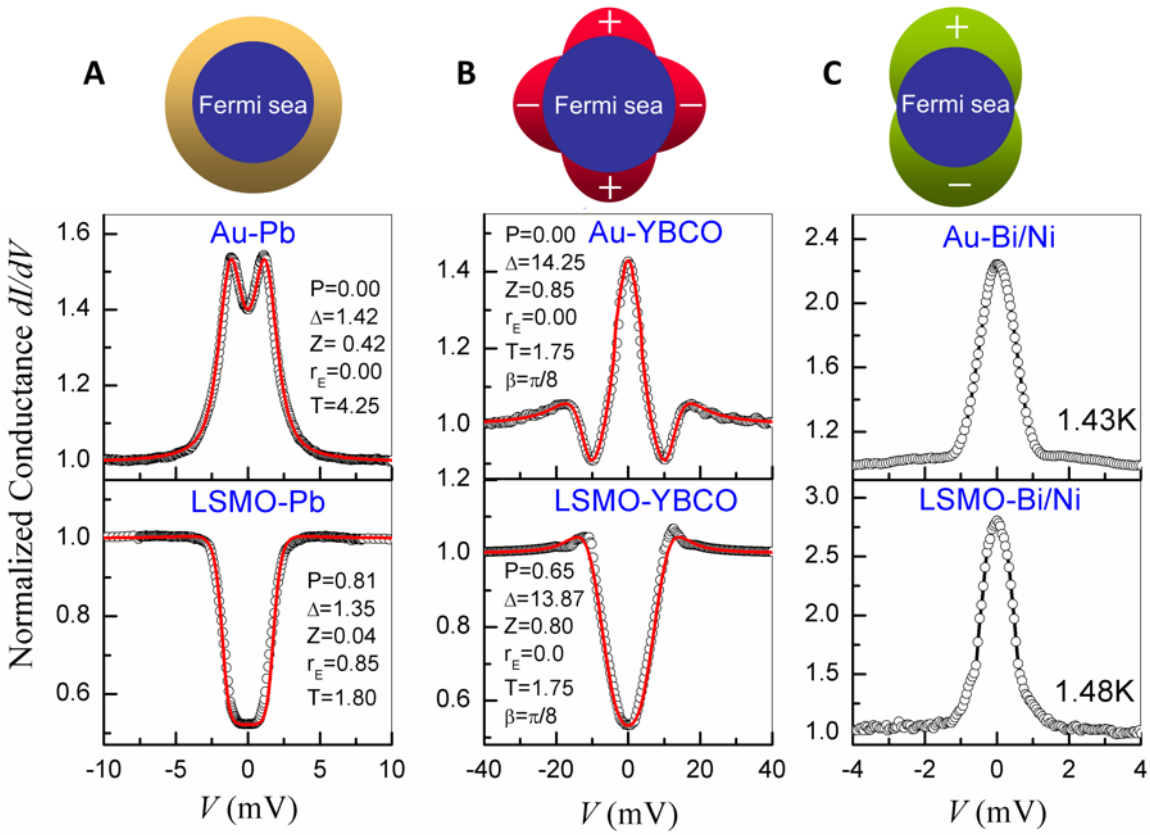

Figure 7.5: (A) Andreev spectra of an s-wave superconductor Pb using Au and LSMO tips. (B) Andreev spectra of a d-wave superconductor YBCO using Au and LSMO tips. (C) Andreev spectra of a p-wave superconductor of Bi/Ni using Au and LSMO tips.

1st row), all the AR spectra with contact resistance from a few Ω to 1700 Ω show the single peak, as shown in the second row of figure (7.6(A)). Importantly, the AR spectra with a LSMO tip also show the single peak from a few Ω to over 1000 Ω, as shown in figure (7.6(A)) 3rd row. This is distinctively different from the AR spectrum of a singlet (s-wave or d-wave) SC in figure (7.5), where the AR peak is suppressed by a spin-polarized current. Taken together, the defining evidences of ARS of Au-Bi/Ni and LSMO-Bi/Ni can only be triplet superconductivity.

The measured conductance ($\frac{dI}{dV}$) in Au-Bi/Ni and LSMO-Bi/Ni for all temperatures are shown in the 3D plots in figure (7.6). The peak structure in both Au-Bi/Ni and LSMO-Bi/Ni varies systematically and disappears at T_c, showing that it is entirely due to superconductivity. At $T < T_c$, the measured $\frac{dI}{dV}$ at bias voltage outside the superconducting gap is roughly constant and it is the normal state conductance ($\frac{dI}{dV}$)normal. As shown in figure (7.6(A)), in both Au-Bi/Ni and LSMO-Bi/Ni, the value of (dI/dV) normal is finite at T = 0 K and approximately unchanged until T_c is approached and then reduces sharply. Concurrently, the peak intensity in Au-Bi/Ni steadily reduces with increasing temperature and vanishes at T_c as shown in figure (7.6(A)). We note similar results of the peak intensity have also been observed in LSMO-Bi/Ni, except that the intensity is not monotonically decreasing, but showing some unusual changes at around 2 K, perhaps related to the superconducting domain structures in the Bi/Ni. These extensive ARS results using both Au and LSMO tips show the peak structure can only be associated with the superconducting state at $T < T_c$. Large differential conductance features for both Au and LSMO tips are the telltale signatures of triplet superconductivity.

Most often ARS is administered on the large top surface of the specimen as in all the cases described thus far. The epitaxial Bi/Ni samples have been cut along different crystal directions thus offering the opportunities to perform ARS measurements on

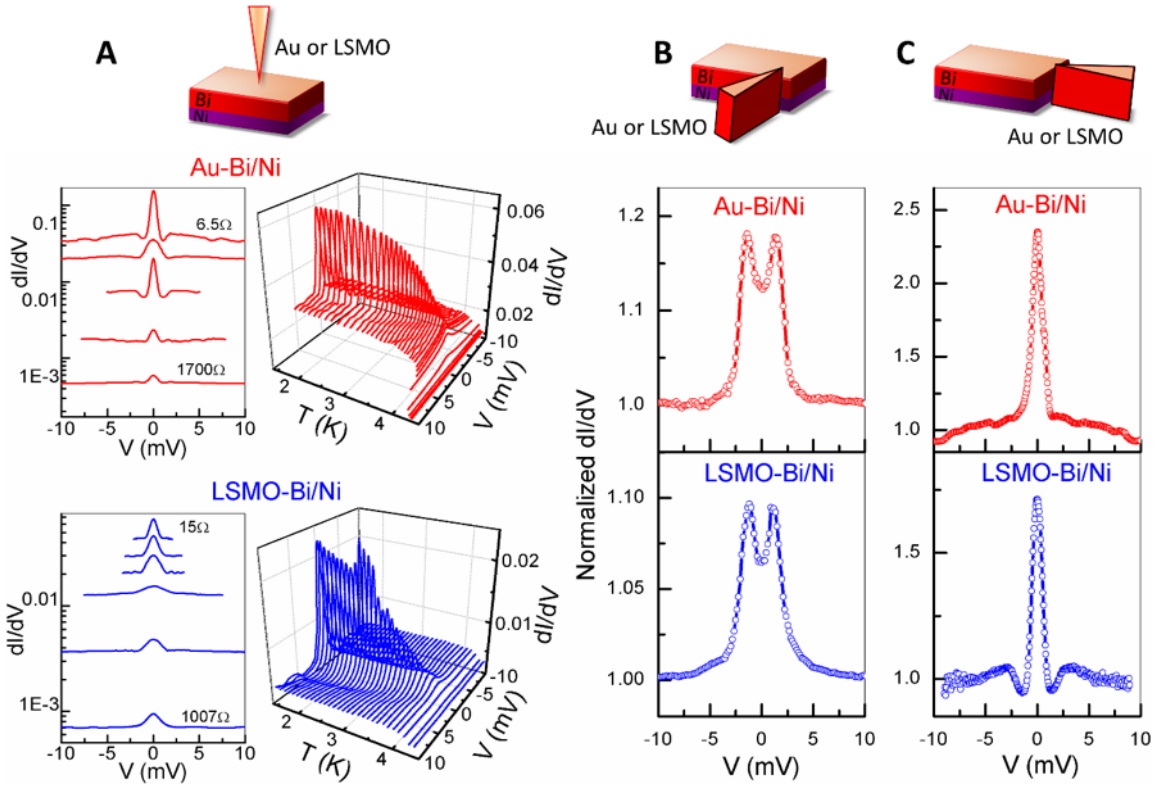

Figure 7.6: (A) Andreev spectra of Au and LSMO contacts on the top surface of Bi/Ni: using Au tip with various contact resistance from a few Ω to 1700 Ω (2nd row left), and temperature dependence of Andreev spectra of one contact using Au tip (2nd row right), Andreev spectra of contacts on the top surface of Bi/Ni using LSMO tip with various contact resistance from 15 Ω to over 1000 Ω, (3rd row left), temperature dependence of Andreev spectrum of a contact using LSMO tip (3rd row right), (B) Andreev spectra of contacts on one side of Bi/Ni: representative Andreev spectra using Au tip, (2nd row) and LSMO (3rd row) tips; (C) Andreev spectra of contacts on the other side of Bi/Ni: representative Andreev spectrum using Au (2nd row) and LSMO (3rd row) tips.

the side surfaces. Au or LSMO is cut into sharp blades in order to make cross-contacts on the sides of the sample, as schematically shown on the top of figure (7.6(B)) and figure (7.6(C)). Since the Bi/Ni sample is only a few tens of nanometers on the insulating substrate MgO, it is exceedingly difficult to create point contact of a few nanometers for ballistic spin injection. Several contacts were successfully made and double-peak AR spectra have been observed for both Au and LSMO on the one side, shown in figure (7.6(B)), and singlet AR spectra on the adjacent side shown in figure (7.6(C)). These are distinctively different from all the AR spectra taken on the top surface as shown in figure (7.6(A)) that always shows a single peak. Importantly, both of the AR spectra, for Au and for LSMO, are similar, regardless of it is double or single peak. Thus these contacts made on the sides of the specimen reaffirm that Bi/Ni is a triplet SC.

Referring to the top of figure (7.5(A)), the p-wave gap structure has nodes. When the contact is right at the knob of the gap structure, the AR shows a double-peak structure while it shows single peaks of Andreev bound states when contact is in the node direction. These distinct features have indeed been observed for AR along the three different directions as shown in figure (7.6(A,B and C)). These results, albeit those with side-contacts are more challenging, conclusively show that Bi/Ni is a p-wave triplet superconductor.

While the mechanism of the superconductivity in Bi/Ni is likely to be a complex one and under further studies, it should be related to the unique properties of the epitaxial Bi and Ni layer where Bi is a semimetal known to have very long mean free path up to cm in bulk Bi[116] and Ni is ferromagnetic. The Bi/Ni bilayer breaks the inversion symmetry and the critical field exceeds the Pauli limit, suggestive of the triplet nature of superconductivity. Our ARS results with a normal and especially half-metallic current unequivocally indicate a p-wave gap symmetry in the Bi/Ni

system. As shown in figure (7.4(D)), superconductivity in epitaxial Bi/Ni occurs in multiple thickness ranges, strongly suggesting that the unconventional superconductivity originates at the Bi/Ni interface. The unusual thickness dependence in Bi/Ni also rules out simple suggestions of superconducting fcc Bi[117, 118] or Bi-Ni alloys at the interface, not to mention that our RHEED measurements during growth show no such evidences at all. It would be very interesting to explore the evolution of the superconducting properties and especially the pairing symmetry as one systematically varies the thicknesses of the two constituent metals. The search for triplet superconductors has been ongoing for more than two decades, but only in bulk materials, such as Sr2RuO4. It is shown in this work that quasi two-dimensional thin films of suitable combination of materials may be more amenable for triplet superconductivity.

7.5 Singlet Superconductivity: Bi_3Ni Compound

In the previous section, the Bi/Ni bilayer structure is proved to be a candidate for p-wave SC using the Andreev Reflection spectroscopy. The interface between the Bi and Ni thin film layer may have great effect on the coexistence of superconductivity and ferromagnetism. Since only in the triplet SC, the two spins in one Cooper pair can be parallel, therefore, ferromagnetism can only coexist with triplet superconductivity, where the supercurrent carries spin angular momentum, similar as that of a spin-polarized current in a ferromagnet.

Since the bilayer structure shows possible p-wave superconductivity, the next question comes to mind is that: is it possible to realize superconductivity, especially triplet superconductivity, in Bi-Ni compound? Coexistence of ferromagnetism and superconductivity has been observed in Bi_3Ni nanostructures[119, 120]. But later experiments did not find ferromagnetism in Bi_3Ni single crystals[121]. In this work, ARS with an unpolarized current has been utilized to determine the gap value, structure and T

dependence of intermetallic SC Bi_3Ni. Furthermore, a highly spin-polarized current injected from $La_{2/3}Sr_{1/3}MnO_3$, (LSMO) has been used to determine spin states. The spin states of the polycrystalline Bi_3Ni sample is antiparallel, the same as that of a singlet SC. The critical field of the sample is about 150 Oe, observed in ARS in a small magnetic field. The point contact shows a negative magnetoresistance (MR) for unpolarized current but a positive MR for a spin-polarized current, demonstrating the distinctive difference of AR for unpolarized and polarized current of a singlet SC. The gap value $2\Delta/k_BT$, symmetry and its T dependence, combined with the spin states show that the bulk Bi_3Ni is a BCS singlet superconductor.

The Bi_3Ni sample is cut into a tip, then enclosed into a vacuum jacket along with a polished Au surface with 99.999% purity or a single crystal LSMO surface. The sample tube is pumped to 10^{-7} Torr then filled with 0.1 Torr of Helium gas. The samples are then cooled down to 4.2 K using liquid helium. Lower temperature is achieved by pumping the sample tube. At desired temperature, a point contact is established by approaching the tip to the surface via a differential screw mechanism. The differential conductance dI/dV and resistance V/I are measured simultaneously using a lock-in method. For a new contact, the Bi_3Ni tip is cut again to obtain a new tip.

First a point contact is established on nonmagnetic Au using the Bi_3Ni tip. A current from Au is unpolarized, the conductance within the gap Δ should be doubled for an ideal interface, regardless of the singlet or triplet nature of the Bi_3Ni sample. But a real interface often has interfacial scattering Z which causes a dip at V = 0. Some representative Andreev spectra are shown in figure(7.7(a-e)). The open circles are the experimental data and the solid circles are the best fit to the modified BTK model. In the fitting, only Δ and Z are varied while T is set as experimental value and P is 0. The data can be well described by the model and the parameters of the best

fit are listed as inset. The conductance rises up to 1.9, very close to an ideal interface with a small Z factor of 0.15, as shown in figure(7.7(a)). For increasing Z factor, the conductance decreases and there is a zero-biased dip appears at large Z factor, as shown in figure(7.7(e)). The ARS spectra are very different for different Z factor, nevertheless the determined Δ values are very similar. It has been measured over 10 spectra using several Bi_3Ni tips and all the determined gap values are similar. The average gap value is $0.62 \pm 0.01meV$, as shown in figure(7.7(f)). The ratio $\frac{2\Delta}{k_BT} = 3.51$, is very close to the BCS s-wave ratio. Since each contact may reach a different crystalline surface of the Bi_3Ni sample, the similar gap value of all contacts indicate an isotropic gap for the Bi_3Ni sample.

After the determination of the gap value and its symmetry using Au with an unpolarized current, next we utilize a highly spin-polarized current to determine the spin states of the Cooper pairs in Bi_3Ni. The polarized current is injected from LSMO, which has a spin polarization of 80% determined by singlet SC Pb[122, 123]. Consider an ideal interface, the conductance at zero-bias voltage G(0) = 2(1-P) = 0.4. Assuming 100 incident electrons, there are 90 spin-up and 10 spin-down electrons. For a singlet SC, 20 electrons have AR: 10 spin-up and 10 spin-down electrons. Each electron with AR reflects a hole, consequently, conductance is 0.4 at zero bias. For a triplet SC, every electron can have AR if it is a mixed of the three spin states, and hence the G(0) = 2. If there is only $S_z = 1$ spin state, then 90 electrons can have AR, G(0) = 1.8. Similarly, G(0)=0.2 for $S_z = -1$ spin state. Therefore, with any combination of the $S_z = 0$ and $S_z = 1$ spin states, the AR spectrum from LSMO will be very different and thus the spin state can be determined.

Some representative ARS spectra from $Bi_3Ni/LSMO$ contact are shown in figure(7.8(a-e)). The open circle are the experimental data and the solid curves are the best fit to the modified BTK model. All the spectra can be well-described by

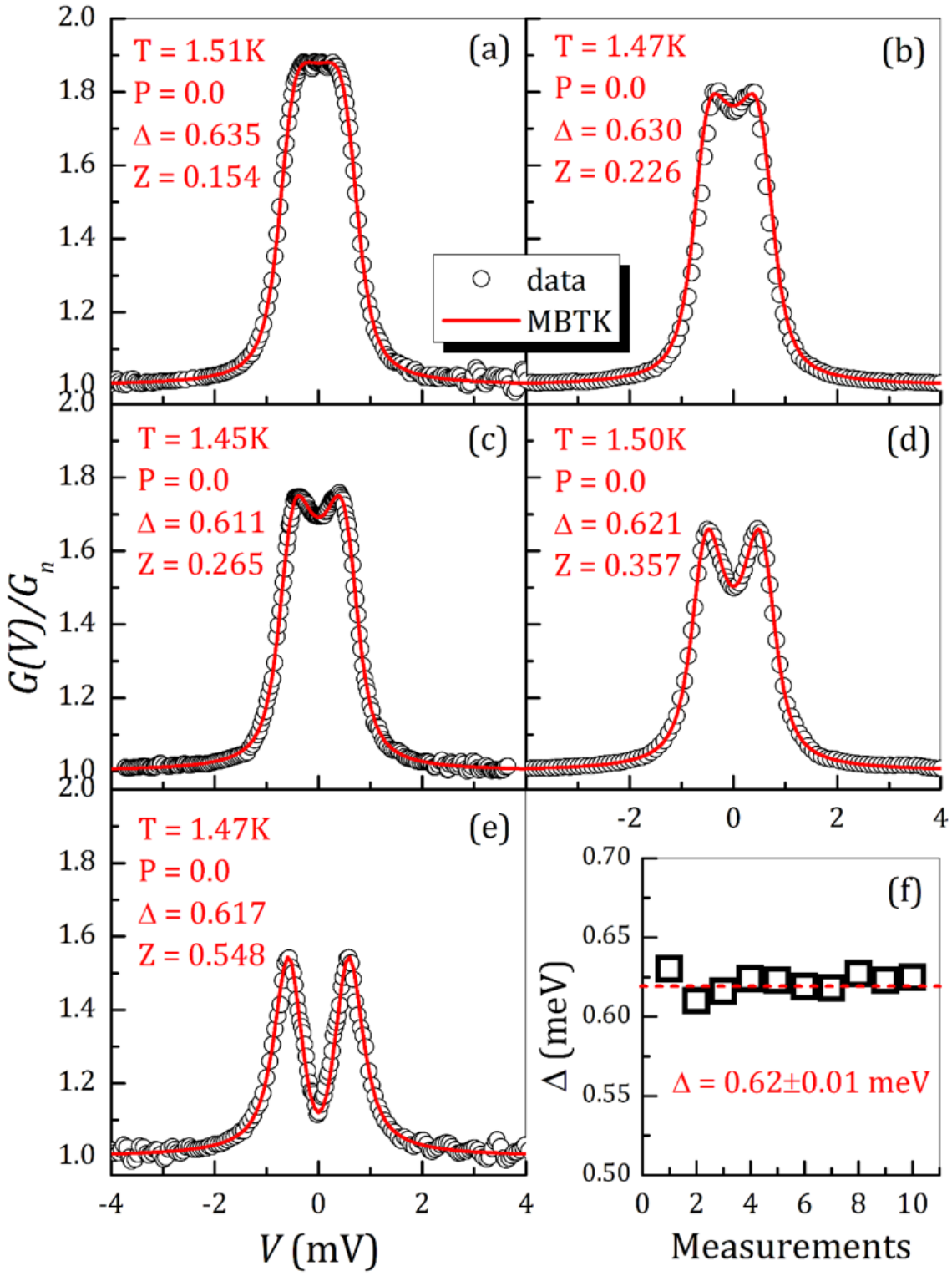

Figure 7.7: (a-e) Representative Andreev spectra of Bi3Ni/Au contacts with various interfacial scattering Z factor (Open circles are the experimental data while the solid curves are the best fit to the modified BTK model), and (f) gap values from different contacts.

the modified BTK model and the parameters of the best fit are listed as inset. In analysis, the gap is fixed as 0.62 meV determined above and T is set as experimental values. Only P, Z and r_E are varied. The extra resistance r_E is utilized to incorporate the effect of the large resistivity of LSMO, and previously it has been discussed in details. The spectra are very different from that of Bi_3Ni/Au contacts in figure(7.7): The conductance at zero bias is much lower than 1 due to the suppression of AR by spin polarization. Indeed, the obtained P value is about 80% at small Z factor, as shown in figure(7.8(a)). For increasing Z factor, the shoulder peaks increase, as shown in figure(7.8(e)). The P values obtained from different contacts are plotted in figure(7.8(f)). For increasing Z, the P value decreases due to spin-flipping scattering. The intrinsic spin polarization of LSMO, $P = 0.812 \pm 0.019$, is obtained by extrapolating Z to 0. The P = 0.81 is the same as that obtained using a singlet SC, suggesting that all spin states in the Bi_3Ni sample is antiparallel, the same as that of a singlet SC.

The critical field of Bi3Ni is small, about 150 Oe[124–129] and this can also be observed in ARS. As shown in figure(7.9), the ARS spectrum of a Bi_3Ni/Au point contact can be well described by the modified BTK model. In this analysis, only T is fixed as experimental value but P, Δ, and Z are varied. The obtained P is zero for gold. Then we apply a magnetic field (H) and measure the magnetoresistance (MR) at small bias of 0.1 mV. As shown in figure(7.9(b)), it shows a negative MR. At $H < 150Oe$, the resistance is smaller, and it jumps to a higher value when the Bi_3Ni sample becomes normal. When the Bi_3Ni sample is superconducting, AR occurs thus conductance is doubled or resistance is reduced by half. One notes that the resistance of the whole Bi_3Ni sample is only about 0.1Ω at room temperature. So the change of the resistance of about 1Ω is mainly due to the disappearance of AR at $H > 150Oe$.

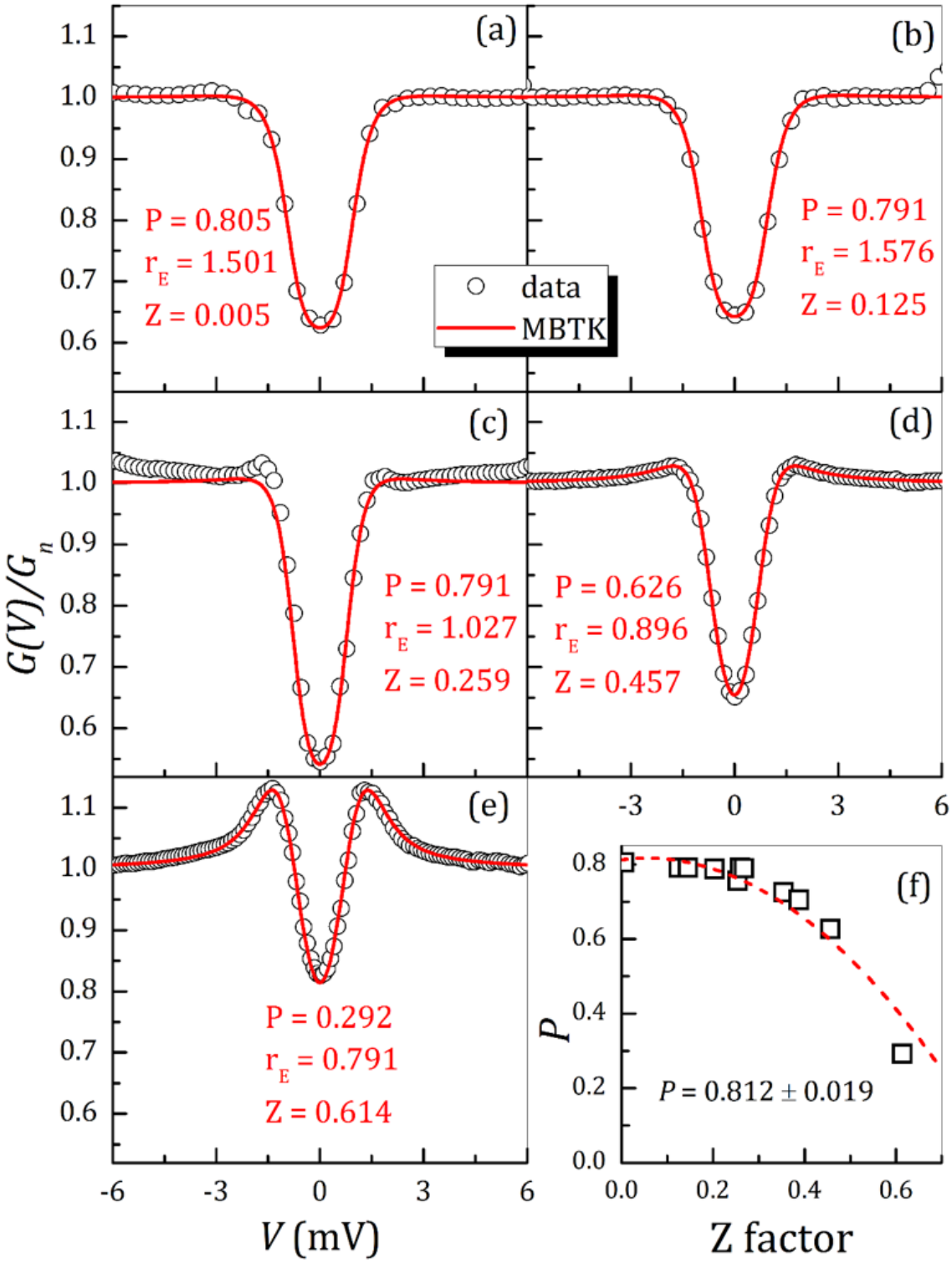

Figure 7.8: (a-e) Representative Andreev spectra of Bi3Ni/LSMO contacts with various interfacial scattering Z factor (Open circles are the experimental data while the sloid curves are the best fit to the modified BTK model), and (f) spin polarization P as a function of Z factor.

For spin-polarized current, however, the MR is completely different. As shown in figure(7.9(c)), the ARS spectrum of a $Bi_3Ni/LSMO$ contact can be well described by the modified BTK model when all the parameter except T are varied in the analysis. The obtained gap value and P values are consistent with the value in figure(7.7) and figure(7.8). The MR at bias V = 0.1 mV is positive, completely different from that observed using the Au contact in figure(7.9(b)). The change of the resistance at H = 150 Oe is about 80Ω, much large than the sample resistance of 0.1Ω. This MR is due to the suppression of AR from the highly spin-polarized current. If it is a true half metal of 100%, the resistance at zero bias would be infinite because of the suppression of AR. In the case of LSMO, the P value is about 80%, but still, the change of resistance is very significant. These results again show that the spin states in the Bi_3Ni sample must be antiparallel.

Next, the temperature (T) dependent of the gap (Δ). As shown in figure(7.10(a)), one AR spectrum is measured from 1.47 K to 4.5K with about 0.2 K of increase for each curve. For increasing T, the AR spectrum decreases and the peak disappears exactly at the T_c of Bi_3Ni at 4.1K. One notes that first it is the Hallmark double AR peaks disappear, and the AR spectrum becomes a big single peak, then the single peak starts to decrease, as clearly shown by the 2D graph in figure(7.10(b)), which is the same data of the 3D graph in figure(7.10(a)). We analyze the AR spectrum at each T. For the spectrum at 1.47 K, we varied the Δ and Z, and set T = 1.47 and P = 0. For higher T, since the Z factor of the same contact is not expected to change during the total change of T less than 3 K, we fix the Z factor as 0.21, only vary the Δ value in analysis of each T. The obtained Δ values at different T is plotted in figure(7.11(b)), along with a BCS theory (dashed curve). One can see that most of the data are very close to the BCS model except a few points near the transition temperature, which may be due to the pressure on the point contact.

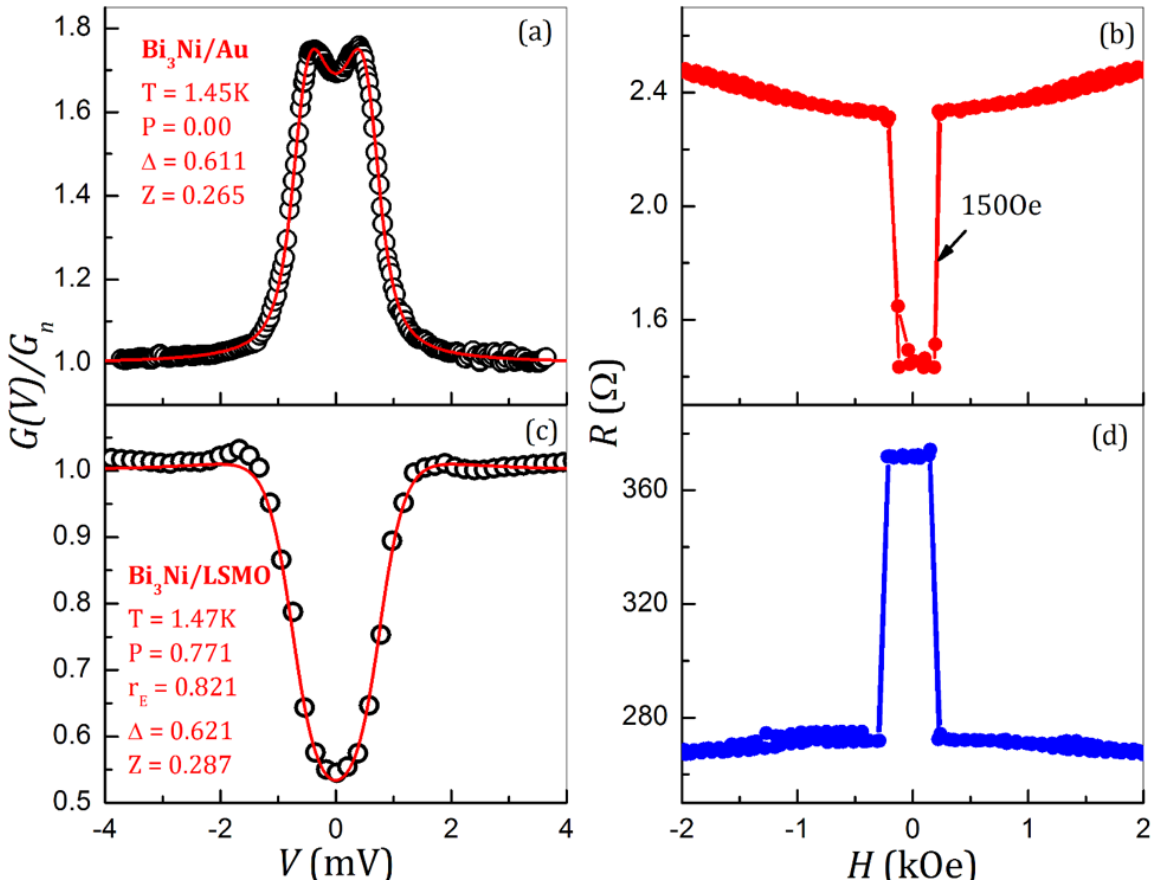

Figure 7.9: (a) Andreev spectrum of one Bi3Ni/Au contact and (b) its magnetoresistance at V 0, Andreev spectrum of one Bi3Ni/LSMO contact and (d) its magnetoresistance at V 0 (open circles are the experimental data and solid curves are the best fit to the modified BTK model with fitting parameters listed inset)

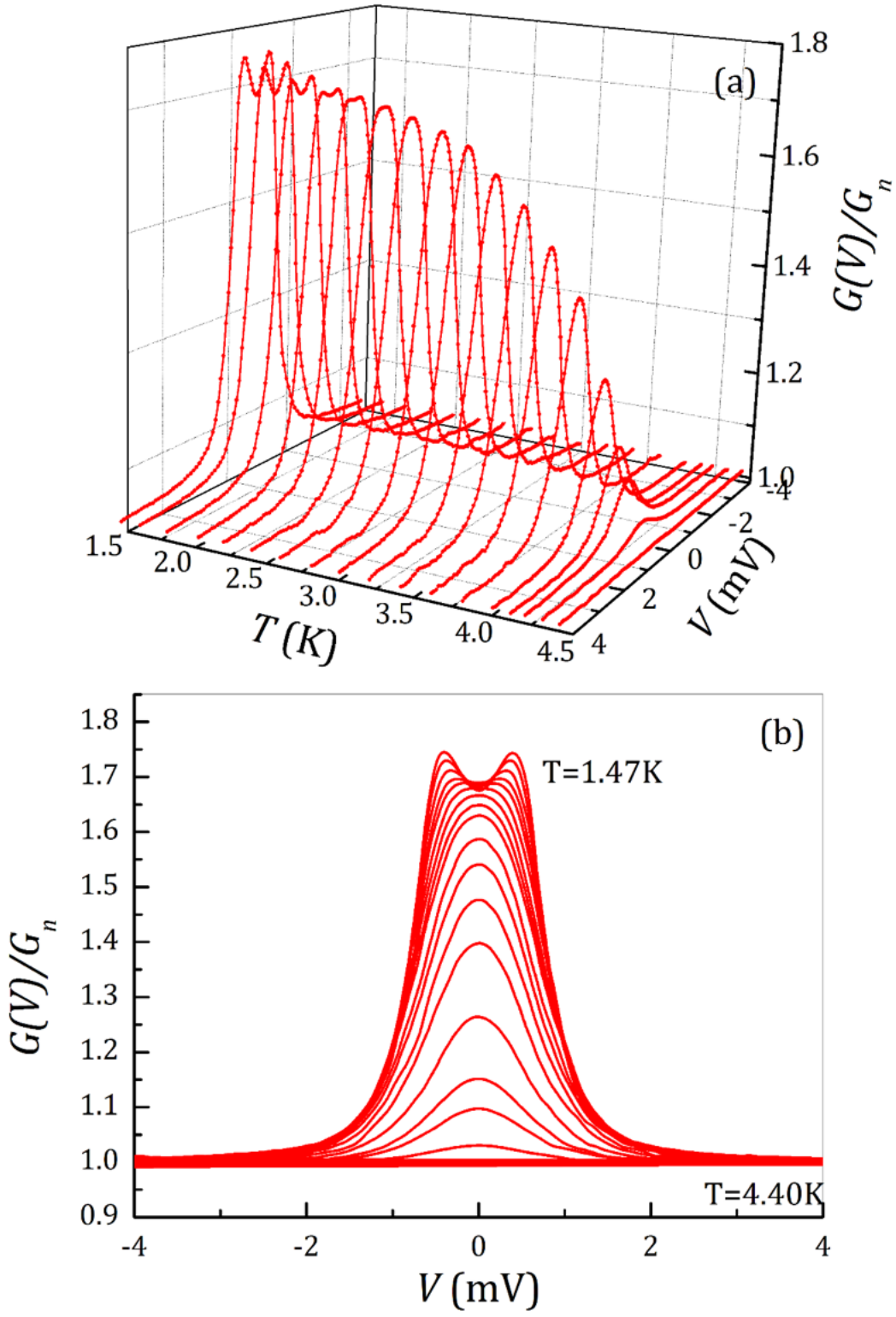

Figure 7.10: (a) 3D plot and (b) 2D plot

Superconductor Bi_3Ni has been studied before. While it has been found that ferromagnetism and superconductivity can coexist in Bi_3Ni nanostructures, ferromagnetism has not been found in bulk single crystals[119, 120, 130–132]. In this work, the gap value and symmetry, spin states and T dependence of the gap all demonstrate that the bulk Bi3Ni sample is a singlet BCS SC. However, this cannot rule out the possibility that triplet superconductivity exists in Bi_3Ni nanostructures. Indeed, studies have shown that while ferromagnetism is absent in the bulk Bi_3Ni single crystal there is ferromagnetism fluctuations at the surface. In the Bi/Ni bilayers or nanostructures, the effect of interface/surface is maximized. Tunneling experiment has shown that the current is spin polarized[133]and recent experiment using ARS has shown that Bi/Ni is indeed triplet[107, 134]. Nevertheless, whenever ferromagnetism or triplet superconductivity shows in Bi_3Ni, the critical field of the structure is much larger 150 Oe, the critical field of bulk Bi_3Ni. Recently it has shown that the superconductivity in 2D materials depends crucially on interface or substrate[135–138]. While a bulk ferromagnetic SC is elusive, our results indicate that the future triplet SC maybe be engineered using hybrid structures, where ferromagnetism can impact superconductivity.

In summary, Andreev reflection spectroscopy with unpolarized and highly spin-polarized currents has been utilized to study intermetallic alloy superconductor Bi_3Ni. The magnetoresistance at zero-bias voltage of unpolarized and spin-polarized current shows that Andreev reflection occurs for unpolarized current but is suppressed by a spin-polarized current. The gap is isotropic with a value of 0.62 meV and $2/k_BT_c = 3.51$. The spin state is antiparallel, the same as that of a singlet superconductor. The temperature dependence of the gap displays a BCS-like behavior. The gap value, isotropic symmetry, and its temperature dependence, along with its antiparallel spin state conclusively demonstrate that the bulk Bi_3Ni sample is a BCS

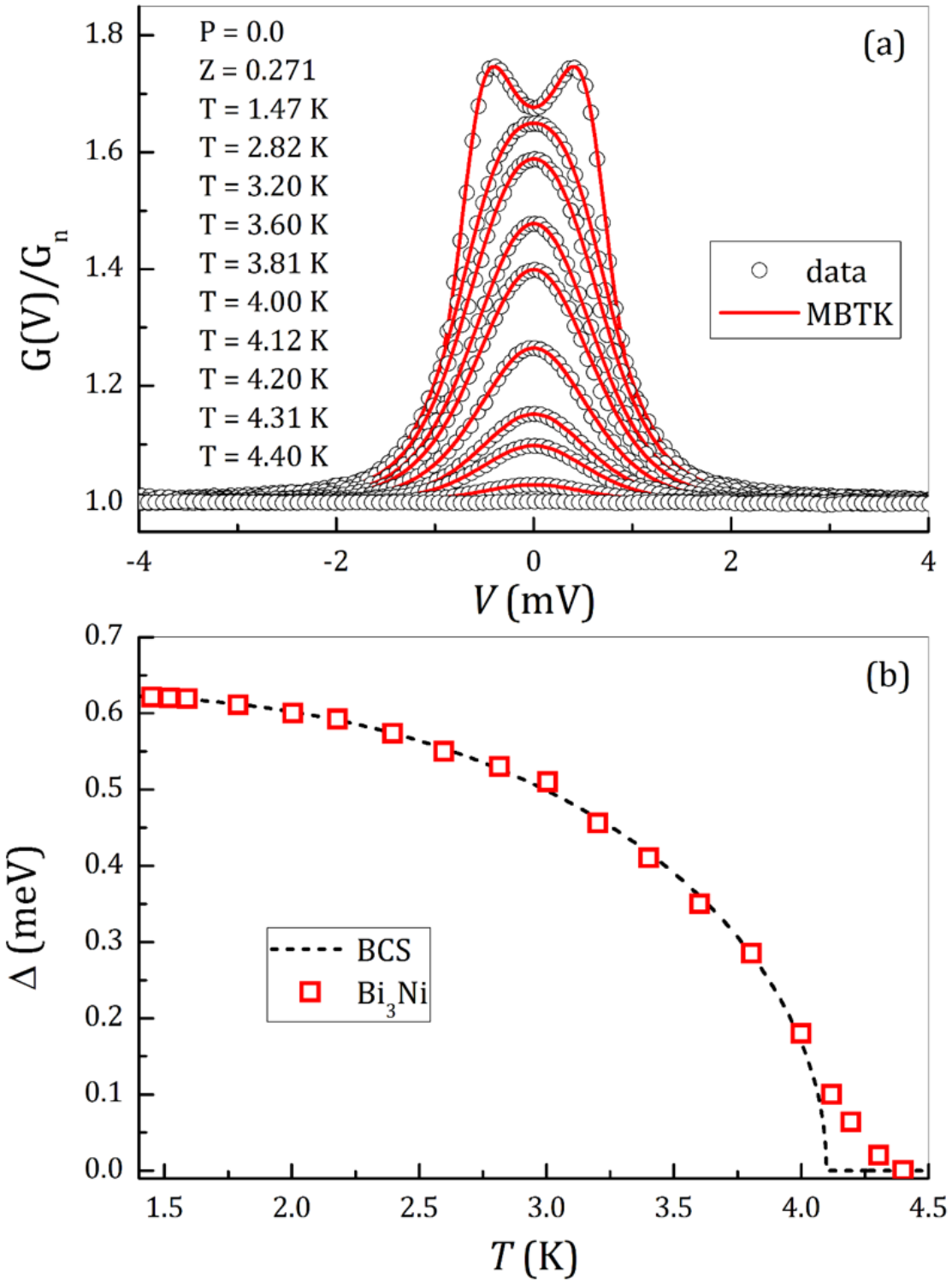

Figure 7.11: (a) Representative Andreev spectra (open circles) and the best fit (solid curves) at different temperatures, and (b) gap values obtained from the best fit at different temperatures from 1.47 K to 4.5 K with Z = 0.271.

s-wave superconductor.

7.6 Acknowledgement

The project is supported by the National Basic Research Program of China under Grant Nos 2015CB921400 and 2011CB921802, the National Natural Science Foundation of China under Grant Nos 11374057, 11434003 and 11421404, the research of Andreev reflection was supported as part of the SHINES, an Energy Frontier Research Center funded by the U.S. Department of Energy, Office of Science under Award SC0012670.

Chapter 8

2-DIMENTIONAL SUPERCONDUCTIVITY

8.1 Motivation

Superconductivity arises from the formation of Cooper pairs at low temperature. In bulk material, the electrons gradually coupled into pairs with proper spin, due to the weak attractive electron-phonon interaction. In thin films, due to the lack of electrons, it becomes harder and harder to form Cooper pairs, so as to induce superconductivity. One extreme is when the thickness of the thin film is thinner than the coherent length of the Cooper pair, the order phase will be destroyed. Historically, due to the symmetry coherence breaking nature of the 2D material, the Mermin-Wager theory prohibits the existence of the 2D superconducting phase[139, 140]. On the other hand, the 2D materials are even not expected to be metals, but insulators, due to the electron localization[141]. Thus, two dimensional (2D) superconductivity seems impossible to realize.

2D material in low temperature can have Berezinskii-Kosterlitz-Thouless (BKT) transition, which is a phase transition from the bound vortex-antivortex pairs to unpaired vortices and antivortices at a certain temperature. This transition is based on a 2D XY model, which is a vector spin model. In this model, the vortices are topologically stable. The energy of a single vortex is $\kappa ln(\frac{R}{a})$, where κ is systematic parameter determined by the vortex system. R and a are the system size and the radius of the vortex core, respectively. Therefore, the number of vortex in a 2D system can be calculated by $(\frac{R}{a})^2$. So the Helmholtz free energy is:

$$F = E - TS = (\kappa - 2k_B T) ln(\frac{R}{a}) \tag{8.1}$$

where k_B is the Boltzmann's constant. When $F < 0$, the system will favor the formation of a vortex. So the critical temperature above which the vortex can form is determined by:

$$T_c = \frac{\kappa}{2k_B} \tag{8.2}$$

This BKT model is compatible with the Mermin-Wager theory, and allows the formation of quasi long range correlation of the order parameter[142, 143]. On the other hand, the BKT transition also causes a zero resistance state, which can be retained for a infinitesimally small external perturbation and the Meissner effect can also be well defined[143–145]. Experimental and theoretical studies show that for 2D materials, the superconductor-insulator (S-I) transition always happens when the sheet resistance of the sample is in the same order of the quantum resistance of the Cooper pairs, namely, $R_Q = \frac{h}{4e^2} = 6.45k\Omega$[146]. In the BKT transition, the sheet resistance induced by the vortex-antivortex pair can be calculated by[143]:

$$R_{sheet} \approx exp[-(\frac{T_{c0} - T}{T - T_{BKT}})^{1/2}] \tag{8.3}$$

where T_{BKT} is the temperature above which the BKT transition can happen. Because there is no free vortex when $T < T_{BKT}$, it is possible to realize zero resistance in this case.

Experimentally, the development of ultrahigh vacuum (UHV) technique has greatly benefited the studies on the ultrathin 2D superconductors, such as molecular beam epitaxy (MBE), pulsed layer deposition (PLD) etc. These technologies allow atomic scale materials to be fabricated. On the other hand, more accurate measurement

method, such as scanning tunneling microscopy (STM), make it possible to characterize the materials in unprecedented details. First experiments on superconducting ultrathin film is a Pb film on a clean Si(111)- (7×7) surface, which was prepared by MBE technique[147]. Another example is $La_{2-x}Sr_xCuO_4$, which is a representative cuprate high T_c superconductor, shows superconductivity at one unit cell (UC) thickness[148]. Furthermore, the interface between two perovskite oxide insulators, $LaAlO_3$ and $SrTiO_3$, shows 2D superconductivity[149]. A recent breakthrough is the field induced 2D superconductivity in some certain insulators, such as $SrTiO3$ and $ZrNCl$, which is realized by the the highly doped field-effect transistors (FET) with an electric-double-layer (EDL) gate[150–152]. On the other hand, with the rapid raising of study on atomic sheets, such as graphene and transition-metal dichalcogenide monolayers, the searching for superconductivity in the related structures attracts a lot of efforts[153, 154]. One of the most surprising findings is the superconductivity in the 1 UC thick FeSe layer epitaxially grown on a $SrTiO_3$ substrate, which has a T_c about 40 to 100K, increasing remarkably from the bulk FeSe (about 8K)[155, 156]. This huge increase in critical temperature suggests a possible way to achieve high T_c superconductivity.

The effect for low dimensionality is the increasing in the fluctuation of the system. Generally, a 2D superconductor often exhibits a decrease in conductivity. ON the other hand, in a 2D system, the conduction electron can also be localized owning to the presence of disorder, which is known as Anderson localization[157]. This localization results in a insulating state, and an S-I transition is expected as the disorder of the system increases. The transition is driven by the suppression of amplitude of the superconducting order parameter, Ψ, or the enhanced fluctuation of the superconducting phase, which will lead to a quantum phase transition at zero temperature[146, 158, 159]. In figure(8.1)[160], the superconductivity in the Bi thin

film is shown. When the thickness of the Bi thin film is between 4.36 $\mathring{A}$ to 72.27 $\mathring{A}$, superconductivity can be observed with the observation of a sharp decrease in the electrical resistance. When the thickness of the Bi film is thinner than the lower value, the system will have more disorder and more defects. And the order parameter has high fluctuations due to the lack of coupling. On the other hand, the conduction electrons can be localized due to the disorder, which is incompatible with the superconductivity state. Therefore, a superconductor-insulator transition will happen so that the resistance greatly increased with the decreasing of the temperature. In this case, 2D superconductivity is quite sensitive to the thickness of the thin film.

For ultrathin metal films, the conduction electrons are quantized in the out of plane direction to form quantum well states (QWS). In this direction, the movement of electrons are confined only in the space of the thin film, which can be expressed as the Bohr-Sommerfeld quantization rule[161]:

$$\frac{4\pi d}{\lambda(E)} + \Phi(E) = 2n\pi \tag{8.4}$$

where d is the thickness of the superconducting thin film, $\lambda(E)$ is the electron wavelength when the energy is E, Φ is the total phase shift at the boundaries, and n is an integer. The formation of QWS induces an oscillation of electron density of states at the Fermi level, which causes an oscillation of the critical temperature. The first successful observation of the oscillation is in a Pb films on Si(110) thin film[162].

When consider atomically uniform thickness thin film, the critical temperature has a strong dependence on the thickness[149, 163, 164]:

$$T_c(d) = T_{c0}(1 - \frac{d_c}{d}) \tag{8.5}$$

where T_{c0} is the critical temperature when the thickness of the film is infinite (bulk

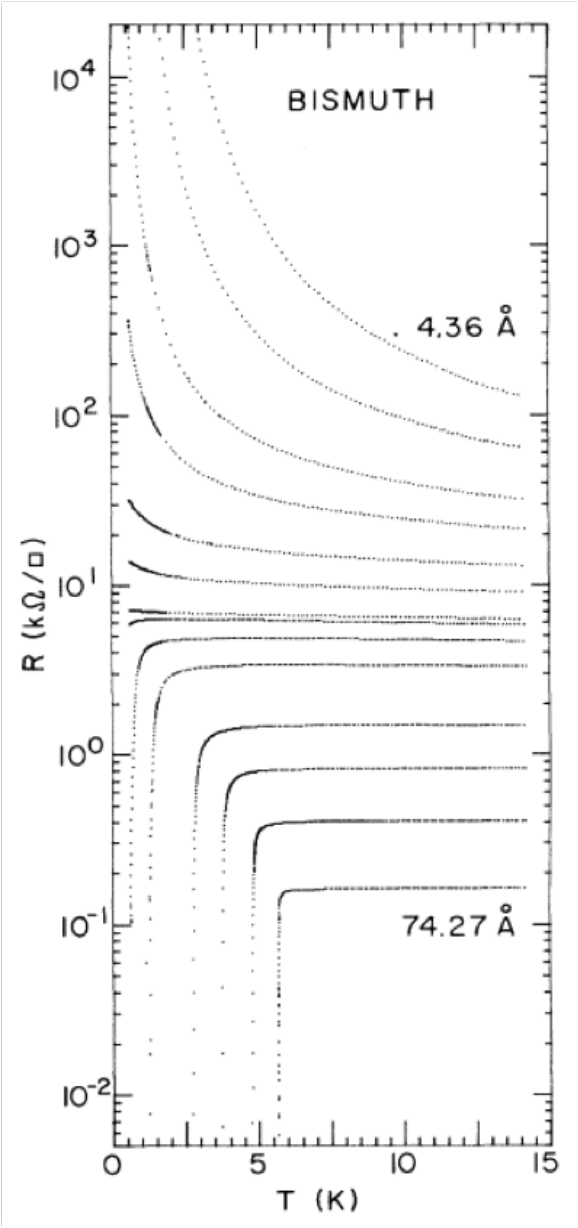

Figure 8.1: Disorder induced S-I transition of Bi films. When the thickness of Bi is thicker than a critical thickness (4.36 $\mathring{A}$), it can show superconductivity. However, when the thickness is thinner than this value, the disorder in the system will induce the S-I transition, which makes the superconductivity disappear.[160]

limit), d_c is the critical thickness for the disappear of superconductivity. From the equation one can see that the critical temperature decreases with the decreasing of the thickness. And when the thickness large, T_c approximates to the critical temperature of the bulk material. This behavior can be explained by the changing of free energy in the GL theory by introducing a surface energy term, as well as other possibilities such as the surface roughness and/or disorder[165].

Besides temperature, external magnetic field can also greatly affect the superconductivity. When in plane field is applied, there exists no orbital pair-breaking effect. This is because the thickness is quite thin, usually a few atomic layer, so that the movement of electrons in the out of plane direction is very limited. Therefore, the in plane upper critical field, H_{c2} can be calculated by[29]:

$$\mu_0 H_{c2\parallel} = \frac{\Delta(0)}{\sqrt{2}\mu_B} \tag{8.6}$$

where $\Delta(0)$ is the superconductor gap at zero temperature and μ_B is Bohr magneton. When the field is not in plane, but has an angle θ with the in plane direction, there will be an component out of plane. The out of plane field will break the Cooper pair, because of the Zeeman energy induced by the field. For the spin along the field direction, the Zeeman energy will be $-\mu \cdot \mathbf{B}$, while for the spin opposite to the field direction, the Zeeman energy will be $\mu \cdot \mathbf{B}$. The energy difference will break the Cooper pair and the spin with higher energy will flip, which is known as Pauli paramagnetism. Generally, for a quasi-2D superconductor with weakly coupled conducting layers, there is an angular dependence of the upper critical field $H_{c2}(\theta)$. In the 3D anisotropic GL model, this anisotropy can be expressed as[29]:

$$(\frac{H_{c2}(\theta)cos\theta}{H_{c2}(0^\circ)})^2 + (\frac{H_{c2}(\theta)sin\theta}{H_{c2}(90^\circ)})^2 = 1 \tag{8.7}$$

This equation can be applied to fairly thicker thin films, i.e., the coherence length

is larger than the interlayer distance. On the other hand, when the film is thin so that the coherence length is much smaller than the penetration depth, one has to use the 2D Tinkham model[166] which can be expressed as:

$$(\frac{H_{c2}(\theta)cos\theta}{H_{c2}(0^\circ)})^2 + (\frac{H_{c2}(\theta)sin\theta}{H_{c2}(90^\circ)}) = 1 \tag{8.8}$$

This 2D Tinkham model will exhibit a cusp-like shape, which can be observed in some systems with strong field anisotropy[167].

8.2 FeSe

The tetragonal phase $\alpha - FeSe$ is one of the high critical temperature superconductor which exhibits superconductivity below 8K at ambient pressure and 37K under a pressure about 8.9GP[168, 169]. FeSe is under intense study due to its unusual physical properties[170]. The atomic layers in bulk FeSe are weakly bounded via van der Waals interaction. However, for 1 unit cell FeSe layers epitaxially grown on a $SrTiO_3$ substrate, the superconductivity behavior is quite different from the bulk material. Experimental results showed the critical temperature is between 23.5K to 109K, depending on the experimental environment[143, 155], and a superconductor gap about 20meV[171]. This is quite different from the FeSe grown on bilayer graphene[172]. In the latter case, superconductivity can not be detected when the temperature is above 2.2K and the T_c decreases with the decreasing of the FeSe thickness, which is similar to the behavior of Pb layer, suggesting the similar mechanism. In the previous discussion, Pb thin film is grown on a Si substrate so that there is no interaction between the Pb atoms with the Si atoms in the structures. By contrast, the greatly increased T_c in the $FeSe - SrTiO_3$ structure indicates a strong interaction between the FeSe atomic layer with the substrate.

As is shown in equation(8.5), critical temperature decreases for decreasing thin

film thickness. In the FeSe grown on $SrTiO_3$ substrate, the high T_c may come from the strain between the two materials, which will enhance the electron-phonon coupling, polaronic effects and carrier doping from the interface[155]. Additionally, the high T_c may also comes from the arise of optical phonon modes at the interface and the spin density wave (SDW) in the FeSe layer[173, 174]. And more experimental and theoretical studies are still needed to clarify the real mechanism of the unique behavior.

8.3 $NbSe_2$

In 2004, a atomic layer of graphene was successfully exfoliated from a piece of graphite to fabricate FET devices[175], which shined light on a new way to study atomic level materials. Afterwords, half-integer quantum Hall effect was discovered on graphene at low temperature[176, 177], which stimulated heavily research studies on this fancy material, including graphene related superconductivity. Even though superconductivity has not been observed on pure graphene, it has already been observed on graphite intercalations compound with alkaline or alkaline-earth metal layers, such as $KC_8(T_c = 0.14K)$[178], $CaC_6(T_c = 11.5K)$[179] and $YbC_6(T_c = 6.5K)$[180]. The metal materials is the key to achieve superconductivity in the structures since they donate electrons into the π^* bands of graphite and modify the electron-phonon interaction[143]. Recently, superconductivity was also discovered on metal doped graphene layers, such as K-doped graphene in dimethoxyethane solution[181], Li-intercalcated few layer graphene[182]. And more research has been conducted to explore new intercalated or chemically doped graphene materials.

The mechanical exfoliation of graphene from bulk graphite has greatly motivated the study of atomic layers using the same method, including the atomic sheets of transition metal dichalcogenides, such as MoS_2 and $NbSe_2$. The layers of transition metal

dichalcogenides are only weakly bounded by the van der Waals force[143], making the mechanical exfoliation an easy way to achieve single atomic layer of these materials. Bulk $NbSe_2$ is a well studied type II SC with anisotropic multiband superconductor. The critical temperature at zero field is reported to be around 7K [183–188]. $NbSe_2$ atomic layer was first studied in 1972[189]. Electron transport data indicate the SC transition at a few UC thickness, with a critical temperature varies from 2K to about 5K[189]. However, loss of superconductivity was also detected[190], due to exposure to air, which has been solved by preparing the sample in an inert gas environment and well protect the sample with a graphene or BN atomic sheet[191].

$NbSe_2$ monolayer is of half UC thickness and lack in plane inversion symmetry, which can result in spin valley locking[192, 193]. Recent experiment shows a critical temperature for monolayer $NbSe_2$ about 3K[154], and the estimated upper critical field at zero K can be as high as 35T, which is about 6 times larger than the Pauli paramagnetic limit. The large upper critical field indicates that the $NbSe_2$ is an Ising superconductor, in which the Cooper pairs are aligned in the out of plane direction due to the spin valley locking. The SC can be destroyed by a small out of plane field of 0.175T[194]. At higher field, the presence of the Bose metal phase was indicated, in which uncondensed Cooper pairs and vortices are responsible for the non zero resistance[143, 195].

The Ising pairing in $NbSe_2$ is supposed to be induced by the Ising spin-orbital coupling (SOC), which prevents the electrons from being aligned with the in-plane field[192, 193]. Due to the strong Ising SOC, Ising superconductors could be used to engineer Majorana fermions[196–198]. Besides, theoretical study shows that there may exist nodes in the $NbSe_2$ superconductor gap, which are connected by the Majorana flat band[199]. Those Majorana flat bands are related with the zero energy Majorana fermion edge modes, which will induce the spin polarized Cooper pairs.

To study the spin pairing configuration in $NbSe_2$ monolayer, especially to verify if there exists spin polarized Cooper pairs (triplet spin pairing), Andreev Reflection Spectroscopy (ARS) is used. To get high quality $NbSe_2$ monolayer, a material, $NbBiSe_3$, is fabricated, with a monolayer of $NbSe_2$ sandwiched between two insulating layer of BiSe. As is discussed above, the air exposure will greatly affect the superconductivity of $NbSe_2$, so that the two insulating BiSe layer can well protect it. On the other hand, the BiSe layers are also serves as an effective spacer, which can reduce the interaction between two $NbSe_2$ monolayers, ensuring a real isolated monolayer. To make a stable point contact on the $NbSe_2$ monolayer for ARS measurement, the sample is cleaved so that a fresh sharp monolayer can be suspended in the air for measurement. And a piece of Au or LSMO is made into a sharp wedge to make a atomic level point contact, as is shown in figure(8.2).

8.4 Results and Discussions

After the contact is made, it is important to verify that the contact is made on a monolayer $NbSe_2$. For bulk $NbSe_2$, the T_c is about 7K, and the T_c gradually decreases as the thickness of the thin film decreases. According to other experiments, the bilayer $NbSe_2$ has a critical temperature 5.4K, and the monolayer $NbSe_2$ has a critical temperature about 3K[154, 200–202]. The obvious difference between the T_c of different number of layers of $NbSe_2$ makes it possible to verify how many layers are actually contacted in the ARS measurement by measuring the critical temperature for the contacts with different contact resistance. The different contact resistance can represent different number of atomic layers, because for more layers being contacted, the electrons can be transported into more superconducting layers, which will result in smaller resistance. As is shown in the left of figure(8.3), different contacts show different critical temperature. The y-axis represents the contact resistance and the x-

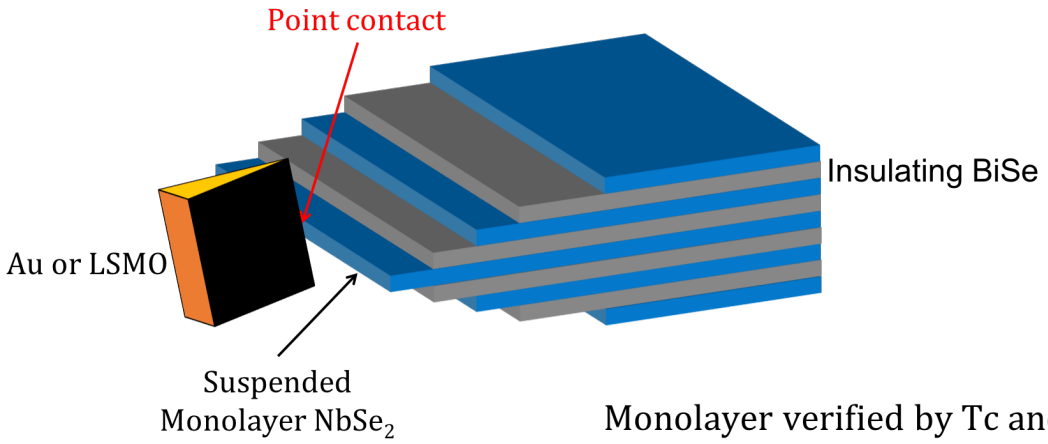

Figure 8.2: $NbSe_2$ monolayer is achieved by cleave the edge of $NbBiSe_3$, which has an alternating $NbSe_2$ and insulating BiSe. Au or LSMO is made into sharp wedge to make a atomic level point contact on the $NbSe_2$ monolayer for ARS measurement

axis is the temperature. From the figure it is clear to see that if the contact resistance (R_C) is larger, the T_c is smaller. After normalization, the T_c is easier to be observed. On the right side of figure(8.3), one can see that for the red curves, the T_c is about 3K, which is corresponding to the contact on a monolayer $NbSe_2$; and for the blue curves, the T_c varies from 5K to 6K, therefore the contacts are actually made on bilayer, trilayer or even bulk $NbSe_2$. The broadening of the R-T curve at thinner thickness can be attributed to the enhanced thermal fluctuations in 2 dimension[29, 203], where the thickness is thinner than the out of plane coherence length of 2.7nm[184].

To further confirm the monolayer contact, the critical field is measured for the contacts with different contact resistance. Due to the Ising pairing in the $NbSe_2$ superconductor, the in plane critical is reported to be larger than 35T[154]. Therefore, an in plane critical field measurement is hard to distinguish monolayer from multilayers or bulk, under the limitation of the maximum magnetic field can be realized in the lab. However, the our of plane critical field is reported to be much smaller than the in plane critical field and also varies with the number of $NbSe_2$ layers. As is reported in other work[154], the out of plane critical field for a monolayer $NbSe_2$ is about 1T, while the value for bilayer, trilayer and bulk is approximately 10T, which is so different from that of the monolayer that it is possible to use the out of plane critical field value to distinguish the number of superconducting layers. In this measurement, a sharp Au wedge is used for more stable contact under the external field. In figure(8.4), (a) and (b) shows the critical temperature and critical field measurement for the same contact, respectively. This contact has a fairly larger contact resistance, with a $T_c = 3K$, which is corresponding to the monolayer. When an out of plane magnetic field is applied, the resistance drops sharply when the field is close to zero, which is due to the superconductivity of the $NbSe_2$ layer. When the field increases to about 1T, the resistance greatly increases and almost become flat

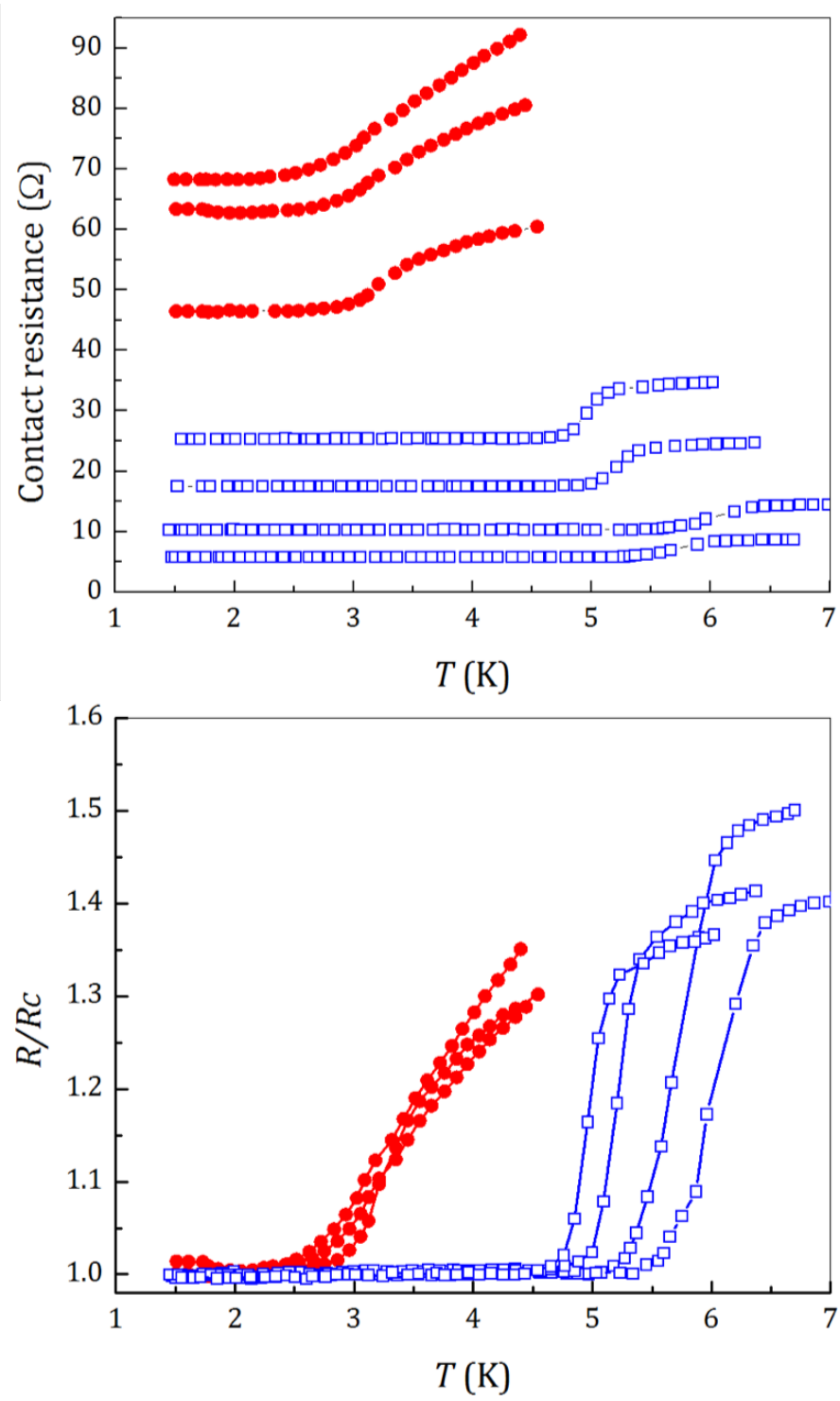

Figure 8.3: The critical temperature is quite different for different contact resistance. Top: Raw data. T_c increases with the decreasing of contact resistance. Bottom: normalized data. For larger contact resistance, the T_c is about 3K, which indicates monolayer. For smaller contact resistance, the T_c varies from 5 to 6K, which is the values for multilayers or bulk.

when the field is larger than 1T. This behavior is corresponding to the disappearance of superconductivity and the experimental critical field is about 1T, which further confirms that this contact is on a monolayer of $NbSe_2$. (c) and (d) show the result for the similar measurements on a contact with smaller contact resistance. In (c), the critical temperature can be decided from the sharp increase in the resistance, which is about 5K so that the contact may be made on multilayer, according to the previous discussion. When a out of plane field is applied, the resistance drops sharply when the field is around 0, but increases slowly with the increasing of the field. When the field is about 5T, the tail in the curve (d) still not totally flat, indicating that the critical field for this contact must be larger than 5T, which, again, further confirms that this contact is on multilayer $NbSe_2$.

After determine the contacts of monolayer $NbSe_2$, Andreev Reflection is measured with a Au/$NbSe_2$ contact. In figure(8.5), the black open circles represent the measurement without magnetic field. From the result, one can see that when the bias voltage is larger (smaller) than 2 (-2) mV, the normalized differential conductance is 1, which is because the energy of the electrons gained from the bias voltage is higher than the superconductor gap value, 2Δ, so that the electrons enter the superconductor without forming Cooper pairs, and suffer from normal scattering from the crystal lattice of the material. On the other hand, however, when the bias voltage is between -2 and +2 mV, the differential conductance shows a clear peak, which is corresponding to the formation of Cooper. The maximum value of the peak is about 1.4, which is smaller than the theoretical value, 2. This is due to the scattering of electrons at the interface between Au and $NbSe_2$. When a in plane magnetic field about 5.8T is applied to the same contact for the same measurement (shown as red open circles), one can clearly see that the Andreev reflection results are almost identical with the ones without magnetic field. This is because the in plane critical is supposed to be

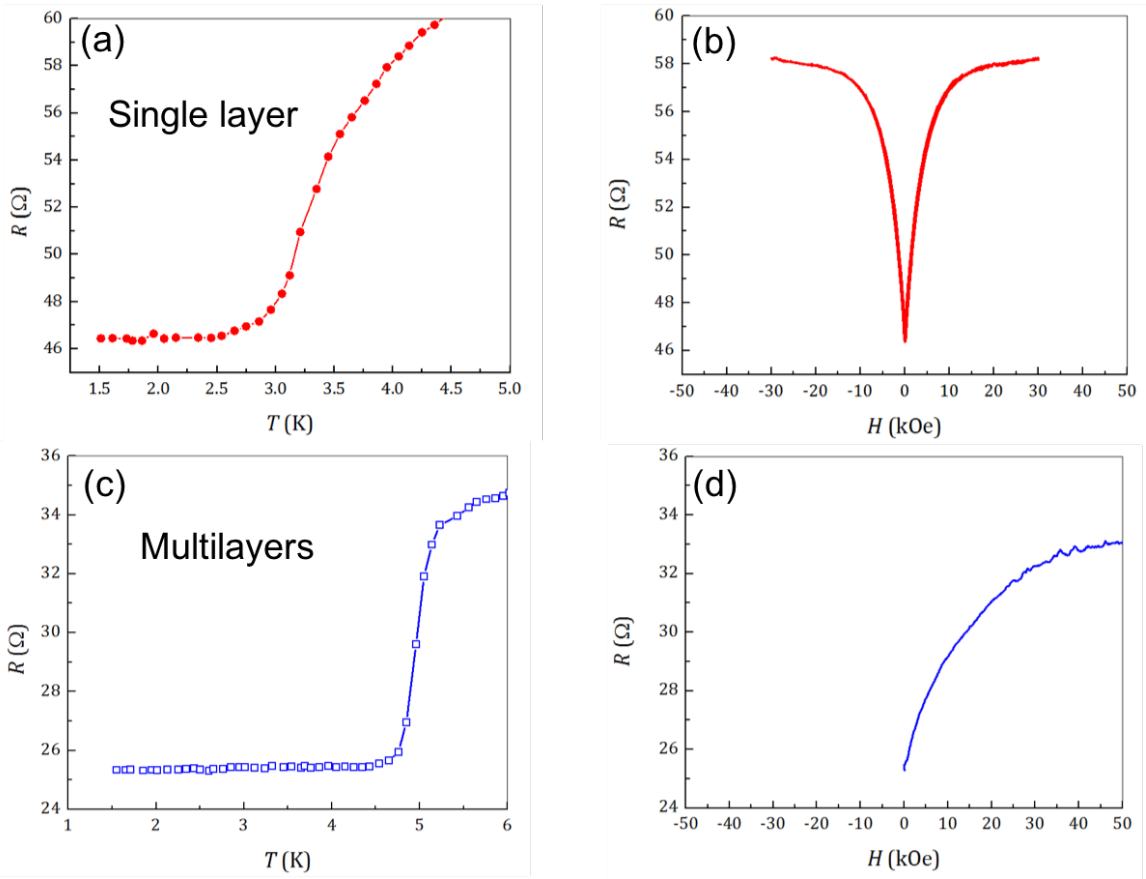

Figure 8.4: (a) A Au/$NbSe_2$ contact with larger contact resistance and a T_c about 3K. (b). Out of plane critical for the contact in (a) is around 1T, indicating a monolayer contact. (c).A Au/$NbSe_2$ contact with larger contact resistance and a T_c about 5K. (b). Out of plane critical for the contact in (a) is larger than 10T, indicating a multilayer contact.

larger than 35T, so that a 5.8T field have almost no effect on the existence of the superconductivity. Again, this is also consistent with the monolayer critical field.

To further study the spin pairing in the Cooper, a LSMO sharp wedge is used to replace the Au wedge. LSMO is a highly spin polarized material. If the $NbSe_2$ has single spin pairing, the differential conductance should decreases within the superconductor gap. By contrast, if the material has a triplet spin pairing, the differential conductance should increase in the gap, similar with the case of a Au contact. Figure(8.6) shows the results. On the left is a 3-D figure which shows the differential conductance measurement under different external in-plane field. One can clearly see that for all the measurements with the field ranging from zero to 5.8T, the differential conductance shows a decrease within a small bias voltage (superconductor gap). This clear dip shows that there is no nodes in the superconducting gap. If there exists node in the gap, the Cooper pair will be spin polarized so that the two spins in one Cooper pair can be parallel. If a piece of half metal (LSMO) is used, Cooper pair can be formed so that the differential conductance should increase. However, for this material, there is no peak observed for all the contacts, even under a field as high as 5.8T. This indicate that the $NbSe_2$ is a singlet superconductor so that the two spins in one Cooper pair has to be antiparallel. Thus, when a piece of LSMO is used to make contact, no Cooper pair can be formed at the interface between the two materials and a dip will appear.

The curve on the left of figure(8.6) is a representative curve of the LSMO/$NbSe_2$ contact. The blue open circles are the raw data under zero magnetic field and the blue open square are the ones under 5.8T in-plane field. The red line is the best fit of the data using the mBTK model. The fitting parameters shows the relative properties of the two materials: the spin polarization (P) value is about 0.794 (79.4%), which is consistent with the P value for LSMO. The superconductor gap for the $NbSe_2$ is

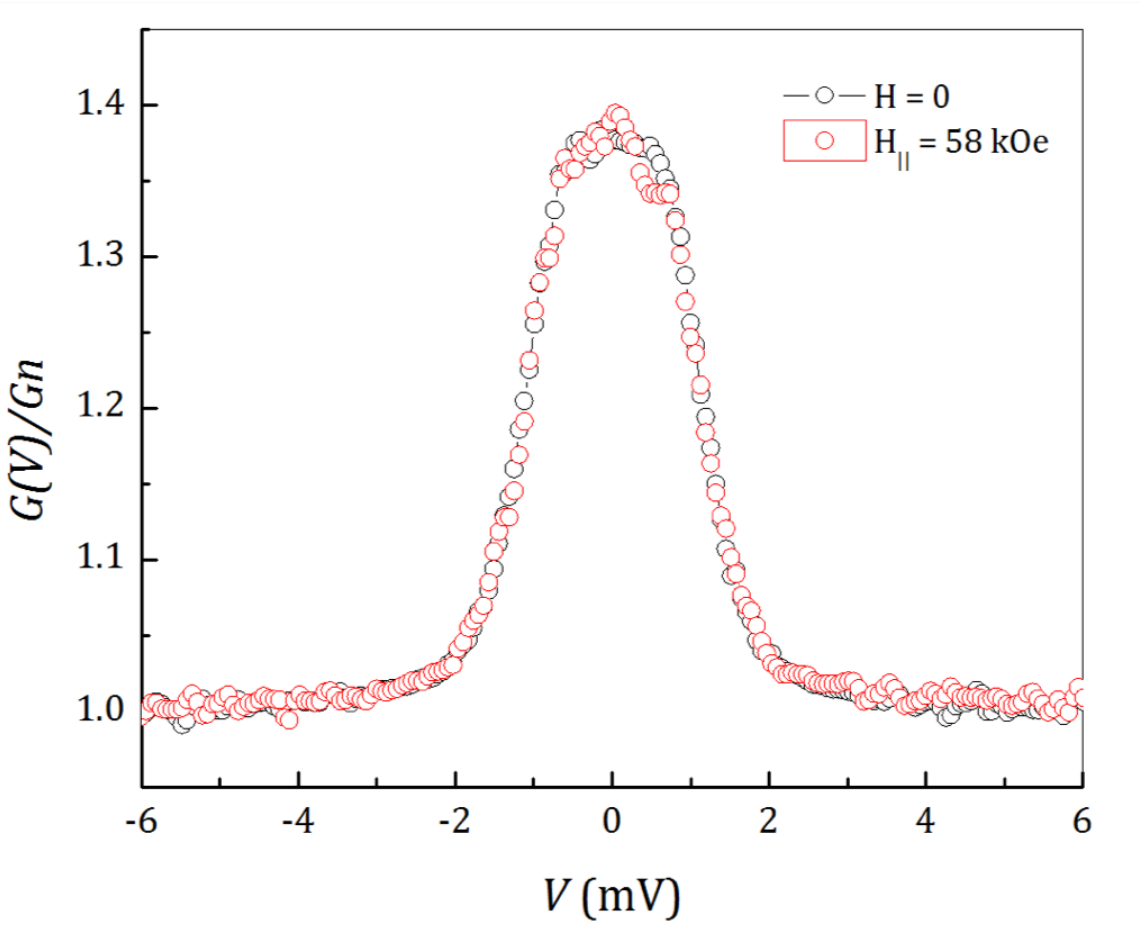

Figure 8.5: Andreev reflection measurement of a Au/$NbSe_2$ contact. A peak is clearly observed under zero field and under 5.8T in plane field, which is typical for Ising pairing.

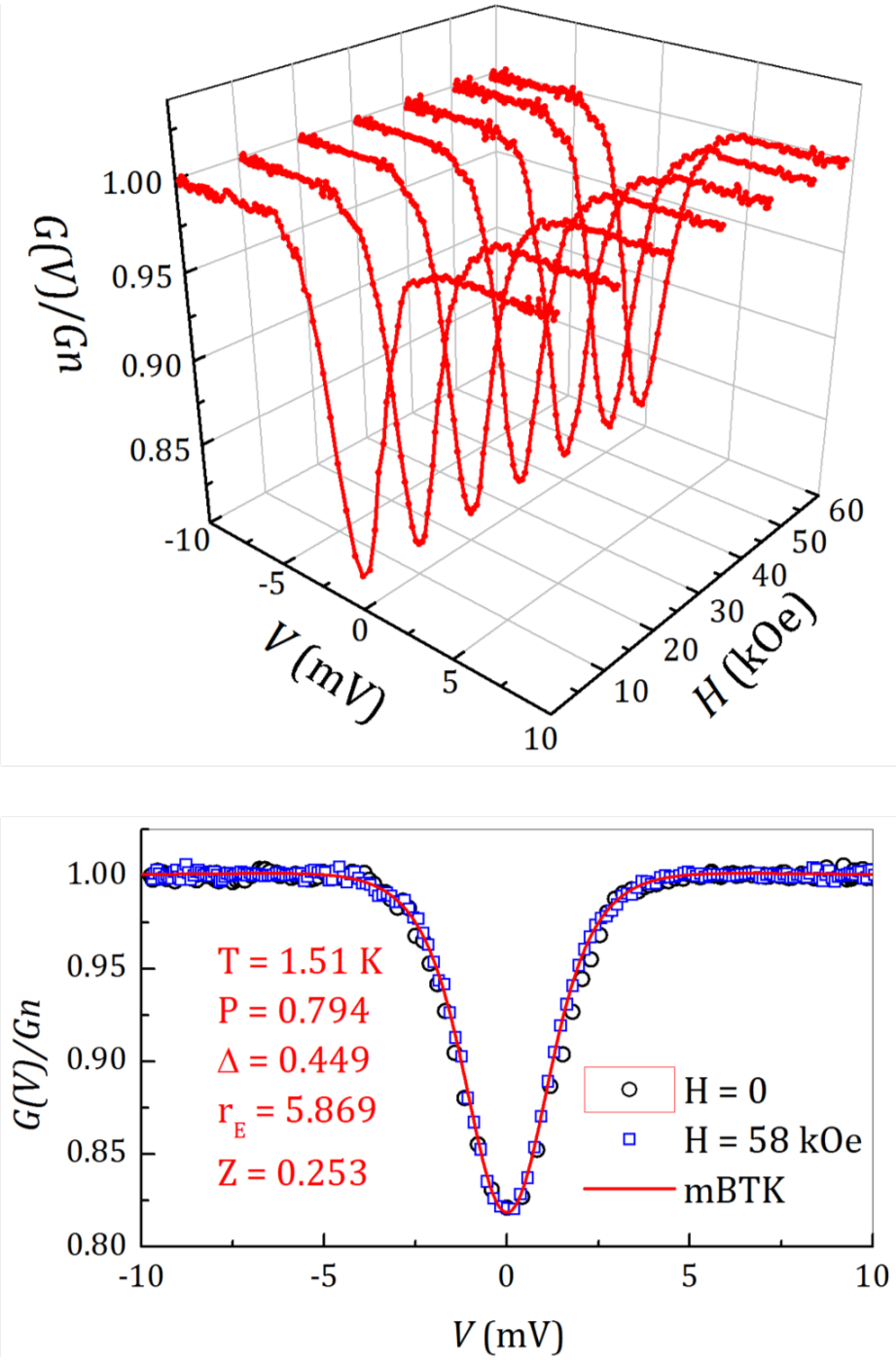

Figure 8.6: Andreev reflection measurement of a LSMO/$NbSe_2$ contact. Top: 3-D curves for Andreev reflection measurements under different field. All the curves show dips, indicating singlet superconductivity. Bottom: A representative curve of Andreev reflection measurement under zero field and 5.8T in plane field. The blue open circles and squares are the raw data for the measurements under zero field and 5.8T field, respectively. The red solid line is the best fit using the mBTK model. The fitting parameters are listed inside the figure.

about $2\Delta = 0.898meV$, and the scattering factor is about Z=0.253.

At last, a out of plane field is applied to the same LSMO/$NbSe_2$ contact. Since this superconductor has a quite small out of plane critical field, the Andreev reflection curve will disappear very quick with the increasing of the field. Figure(8.7) shows the results for this contact. The red solid dots are the raw data for zero field and the blue open squares represent the data when the field is about 3T. One can clearly see a dip when the field is zero. The minimum of the dip is about 0.83, larger than the ideal value, 0. This is because the spin polarization of LSMO is about 80%, which is much smaller than that of a ideal half metal (P=100%). Therefore, when Andreev reflection is measured, the minority spin band in the LSMO is not zero so that there are always some Cooper pair can be formed. On the other hand, the scattering factor may also have effect on the value of differential conductance value. When the field is about 3T, the Andreev reflection spectrum almost disappears, which is corresponding to the disappearance of superconductivity of $NbSe_2$. The out of plane critical field in this case is larger than that in the previous measurement (figure(8.4)), which is because the LSMO may contact on a few other atomic layers so that the critical field increases a little bit. Besides, LSMO has highly spin polarization, which will generate a magnetic field around it and affect the critical field of the superconductor.

As a conclusion, Andreev Reflection Spectroscopy is used to study a monolayer of $NbSe_2$. Due to the huge difference on critical temperature and out of plane critical field between monolayer and multilayer $NbSe_2$, it is convenient to use these values to decide whether the point contact is made on a monolayer or not. The Au/$NbSe_2$ contact shows a increase in the differential conductance, which is typical for any superconductor. According to the experimental data, the in plane critical field must be larger than 5.8T, which is consistent with the Ising pairing of the Cooper pair. The LSMO/$NbSe_2$ contact shows a decrease in the differential conductance, which

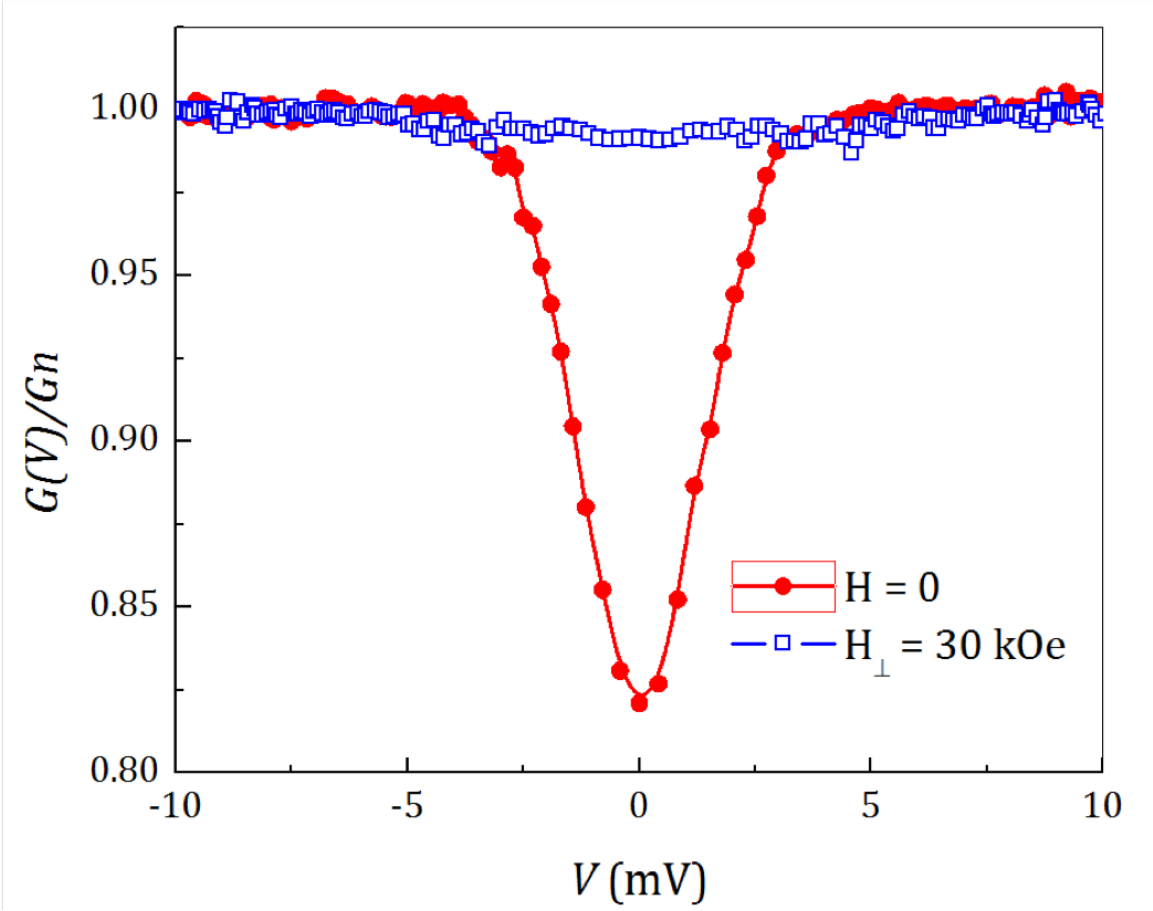

Figure 8.7: Andreev reflection measurement of a LSMO/$NbSe_2$ contact with out-of-plane field. Red solid dots: raw data for measurement under 0 field; Blue open squares: raw data for measurement with 3T out-of-plane field. Andreev reflection dip appears when there is no magnetic field and disappears when the field is about 3T.

is corresponding to a singlet superconductor, for a magnetic field up to 5.8T. This results indicate that there is no node in the superconducting gap of the $NbSe_2$ under this field. Since the critical temperature for this monolayer is about 3K, so that the Pauli limit for it is about $1.84T_c = 5.52T$. The in plane field applied in the lab is about 5.8T, which is close to the Pauli limit. This may be the reason that the node can not be observed under this field. If the field can be larger (at least 6 times larger than that of the Pauli limit), the node may appear in the superconductor gap so that spin polarized Cooper might be observed.

8.5 Acknowledgement

This work was supported as part of SHINES, an EFRC center funded by the U. S. Department of Energy, Office of Science, Basic Energy Science, under award SC0012670.

REFERENCES

[1] A Buzdin. Direct coupling between magnetism and superconducting current in the josephson φ 0 junction. *Physical review letters*, 101(10):107005, 2008.

[2] Peter Moller. *Electric fishes: history and behavior*, volume 17. Chapman & Hall, 1995.

[3] Hugh P Vowles. Early evolution of power engineering. *Isis*, 17(2):412–420, 1932.

[4] Massimo Guarnieri. The age of vacuum tubes: Early devices and the rise of radio communications [historical]. *IEEE Industrial Electronics Magazine*, 6(1):41–43, 2012.

[5] Charles J Bashe, Lyle R Johnson, John H Palmer, and Emerson W Pugh. *IBM's early computers*. MIT press, 1986.

[6] David J Griffiths. *Introduction to quantum mechanics*. Cambridge University Press, 2016.

[7] Grünberg Binasch, Peter Grünberg, F Saurenbach, and W Zinn. Enhanced magnetoresistance in layered magnetic structures with antiferromagnetic interlayer exchange. *Physical review B*, 39(7):4828, 1989.

[8] Mario Norberto Baibich, Jean Marc Broto, Albert Fert, F Nguyen Van Dau, Frédéric Petroff, P Etienne, G Creuzet, A Friederich, and J Chazelas. Giant magnetoresistance of (001) fe/(001) cr magnetic superlattices. *Physical review letters*, 61(21):2472, 1988.

[9] JA Gifford, GJ Zhao, BC Li, Brian D Tracy, J Zhang, DR Kim, David J Smith, and TY Chen. Continuous control of spin polarization using a magnetic field. *Applied Physics Letters*, 108(21):212401, 2016.

[10] Michel Julliere. Tunneling between ferromagnetic films. *Physics letters A*, 54(3):225–226, 1975.

[11] Terunobu Miyazaki and N Tezuka. Giant magnetic tunneling effect in fe/al2o3/fe junction. *Journal of Magnetism and Magnetic Materials*, 139(3):L231–L234, 1995.

[12] Jagadeesh Subbaiah Moodera, Lisa R Kinder, Terrilyn M Wong, and R Meservey. Large magnetoresistance at room temperature in ferromagnetic thin film tunnel junctions. *Physical review letters*, 74(16):3273, 1995.

[13] WH Butler, X-G Zhang, TC Schulthess, and JM MacLaren. Spin-dependent tunneling conductance of fe— mgo— fe sandwiches. *Physical Review B*, 63(5):054416, 2001.

[14] J Mathon and A Umerski. Theory of tunneling magnetoresistance of an epitaxial fe/mgo/fe (001) junction. *Physical Review B*, 63(22):220403, 2001.

[15] M Bowen, V Cros, F Petroff, Albert Fert, C Martınez Boubeta, José Luis Costa-Krämer, José Virgilio Anguita, Alfonso Cebollada, F Briones, JM De Teresa, et al. Large magnetoresistance in fe/mgo/feco (001) epitaxial tunnel junctions on gaas (001). *Applied Physics Letters*, 79(11):1655–1657, 2001.

[16] Shinji Yuasa, Taro Nagahama, Akio Fukushima, Yoshishige Suzuki, and Koji Ando. Giant room-temperature magnetoresistance in single-crystal fe/mgo/fe magnetic tunnel junctions. *Nature materials*, 3(12):868, 2004.

[17] Stuart SP Parkin, Christian Kaiser, Alex Panchula, Philip M Rice, Brian Hughes, Mahesh Samant, and See-Hun Yang. Giant tunnelling magnetoresistance at room temperature with mgo (100) tunnel barriers. *Nature materials*, 3(12):862, 2004.

[18] S Ikeda, J Hayakawa, Y Ashizawa, YM Lee, K Miura, H Hasegawa, M Tsunoda, F Matsukura, and H Ohno. Tunnel magnetoresistance of 604% at 300 k by suppression of ta diffusion in co fe b/ mg o/ co fe b pseudo-spin-valves annealed at high temperature. *Applied Physics Letters*, 93(8):082508, 2008.

[19] NP Vasil'eva and Sergey Ivanovich Kasatkin. Magnetic random access memory devices. *Automation and Remote Control*, 64(9):1369–1385, 2003.

[20] Bradley N Engel, Jason Allen Janesky, and Nicholas D Rizzo. Magnetoresistive random access memory with reduced switching field, October 14 2003. US Patent 6,633,498.

[21] D Lammers. Mram debut cues memory transition. *ELECTRONIC ENGINEERING TIMES-MANHASSET-*, 1431:1, 2006.

[22] Soshin Chikazumi and Chad D Graham. *Physics of Ferromagnetism 2e*, volume 94. Oxford University Press on Demand, 2009.

[23] Robert C O'handley. *Modern magnetic materials: principles and applications*. Wiley, 2000.

[24] Pierre Weiss. L'hypothèse du champ moléculaire et la propriété ferromagnétique. *J. Phys. Theor. Appl.*, 6(1):661–690, 1907.

[25] H Barkhausen. Two phenomena revealed with the help of new amplifiers. *Phys. Z*, 29(6):401–403, 1919.

[26] Didier St Médar. An overview of micromagnetism, magnetization dynamics and skyrmions. 2016.

[27] D. Fishlock. *A guide to superconductivity*. Macdonald, 1969.

[28] Charles Kittel, Paul McEuen, and Paul McEuen. *Introduction to solid state physics*, volume 8. Wiley New York, 1996.

[29] Michael Tinkham. *Introduction to superconductivity*. Courier Corporation, 1996.

[30] Max Born and Kun Huang. *Dynamical theory of crystal lattices*. Clarendon press, 1954.

[31] Adwaele. Flux lines in a superconductor01.

[32] R. Nave. Energy gap in superconductors as a function of temperature.

[33] II Mazin, DJ Singh, and Claudia Ambrosch-Draxl. Transport, optical, and electronic properties of the half-metal cro 2. *Physical Review B*, 59(1):411, 1999.

[34] Jose Maria De Teresa, Agnès Barthélémy, Albert Fert, Jean Pierre Contour, François Montaigne, and Pierre Seneor. Role of metal-oxide interface in determining the spin polarization of magnetic tunnel junctions. *Science*, 286(5439):507–509, 1999.

[35] Y Ji, GJ Strijkers, FY Yang, CL Chien, JM Byers, A Anguelouch, Gang Xiao, and A Gupta. Determination of the spin polarization of half-metallic cro 2 by point contact andreev reflection. *Physical Review Letters*, 86(24):5585, 2001.

[36] RA De Groot, FM Mueller, PG Van Engen, and KHJ Buschow. New class of materials: half-metallic ferromagnets. *Physical Review Letters*, 50(25):2024, 1983.

[37] KEHM Hanssen and PE Mijnarends. Positron-annihilation study of the half-metallic ferromagnet nimnsb: Theory. *Physical Review B*, 34(8):5009, 1986.

[38] KP Kämper, W Schmitt, G Güntherodt, RJ Gambino, and R Ruf. Cr o 2—a new half-metallic ferromagnet? *Physical Review Letters*, 59(24):2788, 1987.

[39] H Van Leuken and RA De Groot. Half-metallic antiferromagnets. *Physical review letters*, 74(7):1171, 1995.

[40] Young-Woo Son, Marvin L Cohen, and Steven G Louie. Half-metallic graphene nanoribbons. *Nature*, 444(7117):347, 2006.

[41] MI Katsnelson, V Yu Irkhin, L Chioncel, AI Lichtenstein, and RA De Groot. Half-metallic ferromagnets: From band structure to many-body effects. *Reviews of Modern Physics*, 80(2):315, 2008.

[42] Sudipta Dutta, Arun K Manna, and Swapan K Pati. Intrinsic half-metallicity in modified graphene nanoribbons. *Physical review letters*, 102(9):096601, 2009.

[43] R Shan, H Sukegawa, WH Wang, M Kodzuka, T Furubayashi, T Ohkubo, S Mitani, K Inomata, and K Hono. Demonstration of half-metallicity in fermi-level-tuned heusler alloy co 2 feal 0.5 si 0.5 at room temperature. *Physical review letters*, 102(24):246601, 2009.

[44] Karlheinz Schwarz. Cro2 predicted as a half-metallic ferromagnet. *Journal of Physics F: Metal Physics*, 16(9):L211, 1986.

[45] GE Blonder, M Tinkham, and TM Klapwijk. Transition from metallic to tunneling regimes in superconducting microconstrictions: Excess current, charge imbalance, and supercurrent conversion. *Physical Review B*, 25(7):4515, 1982.

[46] Karl-Heinz Meiwes-Broer. *Metal clusters at surfaces: structure, quantum properties, physical chemistry*. Springer Science & Business Media, 2012.

[47] DK Maurya, Ali Sardarinejad, and Kamal Alameh. Recent developments in rf magnetron sputtered thin films for ph sensing applications—an overview. *Coatings*, 4(4):756–771, 2014.

[48] Milton Ohring. *Materials science of thin films*. Elsevier, 2001.

[49] Kenjiro Oura, VG Lifshits, AA Saranin, AV Zotov, and M Katayama. *Surface science: an introduction*. Springer Science & Business Media, 2013.

[50] MJM De Jong and CWJ Beenakker. Andreev reflection in ferromagnet-superconductor junctions. *Physical review letters*, 74(9):1657, 1995.

[51] B Nadgorny, II Mazin, M Osofsky, RJ Soulen Jr, P Broussard, RM Stroud, DJ Singh, VG Harris, A Arsenov, and Ya Mukovskii. Origin of high transport spin polarization in la 0.7 sr 0.3 mno 3: Direct evidence for minority spin states. *Physical Review B*, 63(18):184433, 2001.

[52] Y Ji, CL Chien, Y Tomioka, and Y Tokura. Measurement of spin polarization of single crystals of la 0.7 sr 0.3 mno 3 and la 0.6 sr 0.4 mno 3. *Physical Review B*, 66(1):012410, 2002.

[53] L Wang, K Umemoto, RM Wentzcovitch, TY Chen, CL Chien, JG Checkelsky, JC Eckert, ED Dahlberg, and C Leighton. C o 1- x f e x s 2: A tunable source of highly spin-polarized electrons. *Physical review letters*, 94(5):056602, 2005.

[54] JS Parker, SM Watts, PG Ivanov, and P Xiong. Spin polarization of cro 2 at and across an artificial barrier. *Physical review letters*, 88(19):196601, 2002.

[55] Eric D Daniel, C Denis Mee, and Mark H Clark. *Magnetic recording: the first 100 years*. John Wiley & Sons, 1999.

[56] Damien Gignoux, Michel Schlenker, and Étienne Du Trémolet de Lacheisserie. *Magnetism: Fundamentals*. Kluwer Academic Publishers, 2002.

[57] SN Piramanayagam and Tow C Chong. *Developments in data storage: materials perspective*. John Wiley & Sons, 2011.

[58] Magnetization in longitudinal bits.

[59] Shun-ichi Iwasaki and Kazuhiro Ouchi. Co-cr recording films with perpendicular magnetic anisotropy. *IEEE Transactions on Magnetics*, 14(5):849–851, 1978.

[60] Perpendicular magnetic structures in hitachi.

[61] Mariana F Chioncel and Peter W Haycock. Structural characterization of cobalt thin films grown by metal-organic cvd. *Chemical Vapor Deposition*, 11(5):235–243, 2005.

[62] PF Carcia, AD Meinhaldt, and A Suna. Perpendicular magnetic anisotropy in pd/co thin film layered structures. *Applied Physics Letters*, 47(2):178–180, 1985.

[63] PF Carcia. Perpendicular magnetic anisotropy in pd/co and pt/co thin-film layered structures. *Journal of applied physics*, 63(10):5066–5073, 1988.

[64] Bharati Tudu and Ashutosh Tiwari. Recent developments in perpendicular magnetic anisotropy thin films for data storage applications. *Vacuum*, 146:329–341, 2017.

[65] S Bandiera, RC Sousa, B Rodmacq, and B Dieny. Enhancement of perpendicular magnetic anisotropy through reduction of co-pt interdiffusion in (co/pt) multilayers. *Applied Physics Letters*, 100(14):142410, 2012.

[66] GHO Daalderop, PJ Kelly, and MFH Schuurmans. Magnetic anisotropy of a free-standing co monolayer and of multilayers which contain co monolayers. *Physical Review B*, 50(14):9989, 1994.

[67] JG Gay and Roy Richter. Spin anisotropy of ferromagnetic films. *Physical review letters*, 56(25):2728, 1986.

[68] Ding-sheng Wang, Ruqian Wu, and AJ Freeman. State-tracking first-principles determination of magnetocrystalline anisotropy. *Physical review letters*, 70(6):869, 1993.

[69] HX Yang, M Chshiev, B Dieny, JH Lee, Aurelien Manchon, and KH Shin. First-principles investigation of the very large perpendicular magnetic anisotropy at fe— mgo and co— mgo interfaces. *Physical Review B*, 84(5):054401, 2011.

[70] B Rodmacq, S Auffret, B Dieny, S Monso, and P Boyer. Crossovers from in-plane to perpendicular anisotropy in magnetic tunnel junctions as a function of the barrier degree of oxidation. *Journal of applied physics*, 93(10):7513–7515, 2003.

[71] Jaivardhan Sinha, Maria Gruber, Masaya Kodzuka, Tadakatsu Ohkubo, Seiji Mitani, Kazuhiro Hono, and Masamitsu Hayashi. Influence of boron diffusion on the perpendicular magnetic anisotropy in ta— cofeb— mgo ultrathin films. *Journal of Applied Physics*, 117(4):043913, 2015.

[72] Jaivardhan Sinha, Masamitsu Hayashi, Andrew J Kellock, Shunsuke Fukami, Michihiko Yamanouchi, Hideo Sato, Shoji Ikeda, Seiji Mitani, See-hun Yang, Stuart SP Parkin, et al. Enhanced interface perpendicular magnetic anisotropy in ta— cofeb— mgo using nitrogen doped ta underlayers. *Applied Physics Letters*, 102(24):242405, 2013.

[73] Chi-Feng Pai, Minh-Hai Nguyen, Carina Belvin, Luis Henrique Vilela-Leão, DC Ralph, and RA Buhrman. Enhancement of perpendicular magnetic anisotropy and transmission of spin-hall-effect-induced spin currents by a hf spacer layer in w/hf/cofeb/mgo layer structures. *Applied Physics Letters*, 104(8):082407, 2014.

[74] Luqiao Liu, OJ Lee, TJ Gudmundsen, DC Ralph, and RA Buhrman. Current-induced switching of perpendicularly magnetized magnetic layers using spin torque from the spin hall effect. *Physical review letters*, 109(9):096602, 2012.

[75] Mustafa Akyol, Juan G Alzate, Guoqiang Yu, Pramey Upadhyaya, Kin L Wong, Ahmet Ekicibil, Pedram Khalili Amiri, and Kang L Wang. Effect of the oxide layer on current-induced spin-orbit torques in hf— cofeb— mgo and hf— cofeb— taox structures. *Applied Physics Letters*, 106(3):032406, 2015.

[76] Can Onur Avci, Kevin Garello, Corneliu Nistor, Sylvie Godey, Belén Ballesteros, Aitor Mugarza, Alessandro Barla, Manuel Valvidares, Eric Pellegrin, Abhijit Ghosh, et al. Fieldlike and antidamping spin-orbit torques in as-grown and annealed ta/cofeb/mgo layers. *Physical Review B*, 89(21):214419, 2014.

[77] Junyeon Kim, Jaivardhan Sinha, Masamitsu Hayashi, Michihiko Yamanouchi, Shunsuke Fukami, Tetsuhiro Suzuki, Seiji Mitani, and Hideo Ohno. Layer thickness dependence of the current-induced effective field vector in ta— cofeb— mgo. *Nature materials*, 12(3):240, 2013.

[78] Shunsuke Fukami, Chaoliang Zhang, Samik DuttaGupta, Aleksandr Kurenkov, and Hideo Ohno. Magnetization switching by spin–orbit torque in an antiferromagnet–ferromagnet bilayer system. *Nature materials*, 15(5):535, 2016.

[79] VE Dmitrienko, EN Ovchinnikova, SP Collins, G Nisbet, G Beutier, YO Kvashnin, VV Mazurenko, AI Lichtenstein, and MI Katsnelson. Measuring the dzyaloshinskii–moriya interaction in a weak ferromagnet. *Nature Physics*, 10(3):202, 2014.

[80] Aurelien Manchon, Hyun Cheol Koo, Junsaku Nitta, SM Frolov, and RA Duine. New perspectives for rashba spin–orbit coupling. *Nature materials*, 14(9):871, 2015.

[81] Ioan Mihai Miron, Kevin Garello, Gilles Gaudin, Pierre-Jean Zermatten, Marius V Costache, Stéphane Auffret, Sébastien Bandiera, Bernard Rodmacq, Alain Schuhl, and Pietro Gambardella. Perpendicular switching of a single ferromagnetic layer induced by in-plane current injection. *Nature*, 476(7359):189, 2011.

[82] KJ Chang, Michel M Dacorogna, Marvin L Cohen, JM Mignot, G Chouteau, and G Martinez. Superconductivity in high-pressure metallic phases of si. *Physical review letters*, 54(21):2375, 1985.

[83] C Michel, M Hervieu, MM Borel, A Grandin, F Deslandes, J Provost, and B Raveau. Superconductivity in the bi-sr-cu-o system. *Zeitschrift für Physik B Condensed Matter*, 68(4):421–423, 1987.

[84] A Schilling, M Cantoni, JD Guo, and HR Ott. Superconductivity above 130 k in the hg–ba–ca–cu–o system. *Nature*, 363(6424):56, 1993.

[85] Anne Volbeda, Marie-Helene Charon, Claudine Piras, E Claude Hatchikian, Michel Frey, and Juan C Fontecilla-Camps. Crystal structure of the nickel–iron hydrogenase from desulfovibrio gigas. *Nature*, 373(6515):580, 1995.

[86] TY Chen, Z Tesanovic, RH Liu, XH Chen, and CL Chien. A bcs-like gap in the superconductor smfeaso 0.85 f 0.15. *Nature*, 453(7199):1224, 2008.

[87] Andrew Peter Mackenzie and Yoshiteru Maeno. The superconductivity of sr 2 ruo 4 and the physics of spin-triplet pairing. *Reviews of Modern Physics*, 75(2):657, 2003.

[88] Yoshiteru Maeno, Shunichiro Kittaka, Takuji Nomura, Shingo Yonezawa, and Kenji Ishida. Evaluation of spin-triplet superconductivity in sr2ruo4. *Journal of the Physical Society of Japan*, 81(1):011009, 2011.

[89] Ying Liu and Zhi-Qiang Mao. Unconventional superconductivity in sr 2 ruo 4. *Physica C: Superconductivity and its Applications*, 514:339–353, 2015.

[90] VL Berezinskii. New model of the anisotropic phase of superfluid he3. *Jetp Lett*, 20(9):287–289, 1974.

[91] A Layzer and D Fay. Spin-fluctuation exchange mechanism for p-wave pairing in liquid 3 he. *Int J Magn*, 1:135, 1971.

[92] PHILIP W Anderson and WF Brinkman. Anisotropic superfluidity in he 3: A possible interpretation of its stability as a spin-fluctuation effect. *Physical Review Letters*, 30(22):1108, 1973.

[93] GR Stewart, Z Fisk, JO Willis, and JL Smith. Possibility of coexistence of bulk superconductivity and spin fluctuations in u pt 3. *Physical review letters*, 52(8):679, 1984.

[94] K Ishida, D Ozaki, T Kamatsuka, Hideki Tou, M Kyogaku, Y Kitaoka, N Tateiwa, NK Sato, N Aso, C Geibel, et al. Spin-triplet superconductivity in uni 2 al 3 revealed by the a 27 l knight shift measurement. *Physical review letters*, 89(3):037002, 2002.

[95] SS Saxena. Ss saxena et al., nature (london) 406, 587 (2000). *Nature (London)*, 406:587, 2000.

[96] Dai Aoki, Andrew Huxley, Eric Ressouche, Daniel Braithwaite, Jacques Flouquet, Jean-Pascal Brison, Elsa Lhotel, and Carley Paulsen. Coexistence of superconductivity and ferromagnetism in urhge. *Nature*, 413(6856):613, 2001.

[97] NT Huy, A Gasparini, DE De Nijs, Y Huang, JCP Klaasse, T Gortenmulder, Anne de Visser, A Hamann, T Görlach, and H v Löhneysen. Superconductivity on the border of weak itinerant ferromagnetism in ucoge. *Physical review letters*, 99(6):067006, 2007.

[98] M Nishiyama, Y Inada, and Guo-qing Zheng. Spin triplet superconducting state due to broken inversion symmetry in li 2 pt 3 b. *Physical review letters*, 98(4):047002, 2007.

[99] Ernst Bauer, Gerfried Hilscher, Herwig Michor, Ch Paul, EW Scheidt, A Gribanov, Yu Seropegin, H Noël, M Sigrist, and Peter Rogl. Heavy fermion superconductivity and magnetic order in noncentrosymmetric c e p t 3 s i. *Physical review letters*, 92(2):027003, 2004.

[100] RS Keizer, STB Goennenwein, TM Klapwijk, G Miao, Gang Xiao, and A Gupta. A spin triplet supercurrent through the half-metallic ferromagnet cro 2. *Nature*, 439(7078):825, 2006.

[101] Patrick A Lee and Xiao-Gang Wen. Spin-triplet p-wave pairing in a three-orbital model for iron pnictide superconductors. *Physical Review B*, 78(14):144517, 2008.

[102] K Ishida, H Mukuda, Y Kitaoka, K Asayama, ZQ Mao, Y Mori, and Y Maeno. Spin-triplet superconductivity in sr 2 ruo 4 identified by 17 o knight shift. *Nature*, 396(6712):658, 1998.

[103] KD Nelson, ZQ Mao, Y Maeno, and Y Liu. Odd-parity superconductivity in sr2ruo4. *Science*, 306(5699):1151–1154, 2004.

[104] Chetan Nayak. C. nayak, sh simon, a. stern, m. freedman, and s. das sarma, rev. mod. phys. 80, 1083 (2008). *Rev. Mod. Phys.*, 80:1083, 2008.

[105] F Romeo and R Citro. Cooper pairs spintronics in triplet spin valves. *Physical review letters*, 111(22):226801, 2013.

[106] Vladimir P Mineev, K Samokhin, and LD Landau. *Introduction to unconventional superconductivity*. CRC Press, 1999.

[107] Gong Xin-Xin, Zhou He-Xin, Xu Peng-Chao, Yue Di, Zhu Kai, Jin Xiao-Feng, Tian He, Zhao Ge-Jian, and Chen Ting-Yong. Possible p-wave superconductivity in epitaxial bi/ni bilayers. *Chinese Physics Letters*, 32(6):067402, 2015.

[108] NR Werthamer, Ef Helfand, and PC Hohenberg. Temperature and purity dependence of the superconducting critical field, h c 2. iii. electron spin and spin-orbit effects. *Physical Review*, 147(1):295, 1966.

[109] Y Kozuka, M Kim, C Bell, Bog G Kim, Y Hikita, and HY Hwang. Two-dimensional normal-state quantum oscillations in a superconducting heterostructure. *Nature*, 462(7272):487, 2009.

[110] Qing Lin He, Hongchao Liu, Mingquan He, Ying Hoi Lai, Hongtao He, Gan Wang, Kam Tuen Law, Rolf Lortz, Jiannong Wang, and Iam Keong Sou. Two-dimensional superconductivity at the interface of a bi 2 te 3/fete heterostructure. *Nature communications*, 5:4247, 2014.

[111] Albert M Clogston. Upper limit for the critical field in hard superconductors. *Physical Review Letters*, 9(6):266, 1962.

[112] BS Chandrasekhar. A note on the maximum critical field of high-field superconductors. *Applied Physics Letters*, 1(1):7–8, 1962.

[113] Yuta Mizukami, Hiroaki Shishido, Takasada Shibauchi, Masaaki Shimozawa, Satoshi Yasumoto, Daiki Watanabe, Minoru Yamashita, Hiroaki Ikeda, Takahito Terashima, Hiroshi Kontani, et al. Extremely strong-coupling superconductivity in artificial two-dimensional kondo lattices. *Nature physics*, 7(11):849, 2011.

[114] TY Chen, SX Huang, and CL Chien. Pronounced effects of additional resistance in andreev reflection spectroscopy. *Physical Review B*, 81(21):214444, 2010.

[115] TY Chen, Z Tesanovic, and CL Chien. Unified formalism of andreev reflection at a ferromagnet/superconductor interface. *Physical review letters*, 109(14):146602, 2012.

[116] Ph Hofmann. The surfaces of bismuth: Structural and electronic properties. *Progress in surface science*, 81(5):191–245, 2006.

[117] JS Moodera and R Meservey. Superconducting phases of bi and ga induced by deposition on a ni sublayer. *Physical Review B*, 42(1):179, 1990.

[118] Patrick LeClair, JS Moodera, John Philip, and D Heiman. Coexistence of ferromagnetism and superconductivity in n i/b i bilayers. *Physical review letters*, 94(3):037006, 2005.

[119] T Herrmannsdörfer, R Skrotzki, J Wosnitza, D Köhler, R Boldt, and M Ruck. Structure-induced coexistence of ferromagnetic and superconducting states of single-phase bi 3 ni seen via magnetization and resistance measurements. *Physical Review B*, 83(14):140501, 2011.

[120] Silvio Henrique Gonsalves, Yuri Aparecido Opata, Lincoln Brum Leite Gusmão Pinheiro, Adriane Consuelo Da Silva Leal, João Frederico Haas Leandro Monteiro, Ezequiel Costa Siqueira, André Vitor Chaves de Andrade, and Alcione Roberto Jurelo. Superconductivity and magnetism in intermetallic bi3ni1-xfex superconductor. *Solid State Communications*, 242:6–10, 2016.

[121] Michael Ruck and Tilo Soehnel. Transmission-optimized single-crystal structure determination and electronic structure of bi3ni. *ChemInform*, 37(41), 2006.

[122] M Bowen, M Bibes, A Barthélémy, J-P Contour, A Anane, Y Lemaıtre, and A Fert. Nearly total spin polarization in la 2/3 sr 1/3 mno 3 from tunneling experiments. *Applied Physics Letters*, 82(2):233–235, 2003.

[123] RJ Soulen, JM Byers, MS Osofsky, B Nadgorny, T Ambrose, SF Cheng, Pr R Broussard, CT Tanaka, J Nowak, JS Moodera, et al. Measuring the spin polarization of a metal with a superconducting point contact. *science*, 282(5386):85–88, 1998.

[124] B Silva, RF Luccas, NM Nemes, J Hanko, MR Osorio, P Kulkarni, F Mompean, M García-Hernández, MA Ramos, S Vieira, et al. Superconductivity and magnetism on flux-grown single crystals of nibi 3. *Physical Review B*, 88(18):184508, 2013.

[125] Matthias F Groh, Martin Heise, Martin Kaiser, and Michael Ruck. Sanfte festkörperchemie. *Nachrichten aus der Chemie*, 61(1):26–29, 2013.

[126] Ulrich Schwarz, Sophie Tencé, Oleg Janson, Cevriye Koz, Cornelius Krellner, Ulrich Burkhardt, Helge Rosner, Frank Steglich, and Yuri Grin. Cobi3: A binary cobalt–bismuth compound and superconductor. *Angewandte Chemie International Edition*, 52(37):9853–9857, 2013.

[127] Regine Boldt, Anett Grigas, Martin Heise, Thomas Herrmannsdörfer, Anna Isaeva, Stefan Kaskel, Daniel Köhler, Michael Ruck, Richard Skrotzki, and Joachim Wosnitza. Semimetallic paramagnetic nano-bi2ir and superconducting ferromagnetic nano-bi3ni by microwave-assisted synthesis and room temperature pseudomorphosis. *Zeitschrift für anorganische und allgemeine Chemie*, 638(12-13):2035–2043, 2012.

[128] Xiangde Zhu, Hechang Lei, Cedomir Petrovic, Yuheng Zhang, et al. Surface-induced magnetic fluctuations in a single-crystal nibi 3 superconductor. *Physical Review B*, 86(2):024527, 2012.

[129] Jagdish Kumar, Anuj Kumar, Arpita Vajpayee, Bhasker Gahtori, Devina Sharma, PK Ahluwalia, S Auluck, and VPS Awana. Physical property and electronic structure characterization of bulk superconducting bi3ni. *Superconductor Science and Technology*, 24(8):085002, 2011.

[130] Vantari Siva, Paresh C Pradhan, G Santosh Babu, Maheswar Nayak, Pratap K Sahoo, and Kartik Senapati. Superconducting proximity effect in nibi3-ni-nibi3 trilayer system with sharp superconductor-ferromagnet boundaries. *Journal of Applied Physics*, 119(6):063902, 2016.

[131] Thomas Herrmannsdoerfer, Richard Skrotzki, Rico Schoenemann, Joachim Wosnitza, Daniel Koehler, Michael Ruck, and Regine Boldt. Coexistence of ferromagnetism and superconductivity in bi 3 ni nanostructures. *Verhandlungen der Deutschen Physikalischen Gesellschaft*, 2011.

[132] P Neha, P Srivastava, MK Kanojia, SK Jha, and S Patnaik. Synthesis and characterization of bi deficient bi3ni superconductor. In *AIP Conference Proceedings*, volume 1731, page 130050. AIP Publishing, 2016.

[133] A Kadigrobov, RI Shekhter, and M Jonson. Quantum spin fluctuations as a source of long-range proximity effects in diffusive ferromagnet-super conductor structures. *EPL (Europhysics Letters)*, 54(3):394, 2001.

[134] Xinxin Gong, Mehdi Kargarian, Alex Stern, Di Yue, Hexin Zhou, Xiaofeng Jin, Victor M Galitski, Victor M Yakovenko, and Jing Xia. Time-reversal symmetry-breaking superconductivity in epitaxial bismuth/nickel bilayers. *Science advances*, 3(3):e1602579, 2017.

[135] KS Novoselov and AH Castro Neto. Two-dimensional crystals-based heterostructures: materials with tailored properties. *Physica Scripta*, 2012(T146):014006, 2012.

[136] Hennrik Schmidt, Francesco Giustiniano, and Goki Eda. Electronic transport properties of transition metal dichalcogenide field-effect devices: surface and interface effects. *Chemical Society Reviews*, 44(21):7715–7736, 2015.

[137] B Shen, B Zeng, GF Chen, JB He, DM Wang, H Yang, and HH Wen. Intrinsic percolative superconductivity in kxfe2- yse2 single crystals. *EPL (Europhysics Letters)*, 96(3):37010, 2011.

[138] Martin Kaiser, Anna Isaeva, Richard Skrotzki, Ulrich Schwarz, and Michael Ruck. Metastable bi8ni8s by reductive pseudomorphosis of bi8ni8si2. *Zeitschrift für anorganische und allgemeine Chemie*, 637(13):2026–2032, 2011.

[139] N David Mermin and Herbert Wagner. Absence of ferromagnetism or antiferromagnetism in one-or two-dimensional isotropic heisenberg models. *Physical Review Letters*, 17(22):1133, 1966.

[140] Sidney Coleman. There are no goldstone bosons in two dimensions. *Communications in Mathematical Physics*, 31(4):259–264, 1973.

[141] Elihu Abrahams, PW Anderson, DC Licciardello, and TV Ramakrishnan. Scaling theory of localization: Absence of quantum diffusion in two dimensions. *Physical Review Letters*, 42(10):673, 1979.

[142] John Michael Kosterlitz and David James Thouless. Ordering, metastability and phase transitions in two-dimensional systems. *Journal of Physics C: Solid State Physics*, 6(7):1181, 1973.

[143] Takashi Uchihashi. Two-dimensional superconductors with atomic-scale thickness. *Superconductor Science and Technology*, 30(1):013002, 2016.

[144] John M Seddon. Structure of the inverted hexagonal (hii) phase, and non-lamellar phase transitions of lipids. *Biochimica et Biophysica Acta (BBA)-Reviews on Biomembranes*, 1031(1):1–69, 1990.

[145] BI Halperin and David R Nelson. Resistive transition in superconducting films. *Journal of Low Temperature Physics*, 36(5-6):599–616, 1979.

[146] Allen M Goldman and Nina Markovic. Superconductor-insulator transitions in the two-dimensional limit. *Physics Today*, 51:39–44, 1998.

[147] O Pfennigstorf, A Petkova, HL Guenter, and M Henzler. Conduction mechanism in ultrathin metallic films. *Physical Review B*, 65(4):045412, 2002.

[148] Anthony T Bollinger, Guy Dubuis, Joonah Yoon, Davor Pavuna, James Misewich, and Ivan Božović. Superconductor–insulator transition in la 2- x sr x cuo 4 at the pair quantum resistance. *Nature*, 472(7344):458, 2011.

[149] Nicolas Reyren, S Thiel, AD Caviglia, L Fitting Kourkoutis, G Hammerl, C Richter, CW Schneider, T Kopp, A-S Rüetschi, Didier Jaccard, et al. Superconducting interfaces between insulating oxides. *Science*, 317(5842):1196–1199, 2007.

[150] Hidekazu Shimotani, Haruhiko Asanuma, Atsushi Tsukazaki, Akira Ohtomo, Masashi Kawasaki, and Yoshihiro Iwasa. Insulator-to-metal transition in zno by electric double layer gating. *Applied Physics Letters*, 91(8):082106, 2007.

[151] K Ueno, S Nakamura, H Shimotani, A Ohtomo, N Kimura, T Nojima, H Aoki, Y Iwasa, and M Kawasaki. Electric-field-induced superconductivity in an insulator. *Nature materials*, 7(11):855, 2008.

[152] JT Ye, S Inoue, K Kobayashi, Y Kasahara, HT Yuan, H Shimotani, and Y Iwasa. Liquid-gated interface superconductivity on an atomically flat film. *Nature materials*, 9(2):125, 2010.

[153] Miguel M Ugeda, Aaron J Bradley, Yi Zhang, Seita Onishi, Yi Chen, Wei Ruan, Claudia Ojeda-Aristizabal, Hyejin Ryu, Mark T Edmonds, Hsin-Zon Tsai, et al. Characterization of collective ground states in single-layer nbse 2. *Nature Physics*, 12(1):92, 2016.

[154] Xiaoxiang Xi, Zefang Wang, Weiwei Zhao, Ju-Hyun Park, Kam Tuen Law, Helmuth Berger, László Forró, Jie Shan, and Kin Fai Mak. Ising pairing in superconducting nbse 2 atomic layers. *Nature Physics*, 12(2):139, 2016.

[155] QY Wang and Z Li. Q.-y. wang, z. li, w.-h. zhang, z.-c. zhang, j.-s. zhang, w. li, h. ding, y.-b. ou, p. deng, k. chang, j. wen, c.-l. song, k. he, j.-f. jia, s.-h. ji, y.-y. wang, l.-l. wang, x. chen, x.-c. ma, and q.-k. xue, chin. phys. lett. 29, 037402 (2012). *Chin. Phys. Lett.*, 29:037402, 2012.

[156] Jian-Feng Ge, Zhi-Long Liu, Canhua Liu, Chun-Lei Gao, Dong Qian, Qi-Kun Xue, Ying Liu, and Jin-Feng Jia. Superconductivity above 100 k in single-layer fese films on doped srtio 3. *Nature materials*, 14(3):285, 2015.

[157] Yoseph Imry. *Introduction to mesoscopic physics*. Number 2. Oxford University Press on Demand, 2002.

[158] Shingo Katsumoto. Single-electron tunneling and phase transitions in granular films. *Journal of low temperature physics*, 98(5-6):287–349, 1995.

[159] SL Sondhi, SM Girvin, JP Carini, and D Shahar. Continuous quantum phase transitions. *Reviews of modern physics*, 69(1):315, 1997.

[160] DB Haviland, Y Liu, and AM Goldman. Onset of superconductivity in the two-dimensional limit. *Physical Review Letters*, 62(18):2180, 1989.

[161] JJ Paggel, T Miller, and T-C Chiang. Quantum-well states as fabry-perot modes in a thin-film electron interferometer. *Science*, 283(5408):1709–1711, 1999.

[162] Yang Guo, Yan-Feng Zhang, Xin-Yu Bao, Tie-Zhu Han, Zhe Tang, Li-Xin Zhang, Wen-Guang Zhu, EG Wang, Qian Niu, ZQ Qiu, et al. Superconductivity modulated by quantum size effects. *Science*, 306(5703):1915–1917, 2004.

[163] Mustafa M Özer, James R Thompson, and Hanno H Weitering. Robust superconductivity in quantum-confined pb: equilibrium and irreversible superconductive properties. *Physical Review B*, 74(23):235427, 2006.

[164] Mustafa M Özer, Yu Jia, Zhenyu Zhang, James R Thompson, and Hanno H Weitering. Tuning the quantum stability and superconductivity of ultrathin metal alloys. *Science*, 316(5831):1594–1597, 2007.

[165] J Simonin. Surface term in the superconductive ginzburg-landau free energy: Application to thin films. *Physical Review B*, 33(11):7830, 1986.

[166] Mer Tinkham. Effect of fluxoid quantization on transitions of superconducting films. *Physical Review*, 129(6):2413, 1963.

[167] Yu Saito, Yuichi Kasahara, Jianting Ye, Yoshihiro Iwasa, and Tsutomu Nojima. Metallic ground state in an ion-gated two-dimensional superconductor. *Science*, page 1259440, 2015.

[168] Fong-Chi Hsu, Jiu-Yong Luo, Kuo-Wei Yeh, Ta-Kun Chen, Tzu-Wen Huang, Phillip M Wu, Yong-Chi Lee, Yi-Lin Huang, Yan-Yi Chu, Der-Chung Yan, et al. Superconductivity in the pbo-type structure α-fese. *Proceedings of the National Academy of Sciences*, 105(38):14262–14264, 2008.

[169] S Medvedev, TM McQueen, IA Troyan, T Palasyuk, MI Eremets, RJ Cava, S Naghavi, F Casper, V Ksenofontov, G Wortmann, et al. Electronic and magnetic phase diagram of β-fe 1.01 se with superconductivity at 36.7 k under pressure. *Nature materials*, 8(8):630, 2009.

[170] Yoshikazu Mizuguchi and Yoshihiko Takano. Review of fe chalcogenides as the simplest fe-based superconductor. *Journal of the Physical Society of Japan*, 79(10):102001, 2010.

[171] G Wu, YL Xie, H Chen, M Zhong, RH Liu, BC Shi, QJ Li, XF Wang, T Wu, YJ Yan, et al. Superconductivity at 56 k in samarium-doped srfeasf. *Journal of Physics: Condensed Matter*, 21(14):142203, 2009.

[172] Can-Li Song, Yi-Lin Wang, Ye-Ping Jiang, Zhi Li, Lili Wang, Ke He, Xi Chen, Xu-Cun Ma, and Qi-Kun Xue. Molecular-beam epitaxy and robust superconductivity of stoichiometric fese crystalline films on bilayer graphene. *Physical Review B*, 84(2):020503, 2011.

[173] Shiyong Tan, Yan Zhang, Miao Xia, Zirong Ye, Fei Chen, Xin Xie, Rui Peng, Difei Xu, Qin Fan, Haichao Xu, et al. Interface-induced superconductivity and strain-dependent spin density waves in fese/srtio 3 thin films. *Nature materials*, 12(7):634, 2013.

[174] JJ Lee, FT Schmitt, RG Moore, S Johnston, Y-T Cui, W Li, M Yi, ZK Liu, M Hashimoto, Y Zhang, et al. Interfacial mode coupling as the origin of the enhancement of t c in fese films on srtio 3. *Nature*, 515(7526):245, 2014.

[175] Kostya S Novoselov, Andre K Geim, Sergei V Morozov, D Jiang, Y_ Zhang, Sergey V Dubonos, Irina V Grigorieva, and Alexandr A Firsov. Electric field effect in atomically thin carbon films. *science*, 306(5696):666–669, 2004.

[176] Kostya S Novoselov, Andre K Geim, SVb Morozov, Da Jiang, MIc Katsnelson, IVa Grigorieva, SVb Dubonos, Firsov, and AA. Two-dimensional gas of massless dirac fermions in graphene. *nature*, 438(7065):197, 2005.

[177] Yuanbo Zhang, Yan-Wen Tan, Horst L Stormer, and Philip Kim. Experimental observation of the quantum hall effect and berry's phase in graphene. *nature*, 438(7065):201, 2005.

[178] NB Hannay, TH Geballe, BT Matthias, K Andres, P Schmidt, and D MacNair. Superconductivity in graphitic compounds. *Physical Review Letters*, 14(7):225, 1965.

[179] N Emery, C Hérold, M d'Astuto, V Garcia, Ch Bellin, JF Marêché, P Lagrange, and G Loupias. Superconductivity of bulk cac 6. *Physical review letters*, 95(8):087003, 2005.

[180] Thomas E Weller, Mark Ellerby, Siddharth S Saxena, Robert P Smith, and Neal T Skipper. Superconductivity in the intercalated graphite compounds c 6 yb and c 6 ca. *Nature Physics*, 1(1):39, 2005.

[181] Mianqi Xue, Genfu Chen, Huaixin Yang, Yuanhua Zhu, Duming Wang, Junbao He, and Tingbing Cao. Superconductivity in potassium-doped few-layer graphene. *Journal of the American Chemical Society*, 134(15):6536–6539, 2012.

[182] Anand P Tiwari, Soohyeon Shin, Eunhee Hwang, Soon-Gil Jung, Tuson Park, and Hyoyoung Lee. Superconductivity at 7.4 k in few layer graphene by li-intercalation. *Journal of Physics: Condensed Matter*, 29(44):445701, 2017.

[183] S Foner and EJ McNiff Jr. Upper critical fields of layered superconducting nbse2 at low temperature. *Physics Letters A*, 45(6):429–430, 1973.

[184] P De Trey, Suso Gygax, and J-P Jan. Anisotropy of the ginzburg-landau parameter κ in nbse 2. *Journal of Low Temperature Physics*, 11(3-4):421–434, 1973.

[185] HF Hess, RB Robinson, RC Dynes, JM Valles Jr, and JV Waszczak. Scanning-tunneling-microscope observation of the abrikosov flux lattice and the density of states near and inside a fluxoid. *Physical review letters*, 62(2):214, 1989.

[186] CL Huang, J-Y Lin, YT Chang, CP Sun, HY Shen, CC Chou, H Berger, TK Lee, and HD Yang. Experimental evidence for a two-gap structure of superconducting nb se 2: A specific-heat study in external magnetic fields. *Physical Review B*, 76(21):212504, 2007.

[187] T Yokoya, T Kiss, A Chainani, S Shin, M Nohara, and H Takagi. Fermi surface sheet-dependent superconductivity in 2h-nbse2. *Science*, 294(5551):2518–2520, 2001.

[188] DJ Rahn, S Hellmann, M Kalläne, C Sohrt, TK Kim, L Kipp, and K Rossnagel. Gaps and kinks in the electronic structure of the superconductor 2 h-nbse 2 from angle-resolved photoemission at 1 k. *Physical Review B*, 85(22):224532, 2012.

[189] RF Frindt. Superconductivity in ultrathin nb se 2 layers. *Physical Review Letters*, 28(5):299, 1972.

[190] Mohammed S El-Bana, Daniel Wolverson, Saverio Russo, Geetha Balakrishnan, Don Mck Paul, and Simon J Bending. Superconductivity in two-dimensional nbse2 field effect transistors. *Superconductor Science and Technology*, 26(12):125020, 2013.

[191] Y Cao, A Mishchenko, GL Yu, E Khestanova, AP Rooney, E Prestat, AV Kretinin, P Blake, MB Shalom, C Woods, et al. Quality heterostructures from two-dimensional crystals unstable in air by their assembly in inert atmosphere. *Nano letters*, 15(8):4914–4921, 2015.

[192] JM Lu, O Zheliuk, Inge Leermakers, Noah FQ Yuan, Uli Zeitler, Kam Tuen Law, and JT Ye. Evidence for two-dimensional ising superconductivity in gated mos2. *Science*, 350(6266):1353–1357, 2015.

[193] Yu Saito, Yasuharu Nakamura, Mohammad Saeed Bahramy, Yoshimitsu Kohama, Jianting Ye, Yuichi Kasahara, Yuji Nakagawa, Masaru Onga, Masashi Tokunaga, Tsutomu Nojima, et al. Superconductivity protected by spin-valley locking in ion-gated mos2. *Nature Physics*, 12(2):144–149, 2016.

[194] AW Tsen, B Hunt, YD Kim, ZJ Yuan, S Jia, RJ Cava, J Hone, Philip Kim, CR Dean, and AN Pasupathy. Nature of the quantum metal in a two-dimensional crystalline superconductor. *Nature Physics*, 12(3):208–212, 2016.

[195] Denis Dalidovich and Philip Phillips. Phase glass is a bose metal: A new conducting state in two dimensions. *Physical review letters*, 89(2):027001, 2002.

[196] Benjamin T Zhou, Noah FQ Yuan, Hong-Liang Jiang, and Kam Tuen Law. Ising superconductivity and majorana fermions in transition-metal dichalcogenides. *Physical Review B*, 93(18):180501, 2016.

[197] Girish Sharma and Sumanta Tewari. Yu-shiba-rusinov states and topological superconductivity in ising paired superconductors. *Physical Review B*, 94(9):094515, 2016.

[198] Junhua Zhang and Vivek Aji. Topological yu-shiba-rusinov chain in monolayer transition-metal dichalcogenide superconductors. *Physical Review B*, 94(6):060501, 2016.

[199] Wen-Yu He, Benjamin T Zhou, James J He, Noah FQ Yuan, Ting Zhang, and KT Law. Nodal topological superconductivity in monolayer nbse2. *Bulletin of the American Physical Society*, 62, 2017.

[200] N Toyota, H Nakatsuji, K Noto, A Hoshi, N Kobayashi, Y Muto, and Y Onodera. Temperature and angular dependences of upper critical fields for the layer structure superconductor 2h-nbse 2. *Journal of Low Temperature Physics*, 25(3-4):485–499, 1976.

[201] Matteo Calandra, II Mazin, and Francesco Mauri. Effect of dimensionality on the charge-density wave in few-layer 2 h-nbse 2. *Physical Review B*, 80(24):241108, 2009.

[202] Perumal Sekar, Eric C Greyson, Jeremy E Barton, and Teri W Odom. Synthesis of nanoscale nbse2 materials from molecular precursors. *Journal of the American Chemical Society*, 127(7):2054–2055, 2005.

[203] MR Beasley, JE Mooij, and TP Orlando. Possibility of vortex-antivortex pair dissociation in two-dimensional superconductors. *Physical Review Letters*, 42(17):1165, 1979.

BIOGRAPHICAL SKETCH

Gejian Zhao was born on August 29th, 1989 in Sanmenxia, Henan Province, People's Republic of China. He spent his first 18 years in Sanmenxia and Luoyang, Henan Province, and entered School of Science, Beijing University of Posts and Telecommunications in 2008. During his college life, he participated in several research projects and received several awards, including University scholarship, Scholarship of Beijing City, Best innovation award in the 4th Innovation Exhibition of BUPT in 2011. From Auguest 2012, he joined the Department of Physics in Arizona State University, USA. He spent his first two years with Dr. Cun-Zheng Ning and started to work with Dr. Tingyong Chen since 2014. During this period, he participated in several individual and collaborative projects and published 10 papers:

[1]. Li, Hongshi, Xuan Li, Dongrin Kim, Gejian Zhao, Delin Zhang, Zhitao Diao, Tingyong Chen, and Jian-Ping Wang. High spin polarization in epitaxial Fe4N thin films using Cr and Ag as buffer layers. Applied Physics Letters 112, no. 16 (2018): 162407.

[2]. Yi Zhang, Lin Xie, Jeongwoo Kim, Alex Stern, Hui Wang, Kui Zhang, Xingxu Yan, Linze Li, Henry Liu, Gejian Zhao, Hang Chi, Chaitanya Gadre, Qiyin Lin, Yichun Zhou, Ctirad Uher, Tingyong Chen, Yinghao Chu, Jing Xia, Ruqian Wu, Xiaoqing Pan, Discovery of a Magnetic Conductive Interface in ferroelectric/insulator Heterostructures, Nature communications. 2018 Feb 15;9(1):685.

[3]. Chi Tang, Cui-Zu Chang, Gejian Zhao, Yawen Liu, Zilong Jiang, Chao-Xing Liu, Martha R. McCartney, David J. Smith, Tingyong Chen, Jagadeesh S. Moodera, and Jing Shi, Above 400 K Robust Perpendicular Ferromagnetic Phase in a Topological Insulator, Science Advances,6, 115023 (2017).

[4]. J. A. Gifford, B. B. Chen, J. Zhang, G. J. Zhao,D. R. Kim, B. C. Li, D. Wu and T. Y. Chen, Determination of spin polarization using an unconventional iron superconductor, AIP Adv., 6, 115023 (2016).

[5]. J. A. Gifford, G. J. Zhao, B. C. Li, J. Zhang, D. R. Kim, and T. Y. Chen, Zero Bias Anomaly in Andreev Reflection Spectroscopy, J. Appl. Phys., 120, 163901 (2016).

[6]. Y. Jin, P. Khare, S. R. Valloppilly, X.-Z. Li, D. R. Kim, G. J. Zhao, T. Y. Chen, R. Skomski, and D. J. Sellmyer, Magnetism, electron-transport and spin polarization of epitaxial CoFeCrAl films, Appl. Phys. Lett., 109, 142410 (2016).

[7]. Wensen Wei, G. J. Zhao, D. R. Kim, Chiming Jin, Jinglei Zhang, Langsheng Ling, Lei Zhang, Haifeng Du, T. Y. Chen, Jiadong Zang, Mingliang Tian, C. L. Chien, Yuheng Zhang, Rh2Mo3N: A new noncentrosymmetric s-wave superconductor, Phys. Rev. B 94, 104503 (2016).

[8]. J. A. Gifford, G. J. Zhao, B. C. Li, Brian D. Tracy, J. Zhang, D. R. Kim, David J. Smith, and T. Y. Chen, Continuous control of spin polarization using a

magnetic field, Appl. Phys. Lett., 108, 212401 (2016).

[9]. GONG Xin-Xin, ZHOU He-Xin, XU Peng-Chao, YUE Di, ZHU Kai, JIN Xiao-Feng, TIAN He, ZHAO Ge-Jian, CHEN Ting-Yong, Possible p-Wave Superconductivity in Epitaxial Bi/Ni Bilayers, Chin. Phys. Lett. 32, 067402 (2015).

[10]. J. Zhang, J. A. Gifford, G. J. Zhao, D. R. Kim, C. N. Snider, N. Vargas, and T. Y. Chen, Control of thermal gradient using thermoelectric coolers for study of thermal effects, J. Appl. Phys. 117, 17C508 (2015).